MICROSTRUCTURAL STUDY OF INTERGRANULAR $M_{23}C_6$ PRECIPITATES IN ALLOY 709

BY

DONGHEE PARK

DISSERTATION

Submitted in partial fulfillment of the requirements
for the degree of Doctor of Philosophy in Nuclear, Plasma, and Radiological Engineering
in the Graduate College of the
University of Illinois at Urbana-Champaign, 2018

Urbana, Illinois

Doctoral Committee:

Professor James F. Stubbins, Chair
Professor Brent J. Heuser
Professor Pascal Bellon
Associate Professor Yang Zhang

ABSTRACT

The microstructural properties of $M_{23}C_6$ (M: mainly Cr), the predominant precipitate phase of Alloy 709, were studied with respect to the correlation with the austenite matrix, γ-Fe. Alloy 709 specimens, aged at 550, 650, and 750℃ for 1 - 3000 hours, were investigated using electron microscopy and synchrotron X-ray diffraction (XRD). Intergranular $M_{23}C_6$ precipitates were first formed on high angle grain boundaries, followed by the formation of lamella-shaped $M_{23}C_6$ precipitates on twin boundaries. The precipitation time threshold of $M_{23}C_6$ was different from the known behaviors of other Fe-20Cr-25Ni austenitic steels so that the Time-Temperature-Precipitation diagram of the $M_{23}C_6$ precipitate phase in Alloy 709 was newly suggested. The presence of the intergranular $M_{23}C_6$ caused compressive stress on the austenite matrix and tensile stress on the $M_{23}C_6$ precipitates. With increasing aging time, the stress became higher due to the volumetric expansion of the $M_{23}C_6$ precipitates.

The crystallographic characteristics of the intergranular $M_{23}C_6$ were investigated analyzing diffraction patterns of the intergranular $M_{23}C_6$ precipitates and the neighboring austenite. The intergranular $M_{23}C_6$ were formed on the grain boundaries in a cube - cube relationship with the austenite, $[001]_{\gamma\text{-Fe}} \| [001]_{M_{23}C_6}$ and $[110]_{\gamma\text{-Fe}} \| [110]_{M_{23}C_6}$. The intergranular $M_{23}C_6$ on the high angle grain boundaries grew toward the opposite side of the parent austenite grain while maintaining a lattice correspondence, $3 \cdot a_{M_{23}C_6} \approx a_{\gamma\text{-Fe}}$. The lamella-shaped $M_{23}C_6$ precipitates on the twin boundaries also exhibited the analogous growing behavior.

In situ synchrotron XRD tensile tests were performed to reveal the mechanical response of the austenite and the precipitates in Alloy 709. The lattice strain evolution of the austenite was anisotropic for all aging conditions. Grains orientated with $\{2\ 0\ 0\}_{\gamma\text{-Fe}}$ yielded first, inducing compressive microstress on grains orientated with $\{2\ 2\ 0\}_{\gamma\text{-Fe}}$. Grains orientated with $\{1\ 1\ 1\}_{\gamma\text{-Fe}}$ did not yield over the entire strain range. The $M_{23}C_6$ precipitates preferentially hardened $\{2\ 0\ 0\}_{\gamma\text{-Fe}}$ orientated grains that determine the yield of the austenite matrix during lattice strain development. The material was substantially strengthened due to the load partitioning by $M_{23}C_6$, which was proportional to its volume fraction. The further increase of the load partitioning by the precipitates was limited due to the mechanical failure of the precipitates, which was confirmed by microcrack formations near the precipitates.

ACKNOWLEDGMENTS

I would like to express great appreciation to my advisor, Prof. James Stubbins, for his friendly and valuable advice. His support and counsel was crucial to accomplishing my research goal.

I would like to thank Prof. Brent Heuser for his patient advising during my past research works on Zircaloy, which would extend my view for future research.

I would like to thank Prof. Yang Zhang and Prof. Pascal Bellon for their service on my dissertation committee and valuable comments to improve my research.

I would like to thank all the staffs in the Department of Nuclear, Plasma, and Radiological Engineering, the Materials Research Lab in UIUC, and APS in Argonne National Lab for their support and help throughout my research.

I would like to thank my fellow students at UIUC; Xiaochun Han, Kyuhak Oh, Jun-Li Lin, Peter Mouche, Weicheng Zhong, Yinbin Miao, Kuan-Che Lan, Xiang Liu, Huan Yan, Hoon Lee, Dominic Piedmont, Carly Romnes, Yongkyu An, Jinwhan Bae, and Yongseok Lee who gave me unforgettable memories here in Champaign.

Finally, and especially, I would like to thank my wife, Jimin Lee, my daughters, Dain and Deyeon, and my parents, Deokho Park and Jeonja Lee, for their endless love and encouragement during my life-long journey in science.

TABLE OF CONTENTS

CHAPTER 1

INTRODUCTION

1.1 Development of Structural Material for Advanced Nuclear Reactors

Nuclear energy has been a crucial component in the global energy systems and currently faces challenges. According to the International Energy Agency(IEA) report of 2014, nuclear energy constitutes approximately 5% of the world primary energy demand in 2012. The demand of nuclear energy will double from 642 Mtoe (million tonnes of oil equivalent) in 2012 to 1210 Mtoe by 2040, although there were declines in the demand for nuclear energy in the aftermath of the Fukushima Daiichi accident on Mar 11 2011 [1]. The most recent IAEA report said 448 nuclear fission reactors have a generating capacity of 391 (electrical) GWs (status as of December 2016) [2]. It is projected that the global nuclear power capacity for 2030 will increase by 1.9 % in the lowest case scenario and by 56 % in the highest case scenario [2]. In order to respond to the growing demand of electricity generation, advanced nuclear fission reactors, which are called Generation IV reactors (Gen IV), are currently being researched to enhance safety, reliability, and economics. After comprehensive discussions over decades, six nuclear reactor concepts (three thermal reactor concepts and three fast reactor concepts) were selected. The thermal reactor concepts were the very-high-temperature reactor (VHTR), the molten-salt reactor (MSR), the supercritical-water-cooled reactor (SCWR). As for the fast reactor concepts, the gas-cooled fast reactor (GFR), the sodium-cooled fast reactor

(SFR), the lead-cooled fast reactor (LFR) were chosen [3].

A number of candidate structural materials are being evaluated in regard to high temperature performance under irradiation and are summarized in Table 1.1 [4]. Structural materials for advanced nuclear reactors will be used in reactor vessels, primary loop piping, control rods, etc. The materials will be continuously exposed to high temperature, harsh irradiation, and substantial stress for the service time of several tens of years. As shown in Fig. 1.1, the requirements in dose and temperature for in-core structural materials for all Gen IV reactor concepts exceed those of existing nuclear reactors [5]. Challenging issues in the development of structural materials are mechanical behaviors at higher temperatures, resistance to corrosion and creep, and stability against radiation damage without detrimental microstructural degradations.

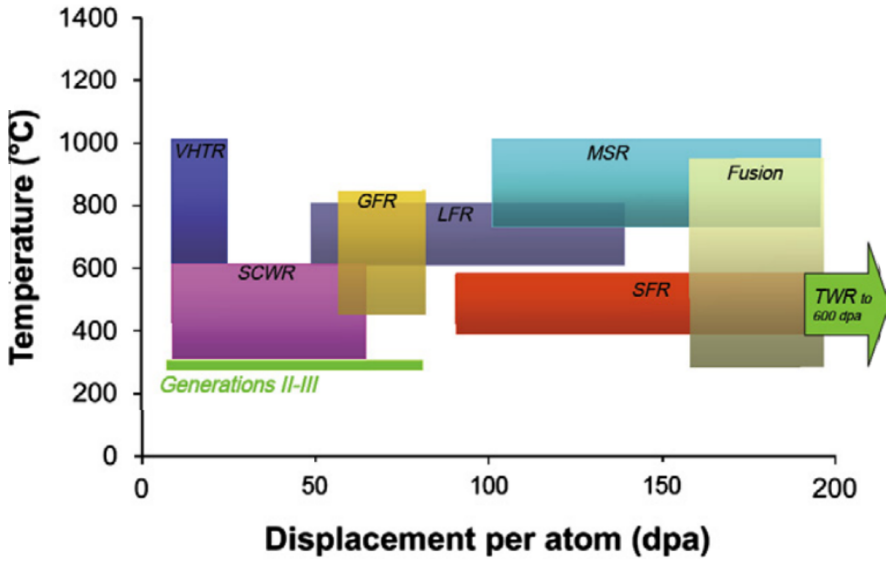

Figure 1.1: The requirements in dose and temperature for in-core structural materials for all proposed Gen IV reactor concepts (adapted from ref. [5]).

Table 1.1: Candidate structural materials for Generation IV advanced reactors (adapted from ref. [4]).

Reactor concept	F-M steel*	Austenitic S.S.	ODS steel†	Ni-base Alloy	Graphite Graphite	Refractory Alloys	Ceramics
VHTR	S	-	-	P	P	S	P
MSR	-	-	-	P	P	S	S
SCWR	P	P	S	S	-	-	-
GFR	P	P	P	P	-	P	P
SFR	P	P	P	-	-	-	-
LFR	P	P	S	-	-	P	P

P: Primary option, S: Secondary option
*F-M: Ferrite-Martensite, †ODS steel: Oxide dispersion-strengthened steel

1.2 Alloy 709

Among the Gen IV concepts, the SFR receives great attention because of the sustainable closed fuel cycle, abundant fuel availability, good economics, and safety [6, 7]. The structural materials in the SFR should withstand high temperatures of up to 600°C under exposure to corrosive sodium coolant so the structural materials must exhibit superior creep/corrosion resistance and mechanical performance. Three candidate materials such as ferrite-martensite steel, austenitic stainless steel, and oxide dispersion-strengthened (ODS) alloys have been investigated for use in the SFR reactors [4, 8–10].

Compared to other candidates for the SFR, austenitic stainless steels exhibit better properties in terms of resistance to creep, corrosion, and heat. Main alloying components of austenitic stainless steels are Cr and Nb. The addition of Cr to austenitic steel improves corrosion/oxidation resistance and hardens the material. Ni is added to stabilize the austenite. Austenitic stainless steels with higher Cr and Nb composition are generally used for applications at the temperature higher than 600°C. In addition, austenitic stainless steels exhibit acceptable formability and weldability. Therefore, austenitic stainless steels are considered as suitable materials for most of Gen IV reactors including the SFR, while there are remaining

issues like relatively larger void swelling under neutron irradiation and higher cost due to a higher Ni composition.

Alloy 709 is derived from NF709 (Fe-20Cr-25Ni-1.5Mo-Nb-B-N austenitic steel), which was developed by Nippon Steel Corporation (Tokyo, Japan) in the 1980s for high-temperature reactors. The alloy composition is a little different from NF 709 (Composition of Alloy 709 can be found in Chapter 3.1). Much higher amounts of Cr and Ni are added to austenitic stainless steels with an Fe-Cr-Ni base system to improve corrosion resistance and stabilize the austenite. NF709 shows superior creep and corrosion resistance at elevated temperatures compared to general austenitic stainless steels [11–13]. The increased operating temperature of advanced nuclear power reactors has led to the development of Alloy 709.

Many studies were performed to characterize the mechanical and corrosive behaviors of Alloy 709 at the elevated temperature up to 750°C [14–21]. Alloy 709 showed better performances in thermal stability, mechanical properties, weldability, creep resistance, and sodium compatibility compared to other advanced austenitic alloys [10]. The steady state creep rate of Alloy 709 was the lowest among high temperature resistant stainless steel such as NF 709, SS316 L(N), the British steel (20Cr-25Ni), and 316H [14, 22]. Creep-fatigue tests showed that grains larger than 400 μm are detrimental to creep-fatigue life [15]. The radiation induced microstructural evolution of Alloy 709 has not been investigated yet, whereas the previous study of NF 709 showed the distributions of Frank loops, voids, radiation induced precipitates, and radiation induced segregation in NF709 was similar to other austenitic steels [23]. Although many advantages of Alloy 709 over other candidates were revealed, most studies were limited with respect to the microstructural aspects.

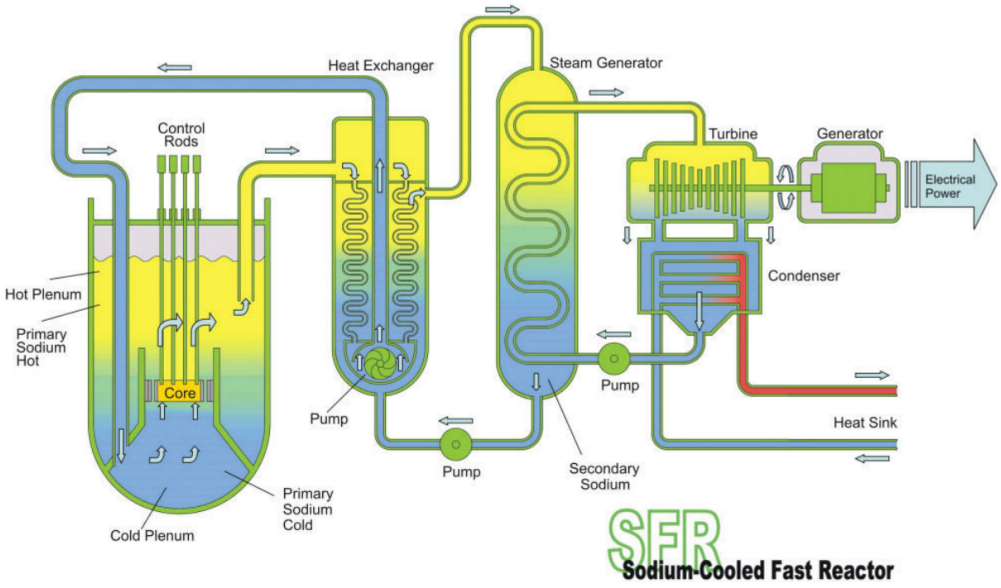

Figure 1.2: Compact loop SFR power plant system (adapted from ref. [7]).

1.3 Research Focus

The material investigated in this study is Alloy 709 (one of the Fe-20Cr-25Ni austenitic alloy class), which is currently recognized as a promising candidate structural material for the SFR. While high-temperature performance of Alloy 709 is being researched, the study of precipitation during aging at elevated temperatures is also of considerable interest because the microstructural changes due to precipitation are associated with the performance of structural materials.

The study of microstructural evolution during age hardening (precipitation hardening) at elevated temperatures is essential because the microstructural changes due to precipitation are critically associated with the properties and performance of Alloy 709. Precipitation is one of the most critical factors influencing the microstructure of metal alloys. In particular, the carbides have a strong tendency to nucleate and grow along grain boundaries(GBs), which affect the mechanical properties of structural components. It is well known that the carbides strengthen the material by inhibiting movement of dislocations or defects. In opposition to this,

the presence of intergranular carbides deforms the GBs and, therefore, provides nucleation sites for microcracks, which initiate the intergranular fracture of the material. However, there is still a lack of research on how the intergranular precipitates correlate with the characteristics of the GBs and affect the mechanical properties of the materials, although many microstructural aspects of the precipitates have been revealed so far.

Consequently, this study focuses on the intergranular precipitation in Alloy 709 and its impact on the microstructural and mechanical properties of Alloy 709. The experiments were designed to investigate the morphological evolution of intergranular precipitates and the surrounding austenite matrix during aging, the correlation between the intergranular precipitates and adjacent austenite matrix, and the role of intergranular precipitation in strengthening of the material. The first objective of this study is to reveal the general features of the precipitates in the aged Alloy 709 in comparison with the as-received Alloy 709. Chapter 3 will analyze the images and the XRD diffraction spectra of the aged Alloy 709 with various aging conditions. The second objective is to investigate the microstructure of the precipitates on the grain boundaries and to study how the microstructure and the distributions of the precipitates correlate with the neighboring austenite in terms of crystallographic characteristics. Chapter 4 will discuss the analysis of the diffraction patterns and the dark field images of the precipitates in Alloy 709 that show the crystal orientation and the morphological distributions. The third objective of this study is to assess the mechanical properties of Alloy 709 that are affected by the presence of the precipitates. Chapter 5 will cover the utilization of the synchrotron XRD diffraction spectra to study the lattice evolution.

CHAPTER 2

LITERATURE REVIEW

Since Alloy 709 has recently drawn interests as a candidate structural material, the microstructural properties of Alloy 709 have not yet been well studied. However, many previous reports showed that various kinds of precipitate phases were formed in the Fe-20Cr-25Ni austenitic alloy class. The dominant precipitate phase after high temperature aging was $M_{23}C_6$ (M: mainly Cr) that was observed mostly on GBs. Since the morphology of $M_{23}C_6$ varies according to the GBs properties, this review first focuses on how to describe the structural relation between the precipitates and the metal grains in terms of characterization of the interphase interface and the GB. Preceding studies that reveal the precipitation behaviors of the Fe-20Cr-25Ni austenitic alloy class are summarized. The growing behaviors of the intergranular $M_{23}C_6$ precipitates were different among GB types and the existing explanations for the behaviors are introduced. The intergranular precipitates either strengthen the material or accelerate the intergranular fracture under stress. The impact of the intergranular precipitates on the mechanical properties of the material is also covered. In addition, a model that predicts an anisotropic response of austenitic steel, a polycrystalline material with an fcc structure, to stress is explained. Finally, brief backgrounds of electron microscopes and X-ray powder diffraction (XRD), analytical tools for the investigation of the morphological evolution of nano- or micro-sized grains, are explained.

2.1 Interphase Interfaces and Grain Boundaries

2.1.1 Interphase Interface between Precipitates and Neighboring Metal Matrix

The interphase interface is a boundary between two distinct phases which may have different crystal structures and/or lattice parameters. The crystal structure of the precipitates may be identical to that of a bulk matrix, but the composition and the lattice parameter are different from the matrix. Thus, an interface between a precipitate grain and a metal grain is called the interphase interface while an interface between polycrystalline metal grains is referred to as the grain boundary. A schematic of the interface types is shown in Fig. 2.1. When the lattice planes of precipitates are continuous with the bulk lattice planes and show no lattice misfit, the precipitates share a fully coherent interface with the surrounding metal matrix as shown in Figs. 2.1(a) and (b). Because the atomic structure is perfect along the interface, only mismatching chemical bonds between the phases contribute to the interfacial energy, which is the lowest among the interphase interface types ($\gamma_{\text{coh}} = \gamma_{\text{chem}} \approx$ 5-200 mJ/m^2) [24]. The small precipitates have almost fully coherent interfaces, which lose coherency with the matrix as the precipitates coarsen. As seen in Figs. 2.1(c) and (d), a long-range uniform elastic strain next to the interface is replaced with a localized strain through the introduction of interface dislocation to reduce the surface energy. A semi-coherent interface has small mismatches in the crystal lattice and can be characterized by the presence of dislocations and lattice strain. A strain (misfit) term is added to the interfacial energy of the semicoherent interface ($\gamma_{\text{semicoh}} = \gamma_{\text{chem}} + \gamma_{\text{str}} \approx$ 200-800 mJ/m^2). When the precipitates and the matrix have no lattice plane continuity as seen in Figs. 2.1(e) and (f), their interface is categorized as an incoherent interface. The structural contribution is dominant in the incoherent interfacial energy and its interfacial energy is much higher than the coherent and semicoherent interface ($\gamma_{\text{incoh}} = \gamma_{\text{chem}} + \gamma_{\text{str}} \approx$ 800-2500 mJ/m^2).

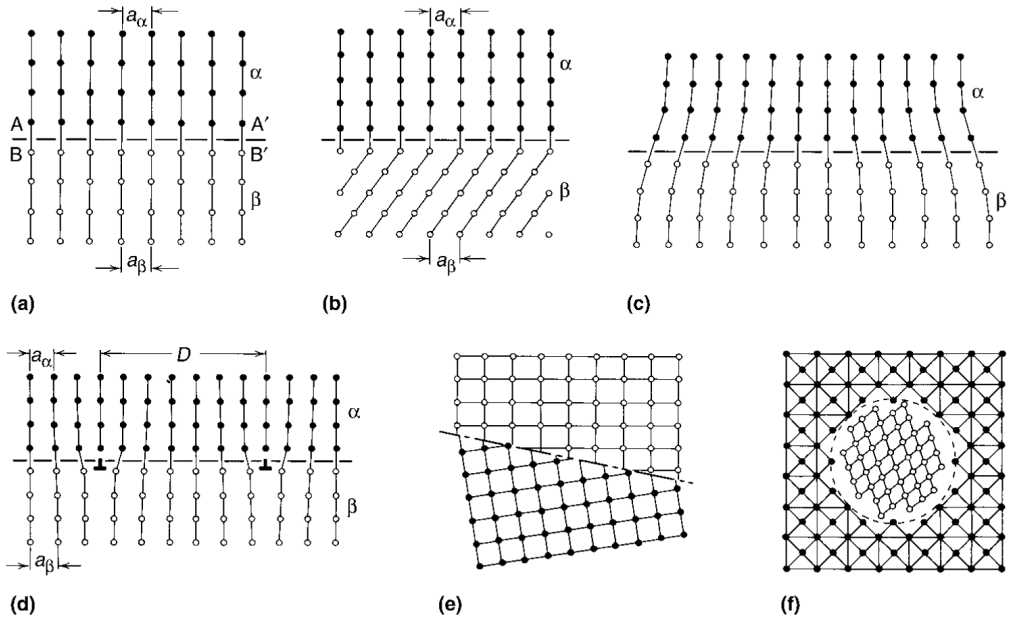

Figure 2.1: Schematic of interface types: (a, b) Fully coherent interface. (c, d) Semicoherent interface with lattice strains and dislocations. (e, f) Incoherent interface (adapted from ref. [25]).

2.1.2 Categorization of Grain Boundaries

The grain boundary is a boundary that separates single-phase two grains with different crystallographic orientations. GBs are categorized according to the misorientation between two adjacent grains as low-angle GBs (LAGBs), coincidence site lattice boundaries (CSLBs), or high-angle GBs (HAGBs). The misorientation matrix, M, is expressed in terms of rotation axis [u, v, w] and rotation angle θ:

$$M = \begin{pmatrix} uu(1-\cos\theta)+\cos\theta & uv(1-\cos\theta)+w\sin\theta & uw(1-\cos\theta)+v\sin\theta \\ uv(1-\cos\theta)+w\sin\theta & vv(1-\cos\theta)+\cos\theta & vw(1-\cos\theta)+u\sin\theta \\ uw(1-\cos\theta)+v\sin\theta & vw(1-\cos\theta)-u\sin\theta & ww(1-\cos\theta)+\cos\theta \end{pmatrix} \tag{2.1}$$

Here, [u, v, w] and θ can be calculated using following equations [26]:

$$[u, v, w] = [M_{32} - M_{23}, M_{13} - M_{31}, M_{21} - M_{12}] \tag{2.2}$$

$$\theta = \arccos\left[\frac{M_{11} + M_{22} + M_{33} - 1}{2}\right] \tag{2.3}$$

LAGBs have a rotation angle between two neighboring grains less than approximately 15° and the other two categories have boundaries with rotation angles larger than 15°. The classification of CSLBs and HAGBs is based on the coincident site lattice (CSL) model [27], which identifies the relation between two adjacent grains using a geometrical construction based on the geometry of the lattice. When the second lattice rotates along the rotation axis, several coincident lattice positions can be measured, as shown in Fig. 2.2, and the number of coincident lattice positions is used to characterize the type of GBs. The CSL boundaries are characterized by Σ, which is the ratio of the number of coincidence sites in a unit cell to the total number of all lattice sites in an unit cell. When Σ is less than or equal to 49, the boundary is defined as a CSLB. Calculated rotation angles and axes of each Σ value can be found in [26]. If the rotation angles and the rotation axis do not match to any of CSLBs, the GB is categorized as a HAGB. An application of the CSL model is acceptable only if proximity to a CSL structure satisfies Brandon's criterion, i.e., $\theta_{\mathrm{m}} < \frac{15}{\Sigma^{1/2}}$, where θ_{m} is the misorientation angle from the exact CSLB structure [28]. For example, twin boundaries occur when one of two identical crystals rotate 60° or 180° along the [1 1 1]; in this case, one lattice position per every three lattice positions are shared between the twin lattices as shown in Fig. 2.2(a). Accordingly, the Σ value of the twin boundaries is 3 and θ_{m} should be less than $\frac{15}{3^{1/2}} = 8.66$ °.

2.1.3 Energy of Grain Boundary

The LAGBs and the low-Σ CSLBs ($\Sigma \leq 29$ in general) are, in general, known to possess a lower boundary energy and mobility than the high-Σ CSLBs ($\Sigma > 29$ in general) and the HAGBs due to their good atomic fit. No model has worked for the interfacial energy per unit area γ for each GB type. Instead, the interfacial energy per unit area, γ, is quantitatively predicted by several models and confirmed

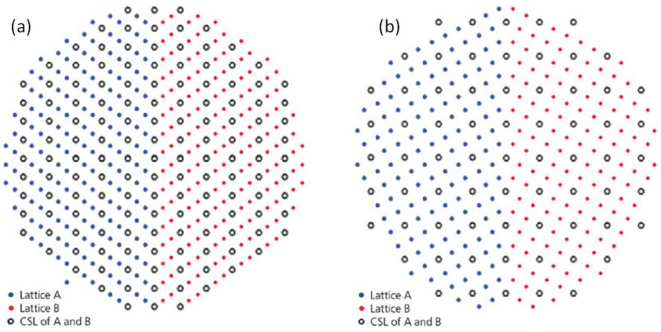

Figure 2.2: Two examples of CSL relationships: (a) The Σ3 boundary (twin boundary) with a rotation angle of 60° and a rotation axis of [1 1 1] and (b) The Σ5 boundary with a rotation angle of 36.9° rotation and a rotation axis of [1 0 0] (adapted from ref. [29]).

by following experimental results. γ is associated with the increase of the Gibbs enthalpy, which is given by

$$\mathrm{d}G = -S\mathrm{d}T + V\mathrm{d}P + \sum_{\mathrm{i}=1}^{\mathrm{C}} \mu_{\mathrm{I}}\mathrm{d}N_{\mathrm{i}} + \gamma\mathrm{d}A \tag{2.4}$$

where S is the entropy of the system, T temperature, V the volume of the bicrystal, P pressure, C the number of constituents, μ_{I} the chemical potential of the constituent i, $\mathrm{N_i}$ the quantity of the constituent i, and A area [30]. Thus, γ is defined by the equation:

$$\gamma = \frac{\partial G}{\partial A_{\mathrm{T,P,N_i}}} \tag{2.5}$$

Read and Shockley assumed that the grain boundary is a row of dislocations and calculated γ as a function of misorientation angle θ by summing the elastic energies of the dislocations:

$$\gamma = \frac{\mu B}{4\pi(1-\mu)} \frac{\theta}{C - ln\theta} \tag{2.6}$$

where μ is the shear modulus, B the slip vector of the dislocation, μ the Poisson coefficient, and C a constant depending on the dislocation [31]. The Read and Shockley formula works well for the LAGBs; γ is proportional to θ in the range 0

to approximately 20° as shown in Fig. 2.3 [32]. Changes in the misorientation angle are strongly correlated with the interfacial energy for the misorientation angle lower than 20° on the [1 0 0] and [1 1 0] rotation axes. In contrast, the interfacial energy is independent in the range of 20° - 70° on the [1 0 0] rotation axis. On the [1 1 0] rotation axis, the interfacial energy abruptly drops near 70° and 129° that are equivalent to the misorientation angle of the {1 1 1} twin plane.

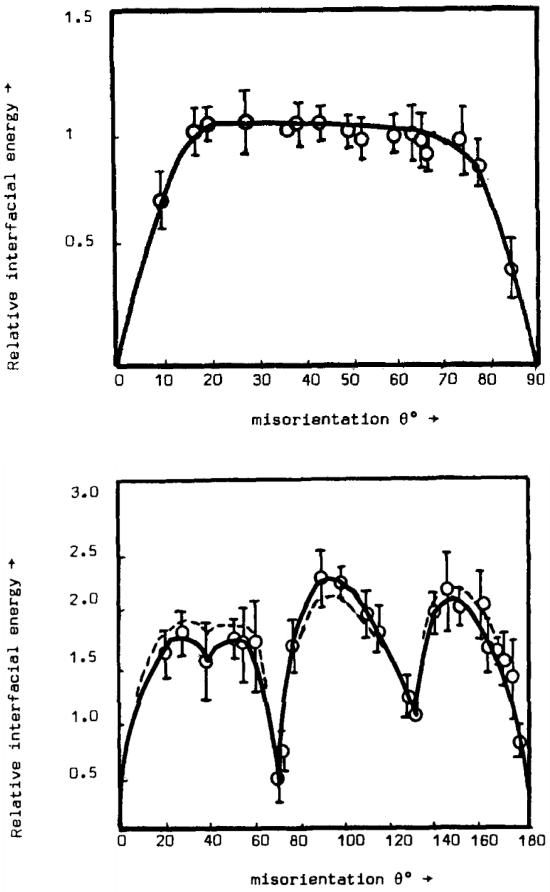

Figure 2.3: Measured relative energies of (top) [1 0 0] and (bottom) [1 1 0] rotation axes in aluminum as a function of θ (adapted from ref. [32]).

2.2 Precipitation in Austenitic Stainless Steel

2.2.1 Precipitation of Fe-20Cr-25Ni Austenitic alloy

A wide variety of precipitate types are formed in austenitic steels during aging and are listed in Table 2.1 (Previous studies are summarized in [33, 34]). Although there is a lack of basic research on Alloy 709, previous studies of NF709 revealed that the major precipitate phases of NF709 are $M_{23}C_6$ (M: mainly Cr), MX (M: Nb or Ti, X: C or N) and Z phase (CrNbN) [12, 23, 35]. An occurrence of the precipitates depends on aging conditions such as aging time and temperature. The precipitates were found mainly near the GBs after 1000 h aging at 700°C, but the precipitate phase was not disclosed in the study [12]. $M_{23}C_6$, Cr_3Ni_2SiX (X: mainly N), and Z-phase were observed at the GBs and the twin boundaries after 100 h aging at 750°C as seen in Fig. 2.4 [35]. The specimens after 3000 h aging at 750°C exhibited G-phase ($Ni_{16}Nb_6Si_7$) that was formed from NbC as a result of silicon segregation [36]. The typical particle size of $M_{23}C_6$ and Cr_3Ni_2SiX precipitates was 0.5-1 μm and Z-phase precipitates showed widths of 50-100 nm [35].

Table 2.1: Structures and compositions of main precipitates in austenitic stainless steel (adapted from ref. [33]).

Precipitate		Structure	lattice parameter [nm]	Composition
Carbide/ Nitride	MX	fcc	a=0.447	NbC
		fcc	a=0.440	NbN
		fcc	a=0.433	TiC
		fcc	a=0.424	TiN
	$M_{23}C_6$	fcc	a=1.057-1.068	M: mainly Cr, Fe,Mo
	Z phase	tetragonal	a=0.3037,c=0.7391	CrNbN
	M_6C	diamond cubic	a=1.062-1.128	$(FeCr)_{21}Mo_3C$, Fe_3Nb_3C, M_5SiC
Intermetallics	σ phase	tetragonal	a=0.880, c=0.454	Fe-Cr-Ni-Mo
	Laves phase	hexagonal	a=0.473, c=0.772	Fe_2Mo or Fe_2Nb
	χ phase	bcc	a=0.8807-0.8878	$Fe_{36}Cr_{12}Mo_{10}$
	G phase	fcc	a=1.12	$Ni_{16}Nb_6Si_7$, $Ni_{16}Ti_6Si_7$

$M_{23}C_6$ has an fcc crystal structure (space group Fm-3m) identical to that of austenite and its lattice parameter is one-third that of austenite ($3 \cdot a_{M_{23}C_6} \approx a_{\gamma\text{-Fe}}$). The $M_{23}C_6$ precipitates in Alloy 709 grow with a cube - cube relationship, $[001]_\gamma \parallel [001]_{M_{23}C_6}$ and $[110]_\gamma \parallel [110]_{M_{23}C_6}$. Therefore, the orientation of the DPs of the $M_{23}C_6$ precipitates is the same as that of the austenitic matrix, and the spacing between diffraction spots are one-third that of austenite as shown in Fig. 2.4 (f). Utilizing these facts, the DPs could be analyzed to reveal the crystallographic correlation between the $M_{23}C_6$ and the austenite.

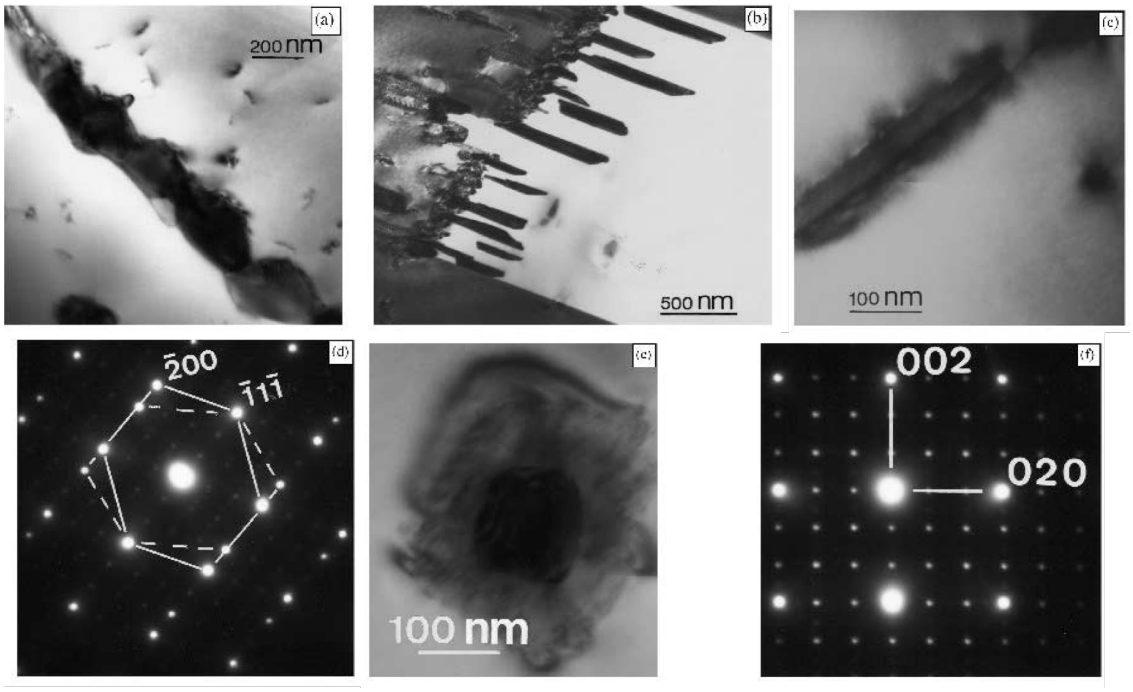

Figure 2.4: Various morphologies of the precipitates in NF 709 after 100 h aging at 750°C: $M_{23}C_6$ on (a) GBs, (b) along incoherent twin boundaries, and (c) on coherent twin boundaries. (d) Diffraction patterns from the precipitate shown in (c). (e) NbN precipitate. (f) Typical diffraction patterns from the $M_{23}C_6$ with the austenite diffraction spots indexed (adapted from ref. [35]).

2.2.2 Growth Mechanism of Intergranular $M_{23}C_6$ Precipitates

During cooling of a metal alloy, the solid state reaction produces and coarsens precipitates in the matrix. The precipitates can be nucleated anywhere (homogeneous nucleation), or the heterogeneous nucleation of precipitates can take place preferentially at specific sites such as dislocations or GBs. The carbide precipitation along the GBs has been studied since the early 20th centuries because it is a critical factor influencing the mechanical degradation such as intergranular corrosion (IGC) and intergranular stress corrosion cracking (IGSCC) [37–40]. The spread of electron microscopes has promoted research into the microstructural behaviors of intergranular precipitates. In particular, the growth mechanisms of the intergranular $M_{23}C_6$ on HAGBs were relatively well studied. The systematic investigation utilizing TEM by Lewis and Hattersley revealed, for the first time, that {1 1 1} of $M_{23}C_6$ is parallel to {1 1 1} of the austenite matrix, independently of $M_{23}C_6$ nucleation sites [41]. It was explained that the reduced strain-energy on the boundaries and dislocations where locally perturbed lattice positions exist is attributed to nucleation and diffusion. The in-situ TEM observation of austenitic stainless steel 304L, under in-situ annealing at 650℃, provided supporting evidence for the preferential migration of intergranular $M_{23}C_6$ towards incoherent matrices [42]. Fig 2.6 showed that fine $M_{23}C_6$ precipitates on GBs grow and aggregate in a film-like layer. The observation of the Cr depletion in the interface with the incoherent matrix, which was confirmed from the EDS line scan, indicated that the Cr diffusion from the incoherent matrix contributed to forming the precipitates. The high interfacial energy of the incoherent interface between the intergranular $M_{23}C_6$ precipitate and the austenite matrix was the driving force for the preferential growth of intergranular $M_{23}C_6$ [42].

Precipitation morphologies are different among the GB types. Lewis and Hattersley observed that the shapes of intergranular $M_{23}C_6$ varied and suggested that

the angle of the GBs could be associated with them. Fine intergranular $M_{23}C_6$ and lamella-shaped precipitates were distributed on the LAGBs and the twin boundaries, respectively. Lim et al. reported that the growth of intergranular $M_{23}C_6$ in LAGBs was retarded in comparison to that on HAGBs as shown in Fig 2.5 [43]. The low grain boundary energy probably results in delaying the growth of intergranular $M_{23}C_6$.

The formation of these lamella-shaped $M_{23}C_6$ precipitates has been observed and discussed in many studies [41, 43–46]. There has been controversy over why the precipitates near the incoherent twin boundaries grow in the shape of lamella, although they agree with the explanation that dislocations provide nucleation sites for the lamella-shaped precipitates. Lewis and Hattersley explained that the nucleation of $M_{23}C_6$ was possible due to Shockley partial dislocations with the Burgers vector $\frac{1}{6}$a<112> near the incoherent twin boundaries, but that there was no specific reason for the spread of lamella-shaped $M_{23}C_6$ outward from the incoherent twin boundaries [41]. According to Sasmal, the localized residual stress on the incoherent twin boundaries due to the anisotropy of austenitic steels probably influenced the nucleation and growth of the lamella-shaped $M_{23}C_6$ precipitates [46].

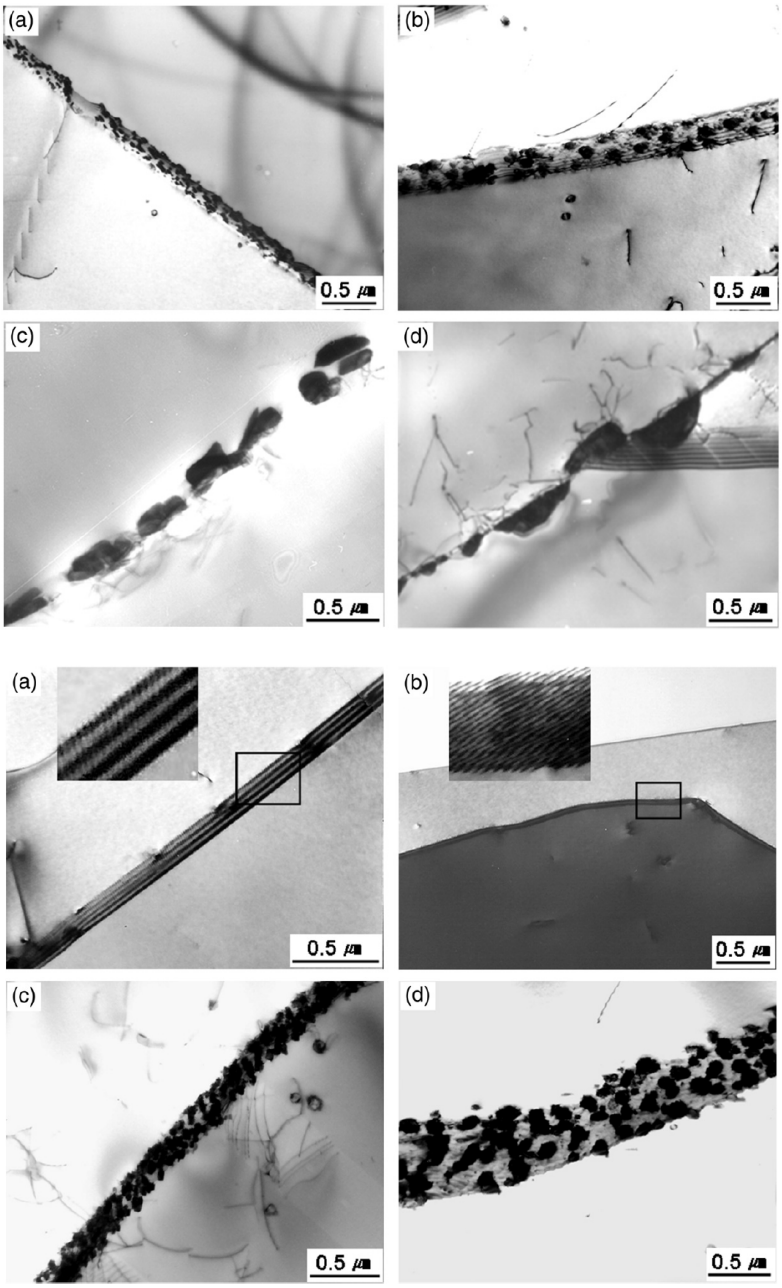

Figure 2.5: Intergranular $M_{23}C_6$ precipitation on (top) HAGBs and (bottom) LAGBs under isothermal treatments at 720℃ for (a) 0.1 h, (b) 1 h, (c) 10 h, and (d) 100 h (adapted from ref. [43]).

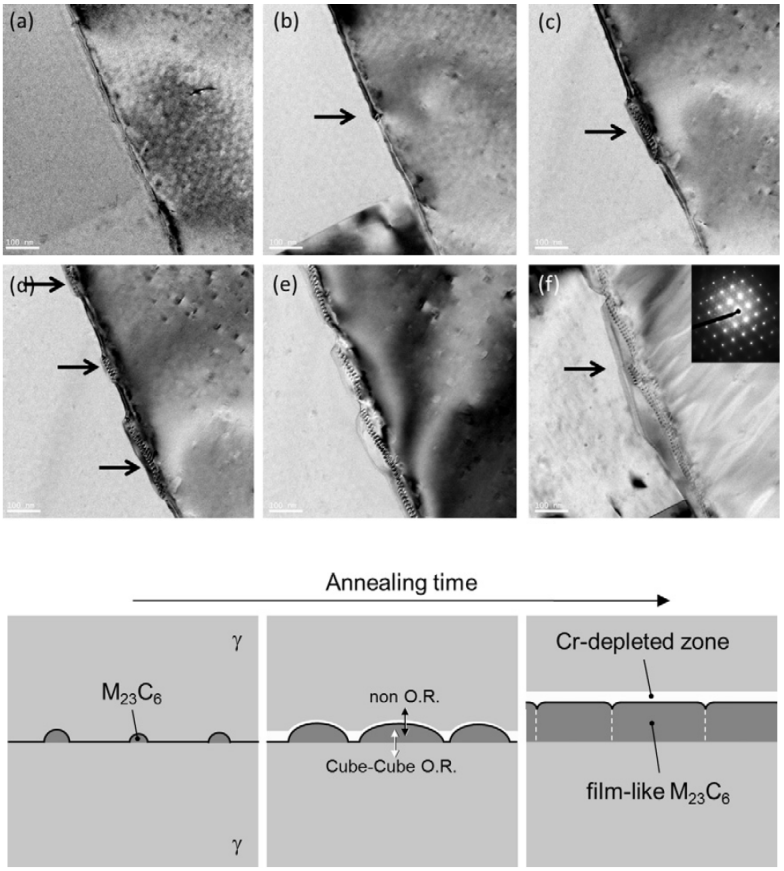

Figure 2.6: (top) In-situ TEM observation of intergranular $M_{23}C_6$ growth: (a) 0, (b) 1, (c) 3, (d) 5, (e) 10 and (f) 60 min. (bottom) Schematic illustrations of the intergranular $M_{23}C_6$ growth (adapted from ref. [42]). The samples were annealed at 650℃.

2.3 Impact of Precipitates on Mechanical Properties of Austenitic Steels

2.3.1 Precipitation Hardening

Precipitation hardening is one of the ways for strengthening the material. The precipitates in metal alloys are nucleated due to a decrease in the solubility limit of the alloying elements when the alloy is cooled. The fine impurity precipitates embedded in metal alloys impede the movement of dislocations or cause defects in the crystal structure. In particular, the precipitates act as obstacles to the dislocation motion so that more stress should be applied on the dislocations penetrating through the precipitates. Since the dislocations are the dominant plasticity carriers, the interaction between precipitates and dislocations leads to an increase of the yield strength of materials. As a dislocation bypasses precipitates in its slip plane via the classical Orowan bowing process, it induces a dislocation loop on it, as shown in Fig. 2.7 (a). The closed loops around the precipitates generate secondary multiple dislocation loops near the precipitates. The precipitate-induced dislocations also attribute to increase residual stress and resistance in the matrix near the precipitates.

2.3.2 Microvoid Formation near Intergranular Precipitates

It is well known that fracture cracks propagate along the GBs. HAGBs show a tendency to lower fracture stress because HAGBs are more susceptible to GB sliding compared to other grain boundary types. It was found that cavities were formed on most HAGBs during deformation, indicating the HAGBs provided preferential sites for microcavities or microcracks [48]. The losses of ductility near the intergranular precipitates weaken the GBs and accelerate the microvoids formation. Considering that the precipitates strengthen the material, the competition between

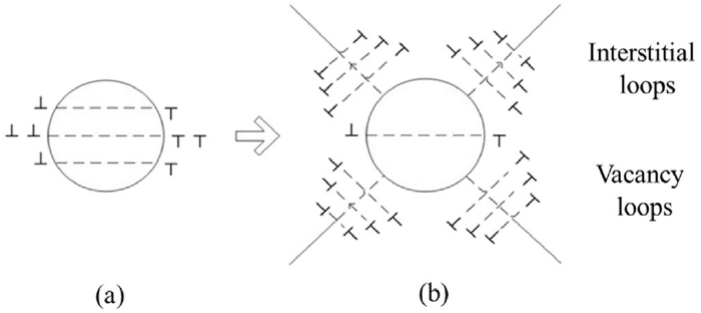

Figure 2.7: Schematic of primary and secondary loops around precipitates (adapted from ref. [47]). (a) Shear-induced primary loops around the precipitate. (b) Secondary slip caused occurred by the nucleation and glide of secondary prismatic loops (interstitial and vacancy).

grain boundary sliding and cavitation probably plays a role during the intergranular cracking; however, a general mechanism to predict the behavior of GBs during deformation has not been yet suggested.

2.3.3 Lattice strain response to stress in austenitic stainless steel

The austenitic stainless steels are an elastically anisotropic polycrystalline material with a face-centered cubic structure. The residual stress in this type of material is classified into three types according to the scale: macrostress (called σ_{I} or Type I stress), intergranular microstress(σ_{II} or Type II stress), and intragranular microstress(σ_{III} or Type III stress) [49]. When the macrostress is applied to the fcc material, individual grains respond differently to the intergranular microstress and, in the elastic regime, the stiffness of the increased lattice strain depends on the inherent anisotropy of the material. The Reuss', Kroner's, and Voigt's model are mostly used to predict the anisotropy of polycrystalline materials [50, 51]. Among these, Reuss developed the model based on the assumption that the same stress is applied over all grains and the strain of each grain is varied by the anisotropy of the material. Reuss's model has worked well in single phase cubic materials. The

elastic modulus and Poisson's ratio for {h k l} is calculated as follows,

$$E_{\mathrm{hkl}} = \frac{1}{S_{11} - 2S_0 A_{\mathrm{hkl}}} \tag{2.7}$$

$$\nu_{\mathrm{hkl}} = \frac{S_{12} + S_0 A_{\mathrm{hkl}}}{S_{11} - 2S_0 A_{\mathrm{hkl}}} \tag{2.8}$$

Here,

$$S_0 = S_{11} - S_{12} - \frac{1}{2S_{44}} \tag{2.9}$$

$$A_{\mathrm{hkl}} = \frac{h^2k^2 + h^2l^2 + l^2k^2}{(h^2 + k^2 + l^2)^2} \tag{2.10}$$

The lattice response to the applied stress in the loading direction for fcc materials is illustrated in Fig. 2.8 (Each lattice plane is perpendicular to the loading direction). The slope of each curve in the elastic regime represents E_{hkl}; $E_{111} > E_{220} > E_{002}$. The stiffness of the increased lattice strain of {1 1 1} orientated grains is the highest and {0 0 2} orientated grains the lowest in the elastic regime. In the plastic regime where the lattice evolution is non-linear, elastically soft {0 0 2} orientated grains exhibit much higher tensile strain after the yield point. From the yield point, the curve for {0 0 2} reflection starts to deviate from the linearity as shown in Fig. 2.8. The lattice evolution of the {0 0 2} orientated grains turn from tensile to compressive and {0 0 2} orientated grains maintain the linearity after the yield point. The precipitates take up load in part in the elastic regime, and the load starts to transfer to the precipitates once the planes of the austenitic matrix yield. Most of the load is partitioned to the precipitate when the material is highly strained.

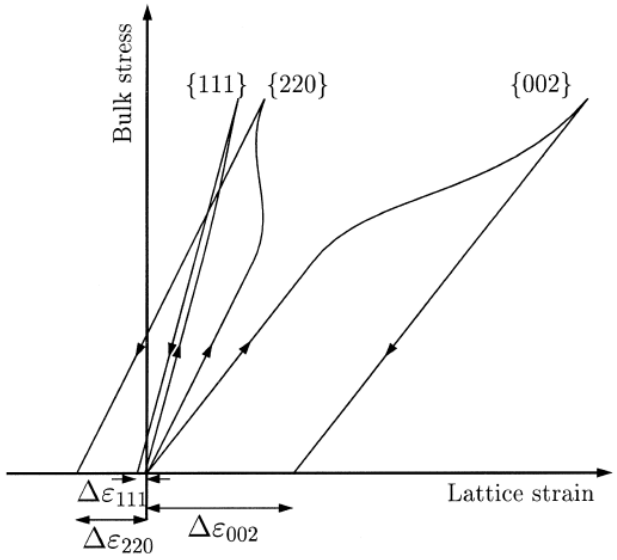

Figure 2.8: Schematic of the lattice strain in a function of applied stress in the loading axial direction for elastically anisotropic fcc materials like nickel and austenitic steels (adapted from ref. [49]). Each curve represents the lattice strain development of grains orientated with {h k l} lattice plane perpendicular to the loading direction.

2.4 Transmission Electron Microscopy

Transmission Electron Microscopes (TEM) are widely used to investigate the crystal structure of the material. When the electrons interact with the crystal planes of the material, they are diffracted according to the crystal structure of the specimen and form specific patterns on the reciprocal space, which are called electron diffraction patterns (DPs). The DPs of each crystal can be obtained by locating the selected area diffraction (SAD) aperture in the TEM. Fig. 2.9 illustrates the basic imaging operation modes in the TEM: bright field (BF) and dark field (DF). An image arising from the direct-beam electrons is called a BF image and its contrast is attributed to the mass density and phase. When an objective aperture allows diffracted electrons along a specific plane as shown in Fig. 2.9 (b) and (c), the contrast only results from the reflection of the planes interacting with electrons (Examples of DF images can be seen in Chapter 4.3). Hence, the diffracted beam with the specifically oriented crystal pole reveals the crystal information of the grains. Since images from electrons impinging off the optic axis suffer from strong aberrations and astigmatism, the diffracted beam should move to the beam axis (the center of the image plate or the screen) for better focus as seen in Fig. 2.9 (c). The other TEM application is dislocation observations. The contrast of dislocations can be enhanced if the specimen is tilted under the "two beam condition" where the Kikuchi line lies on one specific diffracted point. The Kikuchi line arises due to the multiple electron scatterings and shows a stereographic projection of the crystal orientation.

Whereas an almost parallel electron beam is illuminated on an electron-transparent specimen in the TEM, a scanning transmission electron microscope (STEM) scans a focused electron beam over the specimen in a raster pattern. High-angle annular dark-field (HAADF) images can be taken when the detector collects any or all of the diffracted electrons with a high scattering angle. Because incoherently scattered

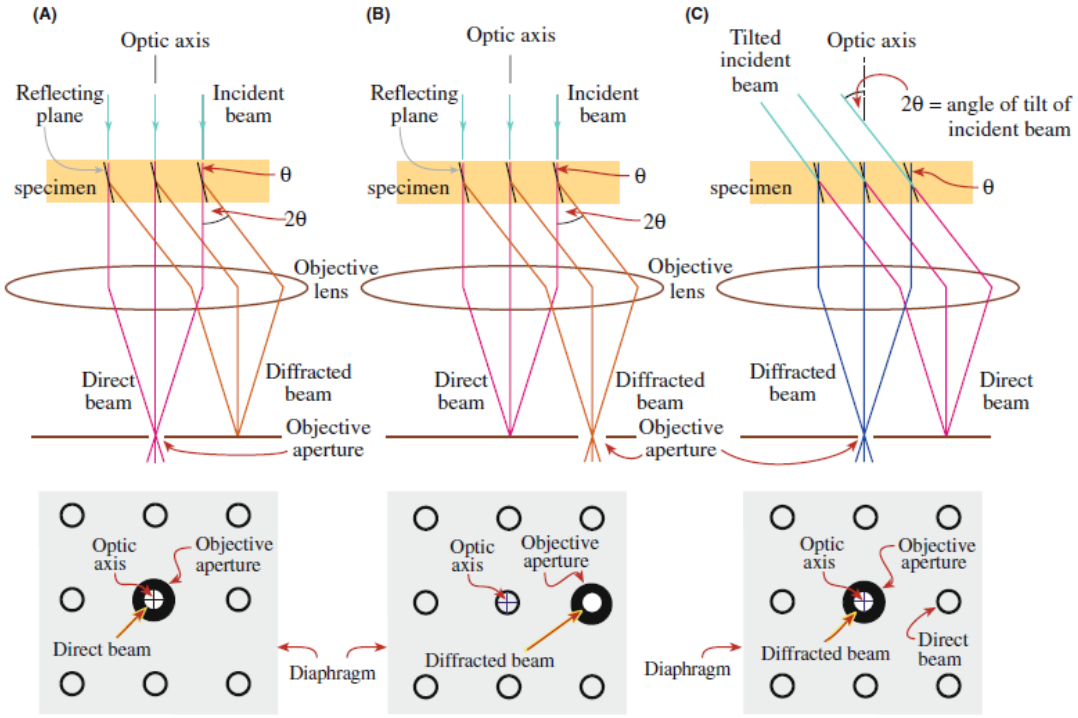

Figure 2.9: Ray diagrams of (A) BF image, (B) displaced-aperture DF, and (C) centered dark-field image (adapted from ref. [52]).

electrons with a large diffracted angle are sensitive to changes in the atomic number (Z) of the interacting atoms, the contrast is directly related to the atomic number. Particles with higher Z exhibit brighter contrast; therefore, these particles can be easily recognized as seen in Fig. 2.10 (c).

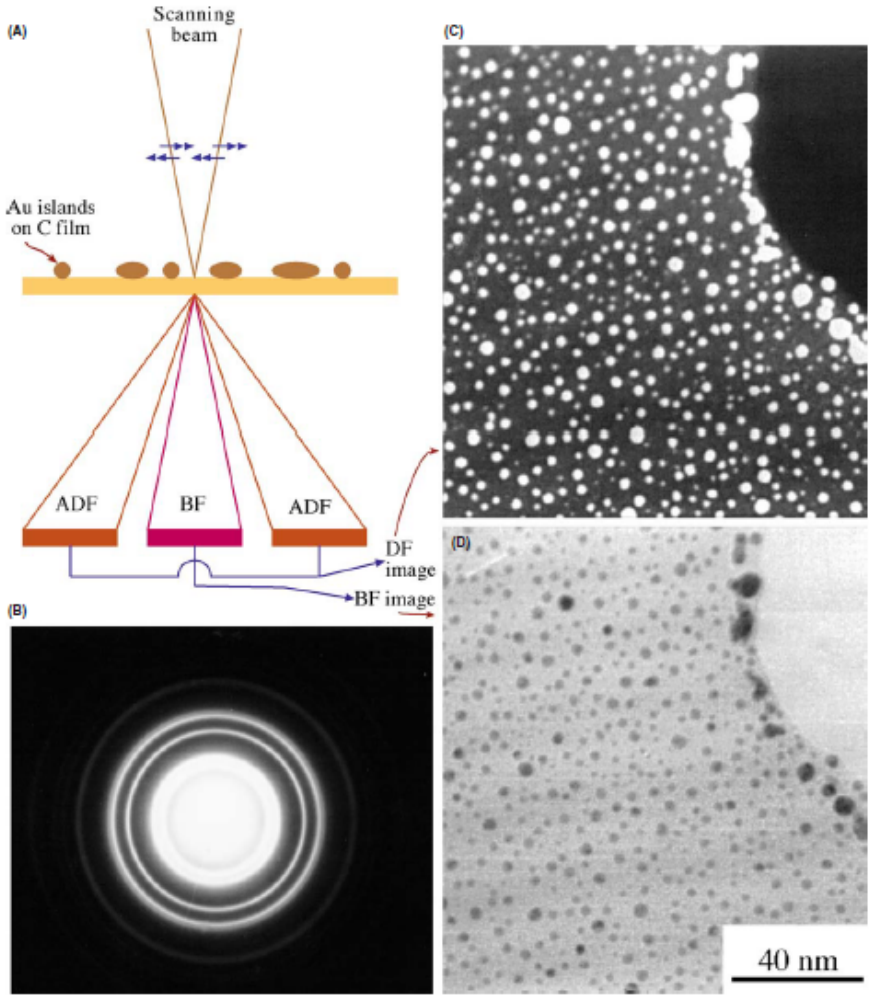

Figure 2.10: (A) Ray diagrams of BF image and annular dark field (ADF) image. (B) Distributed diffracted electrons in the SAD pattern. (C) ADF image and (D) BF image of nano particles (adapted from ref. [52]).

2.5 Synchrotron X-ray Diffraction Analysis

The synchrotron x-ray analysis has several advantages over conventional tabletop XRD measurements. The high-flux synchrotron x-ray returns much higher signals at the detectors and its signal collection time is extremely short. For example, it typically takes less than a second to obtain 2D diffraction profiles from specimens compared to approximately an hour in conventional tabletop XRDs, making in-situ tests during loading possible. In addition, the high energy X-ray can penetrate through the specimen (with a thickness of at most several millimeters); therefore, microstructural information of the whole specimen can be easily obtained without destruction. A higher signal-to-noise ratio and a higher angular resolution are other advantages of synchrotron diffraction techniques.

The X-ray beam is diffracted at a specific angle during penetration when the d-spacing of the material satisfies Bragg's law:

$$2dsin\theta = n\lambda \tag{2.11}$$

where d is the d-spacing value of the diffracting planes, θ the incident angle, n an integer, and λ the X-ray wavelength. The diffracted angles with strong intensity due to constructive interference of the beam are called reflections. The intensity other than the exact reflection angle should be zero under the ideal condition, a perfect crystal structure and a monochromatic beam consisting of perfectly parallel incident X-rays. If an incident angle of the beam path is slightly different from the Bragg angle, the destructive interference is not perfect so the intensity at this angle is not zero anymore. The non-zero intensity of the beam causes the peak broadening and is affected by the grain size, while the FWHM of the peak curve should be zero in the ideal diffraction condition, as shown in Fig. 2.11. The width of the diffraction peak increases as the crystal size decreases and its contribution

can be calculated using Scherrer formula:

$$D = \frac{K\lambda}{\beta(2\theta)cos\theta} \tag{2.12}$$

where β is the spectral integral line breadth (FWHM is typically used in calculation), D the average linear dimension of the particle, K the Scherrer constant, and λ the X-ray wavelength.

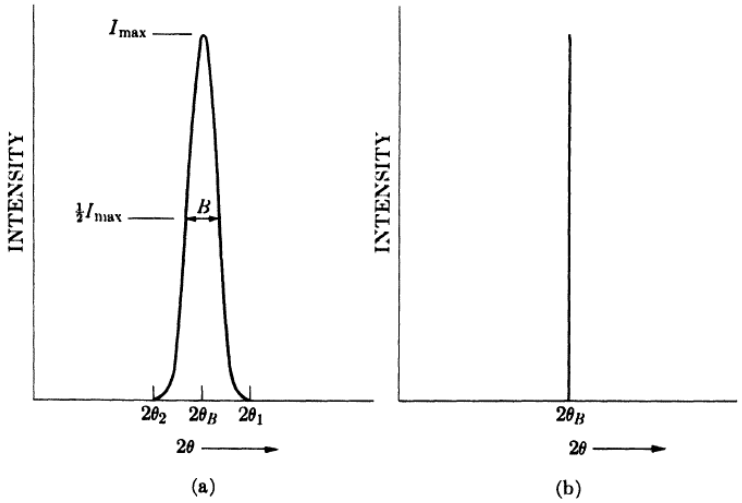

Figure 2.11: Schematic of (a) XRD peak broadening due to particle size (b) XRD peak in the ideal condition (adapted from ref. [53]). FWHM of the peak curve increases as the size of the crystal in actual XRD measurement experiments. The beam intensity should be zero except for the exact Bragg angle when the incident beam is perfectly parallel and monochromatic.

The position of each reflection is correlated with lattice parameters, so the position shifts under deformation or stress and can be used to determine the internal lattice strain of the corresponding planes.

$$\epsilon = \frac{d - d_0}{d_0} \tag{2.13}$$

where d is the d-spacing value of a specific lattice plane under stress and d_0 is the initial spacing without stress. For example, when the material is strained along

the loading direction, d increases more than d_0. Because XRD measures 2θ in a reciprocal space, 2θ in inverse relation to d becomes smaller with increasing stress, as shown in Fig. 2.12(b). In addition, the peak broadening is also attributed to the microstrain and the dislocations inside grains. If the grain is not strained uniformly, the plane spacing of some regions of the grains vary from the initial value, resulting in the formation of sharp scattered peaks near d_0, which is illustrated in Fig. 2.12(c). Williamson and Hall presented that the peak breadth could be calculated as a sum of the crystal size broadening term and the microstrain broadening term [54]:

$$\frac{\beta(2\theta)cos\theta}{\lambda} = \frac{K}{D} + \frac{4\epsilon sin\theta}{\lambda} \tag{2.14}$$

where ϵ is the strain.

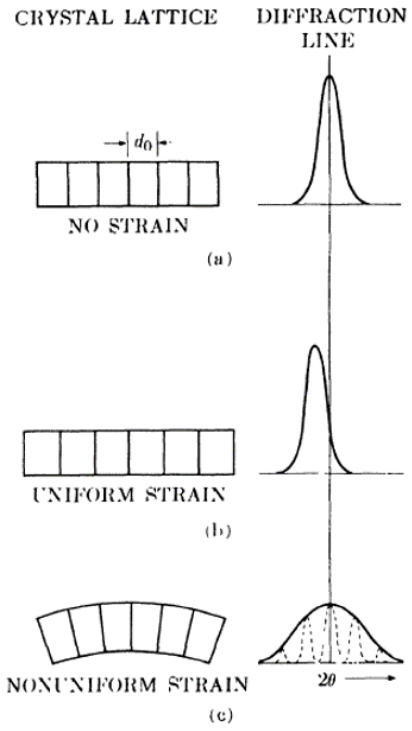

Figure 2.12: Schematic of XRD peak profiles when the grain is under (a) no strain (b) uniform strain (c) nonuniform strain (adapted from ref. [53]).

CHAPTER 3

PRECIPITATION IN ALLOY 709

The first objective of this study is to study the morphological and growth properties of the main precipitate phase in the aged Alloy 709, $M_{23}C_6$. The Alloy 709 specimens were examined using various analytical tools after aging at 550, 650, and 750℃ for 1 to 3000 h. SEM and electron backscatter diffraction (EBSD) were used to observe the morphological features of each aging condition in comparison with those of the as-received Alloy 709. TEM and STEM analysis revealed the crystal structure and the chemical composition of the precipitates and the austenite matrix. The volume fraction and the lattice parameter of the precipitates in the Alloy 709 specimens were calculated from the synchrotron diffraction profiles. $M_{23}C_6$ precipitation on GBs was observed in the Alloy 709 specimens aged at 650 and 750℃. Various shapes and distributions of the $M_{23}C_6$ precipitates were discussed in the context of the correlation between the precipitates and the grain boundary in order to figure out the impact of the precipitation on the morphological changes. Morphological properties of Alloy 709 were similar to other austenitic steel whereas the growth behavior was different. Finally, the Time-Temperature-Precipitation (TTP) diagram of the $M_{23}C_6$ precipitate phase in Alloy 709, which shows the growing behavior of those, could be determined.

3.1 Experimental Methods

3.1.1 Material and Aging Condition

The alloying elements of Alloy 709 are listed in Table 3.1. Forged and hot rolled Alloy 709 was supplied by Oak Ridge National Laboratory (ORNL). The bulk Alloy 709 material was cut into samples with a dimension of $40 \times 6 \times 6$ mm for aging at respective conditions. The specimens were aged at 550, 650, and 750℃ for 1 to 3000 h in air. Table 3.2 provides details of each specimen such as aging time and temperature, as well as the analysis performed. This temperature was chosen due to its relevance to advanced nuclear reactor designs, which may operate at higher temperatures than current commercial plants. All samples were placed in furnaces at room temperature. Then the furnaces were programmed to ramp up to the desired final temperature at a rate of 20°C per minute. The start time for the aging process was initiated only after the temperature of the furnace stabilized (approximately 30-40 minutes after initiating the temperature ramp). Temperature was monitored using thermocouples inserted into the furnaces. The samples were cooled in air (air-quench) after aging.

Table 3.1: Composition in wt% of Alloy 709

Fe	Ni	Cr	Mo	Mn	Si	C
bal.	25.00	19.69	1.46	0.88	0.28	0.063
N	S	P	Ti	Cb	B	
0.14	<0.001	<0.005	<0.01	0.23	0.0022	

3.1.2 Specimen Preparation for Electron Microscopy

SEM and TEM specimens were prepared to investigate the microstructural evolution of the exposed coupons. Cross sections were cut and mounted in the holder of a Buehler polishing machine using a crystal bond. The specimens were polished

Table 3.2: Sample identification matrix showing aging conditions and characterization techniques employed

Sample	Temp. [°C]	Time [hr]	Analysis techniques
A709-AsR*	-	-	SEM, XRD, in-situ XRD, EBSD, EDS, TEM
A709-550C10h	550	10	SEM, XRD
A709-550C100h	550	100	SEM, XRD
A709-550C300h	550	300	SEM, XRD
A709-550C1000h	550	1000	SEM, XRD
A709-550C3000h	550	3000	SEM, XRD
A709-650C10h	650	10	SEM, XRD
A709-650C100h	650	100	SEM, XRD
A709-650C300h	650	300	SEM, XRD
A709-650C1000h	650	1000	SEM, XRD
A709-650C3000h	650	10	SEM, XRD
A709-750C1h	750	1	SEM, XRD
A709-750C5h	750	5	SEM, XRD
A709-750C10h	750	10	SEM, XRD, in-situ XRD
A709-750C100h	750	100	SEM, XRD
A709-750C300h	750	300	SEM, XRD, in-situ XRD, EBSD, EDS, TEM, STEM
A709-750C1000h	750	1000	SEM, XRD
A709-750C3000h	750	3000	SEM, XRD, EBSD, EDS, TEM

*AsR : as-received

with 240, 400, 800, and 1200 grit SiC papers lubricated with water, followed by 9, 3, and 1 μm diamond suspension polishing. Finally, 0.3 μm alumina suspension polishing and 5keV-30μA Ar ion beam milling was used as the final preparation step for SEM and EBSD analysis. This was due to the fact that the electrolyte polishing method, the typical final polishing step for stainless steels, preferentially etched the GBs, resulting in an uneven topology near the GBs. After observation of the morphologies of each specimen, representative samples were selected for further investigation of the microstructure of the GBs and the $M_{23}C_6$ precipitates: A709-AsR, A709-750C300h, A709-750C3000h. The GBs decorated with the precipitates were lifted out and bonded to a copper grid using a focused ion beam (FIB) system. Electron-transparent TEM specimens with a dimension of $10 \times 10 \times 0.1$ μm were examined using TEM and STEM.

3.1.3 Electron Microscopy

The analysis that utilized various kinds of electron microscopes was carried out in the Frederick Seitz Materials Research Laboratory Central Facilities of the University of Illinois at Urbana and Champaign. A JEOL 7000F SEM equipped with an EDS and an EBSD, an FEI Helios 600i dual beam SEM/FIB, and a Scios 2 SEM/FIB equipped with an EBSD were used for plan view. Each operating parameter was carefully optimized to obtain high-quality SEM images. SEMs are typically operated at a high accelerating voltage (15 to 30 kV depending on the instrument) so that the electron probe diameter can be focused smaller to improve the sharpness and the resolution of the images. However, the penetration (approximately 3.1 μm in Fe at the beam energy of 30kV) and the diffusion of high energy electrons become severe, making it difficult to observe the morphologies of the precipitates (with a size of at most several hundred nanometers) or the GBs at the top surface. To offset poor resolution at the lower accelerating voltage mode, the SEM was operated with a short working distance: the accelerating voltage of 5 kV and the working distance of 2-4 mm. The short working distance enhanced the channeling contrast, which arose from the difference in the crystal orientation, due to the backscattered electrons. Since the backscattered electrons always contribute in part to the image contrast in the secondary electron mode, the secondary electron detector could pick up more back scattered electrons in the short working distance, although their intensity is weak. The main disadvantage of the short working distance mode is that the depth of focus is significantly short; however, this could be canceled out by a very flat topology after an ion beam milling. Fig. 3.1 shows differences between the SEM operating conditions. In contrast to Fig. 3.1 (a) taken in the operation mode with the high accelerating voltage and the long working distance, Fig. 3.1(b) explicitly shows twin boundaries (marked with yellow arrows) when the accelerating voltage and the working distance were reduced to

5kV-4mm from 15kV-15mm.

A Hitachi 9500 TEM, a JEOL 2010 LaB6 TEM, and a JEOL 2010F STEM were used to take bright field (BF) images, dark field (DF) images, and diffraction patterns (DPs) of representative regions. The Hitachi 9500 equipped with a LaB6 electron emission gun was operated at an acceleration voltage of 300 kV to achieve 0.18 nm resolution. A wide angle double tilting holder (+/-45 degrees on two axes) of the JEOL 2010 LaB6 TEM was ideal for checking multiple crystal poles, although it had a lower acceleration voltage of 200 kV and a poorer resolution of 0.28 nm. The JEOL 2010F STEM, equipped with an Oxford INCA 30 mm atmosphere thin window (ATW) detector, was performed to obtain HAADF images and EDS spectra for the investigation of the chemical distributions near the GBs. The JEOL 2010F STEM was operated at 200 kV and used a Schottky field emitter source.

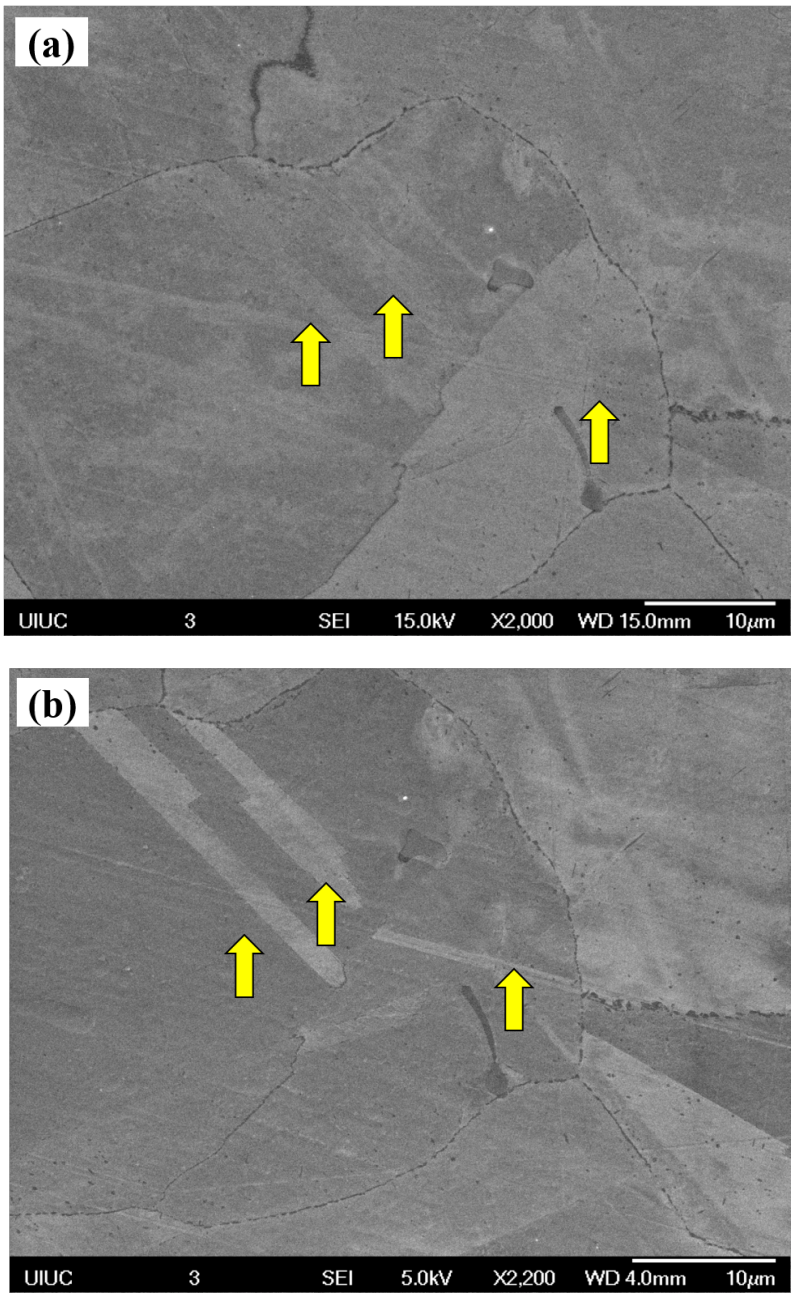

Figure 3.1: Comparison of SEM images with different operating conditions. Both images were taken at the same region of the aged Alloy 709 specimen (at 750℃ for 3000h, A709-750C3000C) with conditions of (a) 15kV accelerating voltage and 15 mm working distance and (b) 5kV accelerating voltage and 4 mm working distance. A twin structure (marked with yellow arrows) was clearly observed at the operation mode with the lower accelerating voltage and the shorter working distance.

3.1.4 Synchrotron Diffraction

The synchrotron XRD analysis was performed in the APS (advanced photon source) synchrotron 1-ID beam line in Argonne national lab. The schematic of the experimental setup is shown in Fig. 3.2. A monochromatic 71.676 keV X-ray beam (equivalent wavelength λ is 0.173 Å) with an incident beam size of 100×100 μm was irradiated on the specimens. The 2D diffraction rings were recorded on a 4-panel set of GE detectors called the Hydra detectors. 200×200 μm detecting pixels were arrayed on the 409.6×409.6 mm detectors (2038 pixels along each horizontal and vertical line). The distance and the tilting angle between the specimen and each GE detector were calculated from calibrating a 2D diffraction ring pattern of a reference specimen, CeO_2, The distance from the specimen to the detectors varies between 2179.6 - 2180.3 mm. After converting the 2D rings to the 1D XRD spectra, the spectra were fitted to a pseudo-Voigt function using GSAS 2 to find the center(θ), intensity, and width of each peak [55].

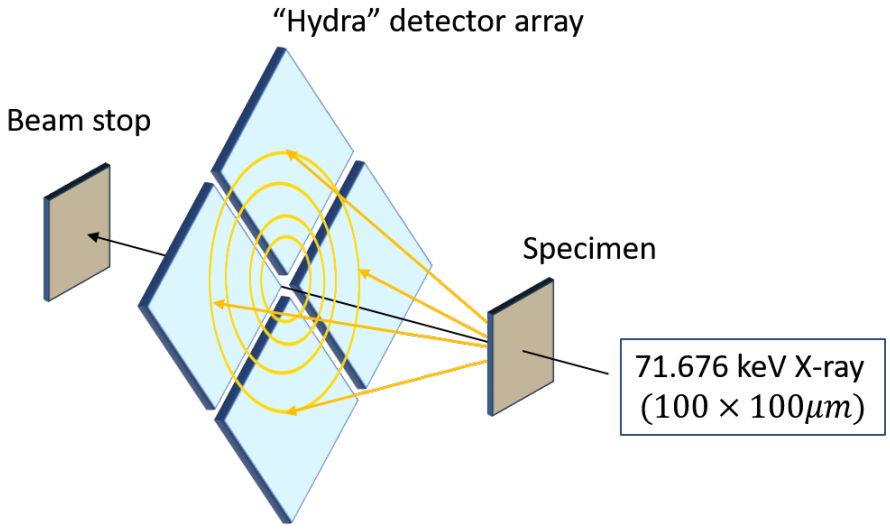

Figure 3.2: Schematic of the synchrotron diffraction experiment

3.2 Microstructure of Aged Alloy 709

3.2.1 Morphological Changes in Aged Alloy 709

The SEM images in Fig. 3.3 show microstructures of (a) the as-received Alloy 709 (A709-AsR) and (b)-(d) the Alloy 709 after aging at 750℃ for 300 h (A709-750C300h). In the as-received sample, the intragranular precipitates were very sparse and no precipitation was observed on GBs. The synchrotron diffraction results (discussed below) confirmed that the phase of the intragranular precipitates is NbN or cementite (Fe_3C) and that $M_{23}C_6$ precipitates were absent in the as-received specimen. In the aged specimen, the frequency of intragranular precipitates increased and the precipitates were present on GBs throughout the aged specimen. EDS analysis (not shown) found that most of the precipitates inside grains or on the GBs have strong Cr peaks, confirming their phase, $M_{23}C_6$. The concentration of carbon in the precipitates could not be determined since the EDS system is not applicable for quantification of lightweight elements. The analysis of DPs and XRD spectra from these precipitates also confirmed the phase of $M_{23}C_6$ (the results and discussion can be found in Chapter 4), confirming that $M_{23}C_6$ is the predominant precipitate phase in aged Alloy 709.

$M_{23}C_6$ showed a strong tendency to nucleate and grew along the GBs in Alloy 709, similar to other austenitic steels. Some intergranular $M_{23}C_6$ precipitates were connected to adjacent precipitates and exhibited semi-continuous growth along the GBs up to a few micrometers in length. Growth of the precipitates towards neighboring grains was also observed. Lamella-shaped $M_{23}C_6$ precipitates were formed near incoherent twin boundaries, with the growing direction parallel to the coherent twin boundary, as seen in Fig. 3.3 (b)-(d). The thicknesses of the lamella-shaped $M_{23}C_6$ precipitates were uniform, approximately tens of nanometers in thickness, and the length varied from approximately 100 nm to, at most, about 1μm. Fig. 3.3

(c) and (d) show intense precipitation near a triple junction. The development of intergranular $M_{23}C_6$ and lamella-shaped $M_{23}C_6$ was much more intense than in the bicrystal GBs. Intergranular precipitates with a thickness between 100 and 250 nm were formed almost continuously near the triple junctions. Lamella-shaped precipitates were also observed at distances as much as several micrometers away from the GB. The length of these precipitates far from the GBs was relatively longer than that of the lamella-shaped $M_{23}C_6$ near the GBs but the thickness was similar.

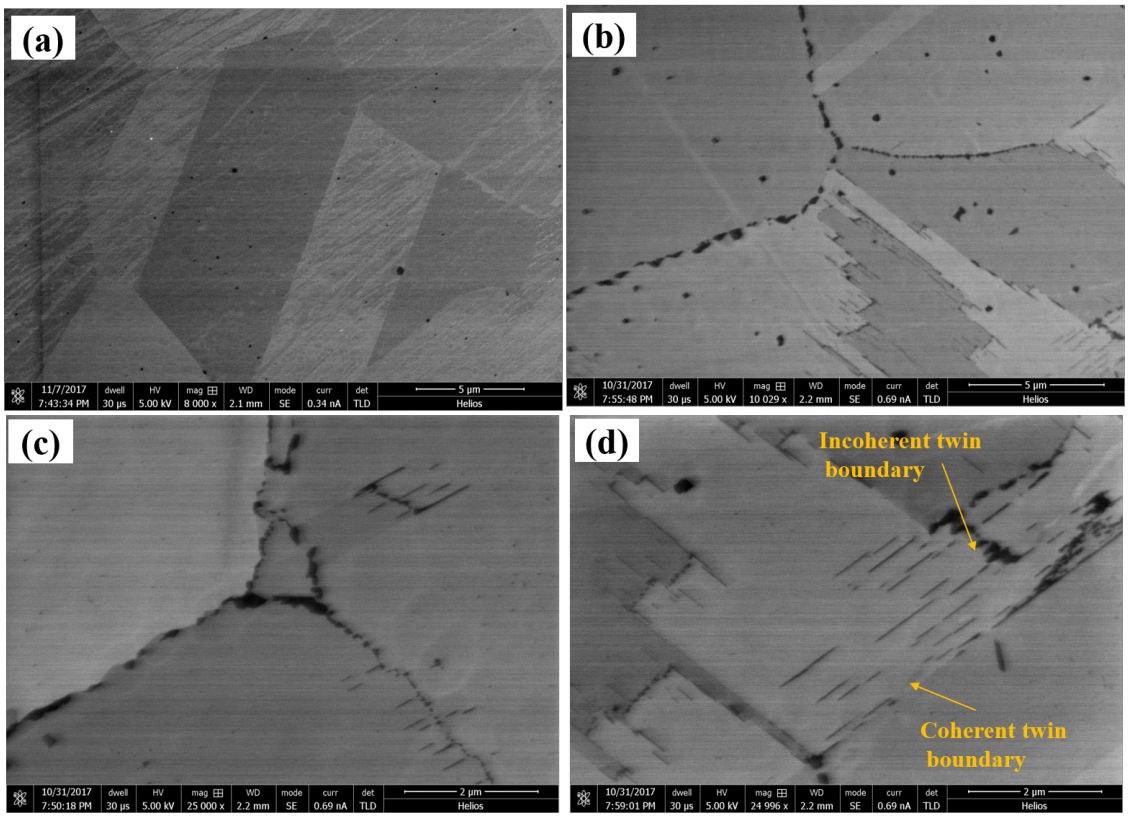

Figure 3.3: SEM images of (a) as-received Alloy 709 (A709-AsR), (b-d) 750℃-300h aged Alloy 709 (A709-750C300h). (c) and (d) exhibited an intense precipitation on a triple junction.

Fig. 3.4 shows EBSD maps representing different orientations of grains and distributions of GBs. Grains in the as-received and the aged Alloy 709 had the average size of 20 - 30 μm. The twin boundaries, LAGBs, and HAGBs account for ap-

proximately 75%, 7%, and 18% of GBs in the aged Alloy 709 (A709-750C300h), respectively. The distribution of GBs in the as-received specimen was analogous to the aged one.

The EBSD results in Fig. 3.5 revealed that the intergranular precipitation of $M_{23}C_6$ correlated with the GB characteristics. The distribution of precipitates varied according to the Σ value of GBs. Relatively large precipitates were formed along the HAGBs (marked with yellow arrows), whereas precipitation was suppressed on the LAGBs. The preferential precipitation of intergranular carbides on the HAGBs was previously observed in other austenitic steels. Trillo and Murr concluded that this precipitation behavior on the HAGBs was due to their high interfacial energy [56].

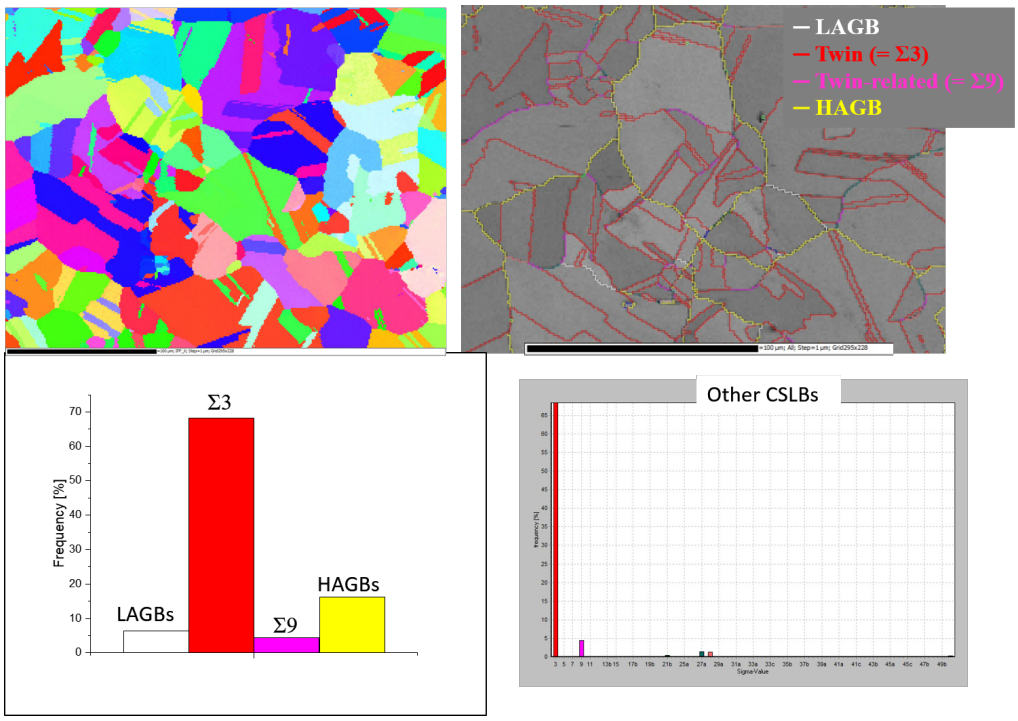

Figure 3.4: EBSD maps of 750℃-300h aged Alloy 709 (A709-750C300h). They represented the distribution of the grains and the GBs. Twin boundaries (Σ3 and Σ9) accounted for most of GBs (approximately 75%); the frequency of HAGB and LAGBS were approximately 7% and 18%.

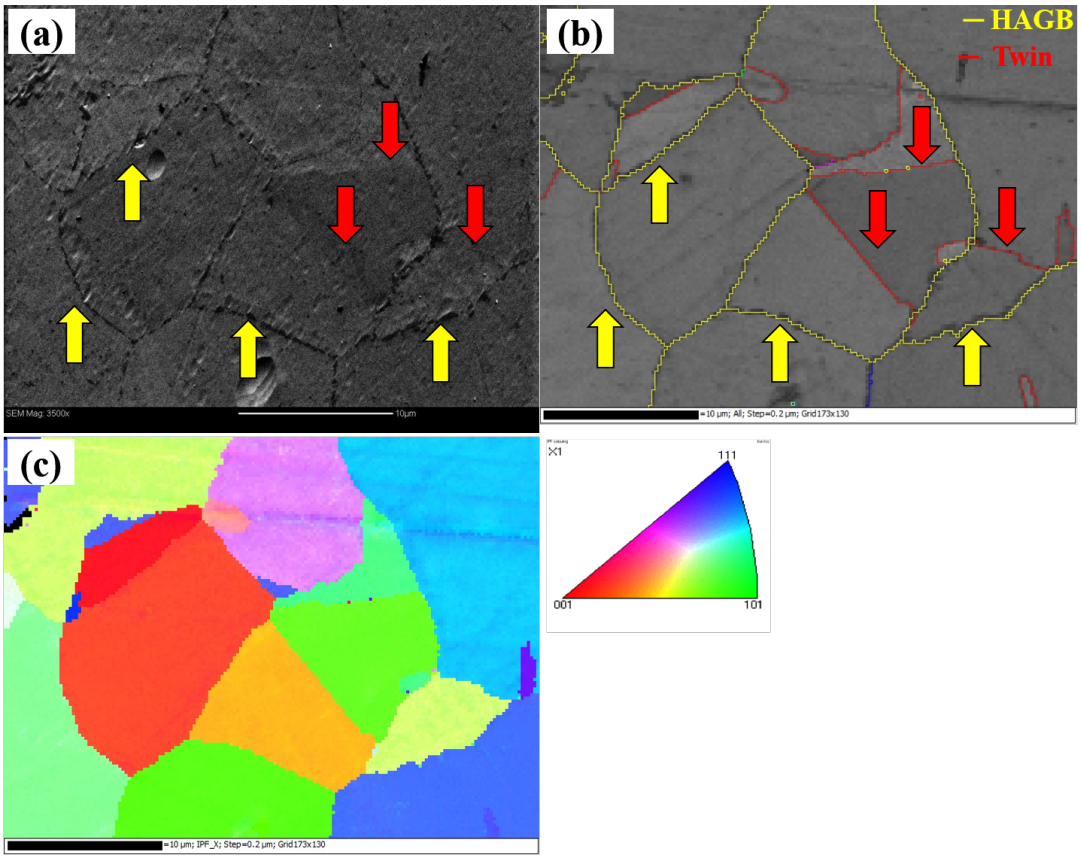

Figure 3.5: (a) SEM image of 750℃-10h aged Alloy 709 (A709-750C10h). (b) GBs with calculated Σ values. (c) Inverse pole figure (IPF) map

3.2.2 Precipitation in Alloy 709

The 1D diffraction profiles of the as-received Alloy 709 (A709-AsR) and the aged Alloy 709 at 750°C for 300h (A709-750C300h) were extracted to identify all precipitate phases, as depicted in Fig. 3.6. It was confirmed that NbN and cementite (Fe_3C) were present both in the as-received Alloy 709 specimen and the aged Alloy 709 specimen. As observed in the SEM results, the only difference between the aged specimen and the as-received one is the formation of $M_{23}C_6$. The formation of G-phase was not detected whereas G-phase was transformed from residual NbN in the other Fe-20Cr-25Ni austenitic alloys [57]. The peak intensity of the residual NbN precipitates did not change much among the XRD spectra of other specimens, suggesting the residual NbN precipitates was stable during aging of Alloy 709. NbC was observed in TEM specimens but was not indexed in the XRD spectra. No Z phase (CrNbN) peak was observed in the spectra for all aging conditions, although the TEM analysis in this study found a precipitate with Cr and Nb composition in the Alloy 709 specimen aged at 750°C for 3000h (A709-750C3000h). However, the exact phase could not be confirmed from the DPs due to its small size (approximately 100 nm). The simulated precipitation behavior in NF 709 and Alloy 709 showed that at 750℃ the Z phase starts to nucleate and grow within 1 h or less but the volume fraction is negligible until it significantly increases after 10000 h [58,59]. The previous TEM works on Alloy 709 specimens aged at 550 - 650 °C for 3000 h exhibited that the Z phase did not precipitate during aging [60]. It was estimated that the Z phase precipitated at 750℃ but their volume fraction was too small to detect. The Cr consumption by the dominant $M_{23}C_6$ phase probably hindered the formation of the Z phase; however, the explanation for the precipitation of the Z phase could not be conclusively drawn here.

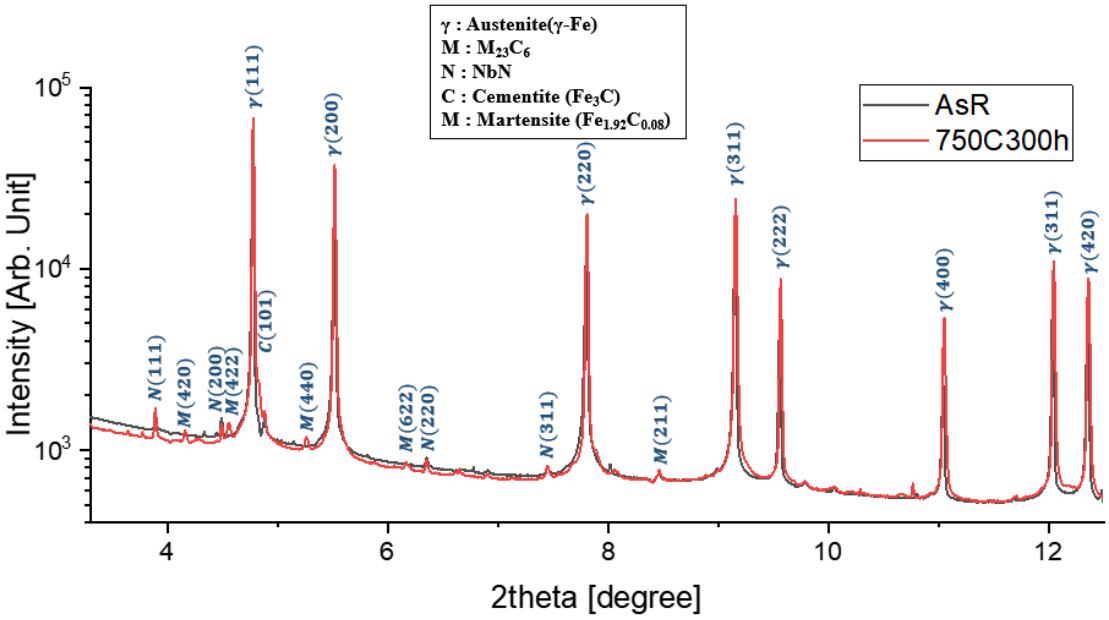

Figure 3.6: XRD spectra of as-received and 750℃-300h aged Alloy 709. All precipitate phases were identified and each reflection was indexed.

3.3 Growing behavior of Intergranular $M_{23}C_6$ in Alloy 709

3.3.1 Morphological Evolution of Intergranular $M_{23}C_6$ in Alloy 709 under Varying Aging Conditions

The SEM images in Fig. 3.7 show microstructures of aged Alloy 709 specimens with various aging conditions: (a) 550℃-3000h (A709-550C3000h), (b) 650℃-10h (A709-650C10h), (c) 650℃-100h (A709-650C100h), (d) 650℃-300h (A709-650C300h), (e) 750℃-1h (A709-750C1h), (f) 750℃-5h (A709-750C5h), (g) 750℃-10h (A709-750C10h), and (h) 750℃-3000h (A709-750C3000h). The morphologies of all specimens at 550℃ were analogous to the as-received specimen; no precipitate was observed on GBs. For 650°C aging conditions, all samples were different from the as-received one, except for the 650°C-10h specimen (Fig. 3.7(b)) without intergranular precipitates. Fig. 3.7(c) showed that at 650℃-100h condition the $M_{23}C_6$ precipitated on some GBs, while lamella-shaped $M_{23}C_6$ were not found throughout the specimen. In the 650°C-300h specimen, both intergranular $M_{23}C_6$ and lamella-shaped $M_{23}C_6$ were observed. The frequency of the intergranular $M_{23}C_6$ was low in the 650°C-100h specimen and became higher when the aging time increased. These results confirmed that at 650℃ the intergranular $M_{23}C_6$ precipitates first precipitate out on HAGBs and their precipitation (time) threshold is approximately 10 to 100 h, and that the formation of the lamella-shaped $M_{23}C_6$ needs an aging of 100 to 300h. For 750℃ aging conditions, while the 1 h aged specimen (Fig. 3.7 (e)) showed a small precipitation on the HAGBs, intense precipitation was observed in other specimens with longer aging time as shown in Fig. 3.7 (f)-(h). The frequency of the intergranular $M_{23}C_6$ and the lamella-shaped $M_{23}C_6$ became higher with increasing aging time. The precipitation of intergranular $M_{23}C_6$ and lamella-shaped $M_{23}C_6$ started within 5 hours under aging at 750°C, showing consistency with the simulated precipitation behavior of $M_{23}C_6$ in NF 709 [59].

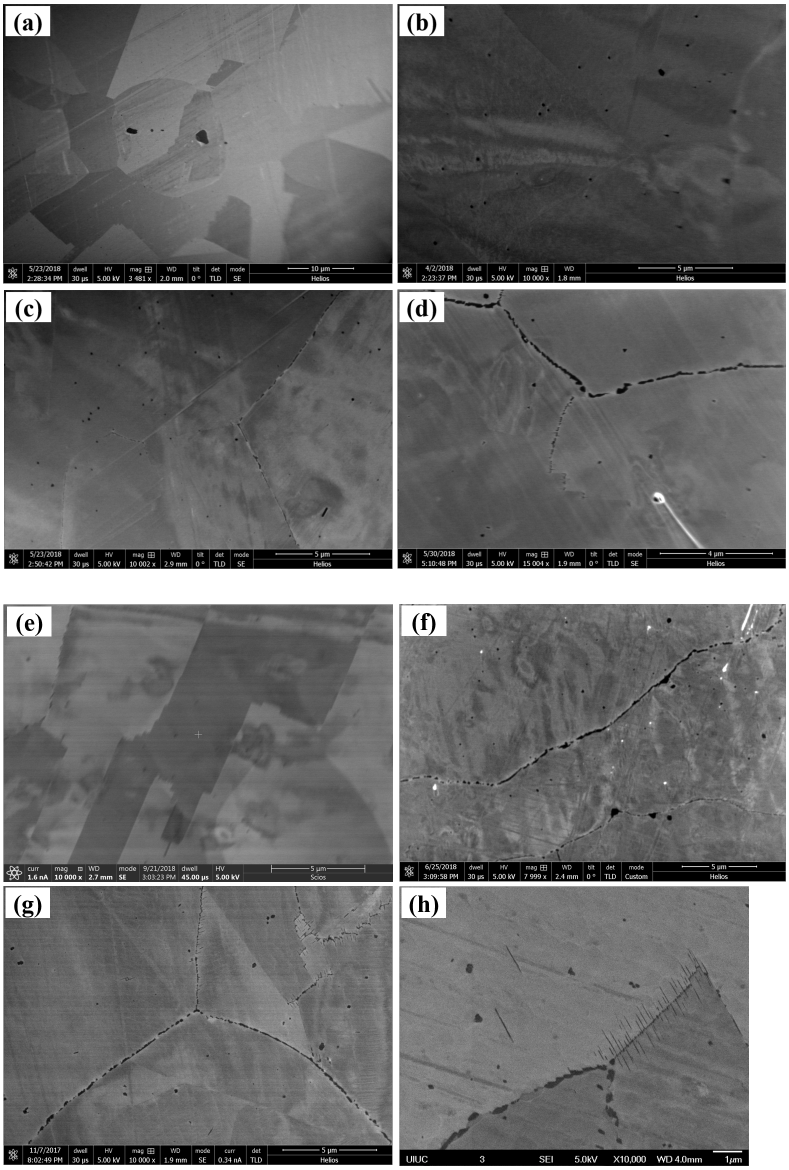

Figure 3.7: SEM images of aged Alloy 709 with various aging conditions: (a) 550℃-3000h, (b) 650℃-10h, (c) 650℃-100h, (d) 650℃-300h, (e) 750℃-1h, (f) 750℃-5h, (g) 750℃-10h, and (h) 750℃-3000h.

3.3.2 XRD analysis of Intergranular $M_{23}C_6$ in Alloy 709 under Varying Aging Conditions

Fig. 3.8, 3.9, and 3.10 show 1-D XRD spectra of specimens aged at 550, 650, and 750℃. Like SEM results above, no $M_{23}C_6$ peak was observed at the expected positions of $(420)_{M_{23}C_6}$ and $(460)_{M_{23}C_6}$ for 550℃ aging conditions, as depicted in Fig. 3.8. The XRD spectra of the 650°C-10h specimen in Fig. 3.9 exhibited very weak peaks near the $(420)_{M_{23}C_6}$ and $(440)_{M_{23}C_6}$ position but they were indexed as oxides. The SEM results for this aging condition, showing no intergranular $M_{23}C_6$, also supported the absence of $M_{23}C_6$ in the austenite matrix. The strong peaks in other spectra confirmed that the precipitation threshold was 100 h for 650°C aging. Fig. 3.10 showed that the $M_{23}C_6$ precipitates were present in all the specimens aged at 750°C. Taking into account the SEM and XRD results, the precipitation threshold of the $M_{23}C_6$ precipitates at 750° probably is likely to be approximately 1 h, showing consistency with the simulated results of NF 709 [59].

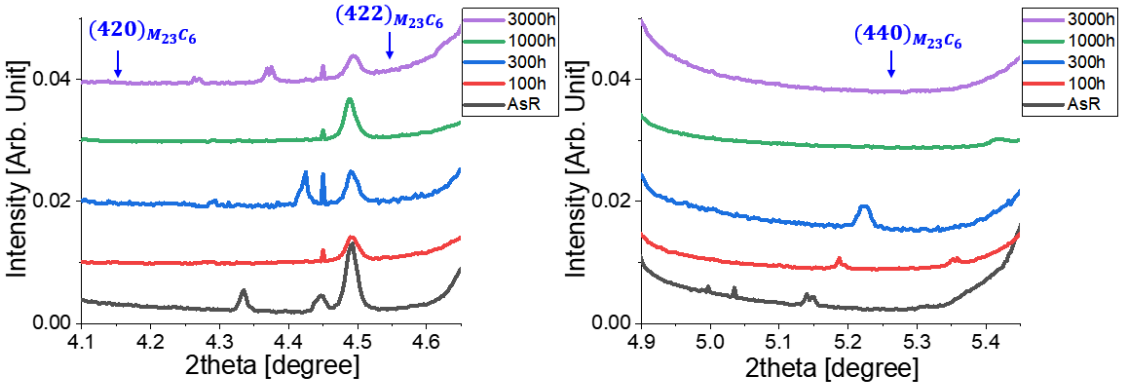

Figure 3.8: XRD spectra of Alloy 709 aged at 550℃. No peak was observed at the expected positions of $M_{23}C_6$.

The intensity of the $(422)_{M_{23}C_6}$, $(420)_{M_{23}C_6}$, and $(442)_{M_{23}C_6}$ peaks grew with increasing aging time, indicating that the volume fraction of $M_{23}C_6$ became higher. The volume fraction of $M_{23}C_6$ was calculated using the GSAS 2 software. Fig. 3.11

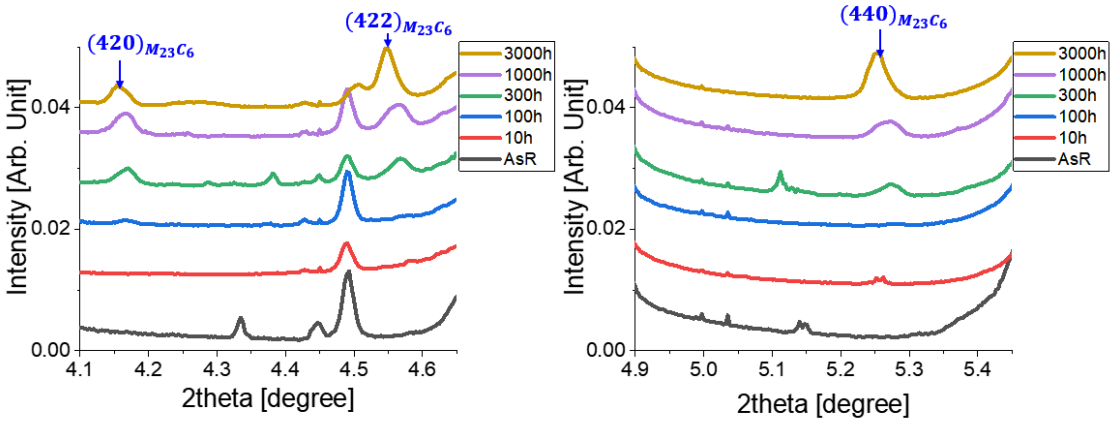

Figure 3.9: XRD spectra of Alloy 709 aged at 650℃. $(420)_{M_{23}C_6}$, $(422)_{M_{23}C_6}$, and $(440)_{M_{23}C_6}$ were found except for 10 h aging. Peak shifts to left and increases of the intensity were observed with increasing aging time.

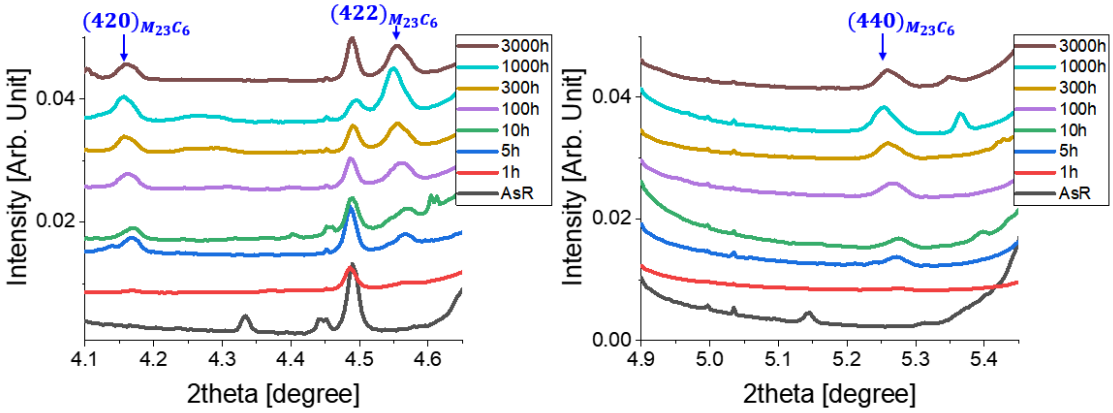

Figure 3.10: XRD spectra of Alloy 709 aged at 750℃. $(420)_{M_{23}C_6}$, $(422)_{M_{23}C_6}$, and $(440)_{M_{23}C_6}$ were indexed in all aging conditions. Peak shifts to left and increases of the intensity were observed with increasing aging time.

shows the increase in $M_{23}C_6$ volume fraction in relation to the aging time. The reason for the abrupt decrease of the $M_{23}C_6$ volume fraction in the 750℃-3000h specimen was not clear. The fraction slowly increased until 3000 and 1000 hours for 650 and 750℃ aging conditions, respectively. The simulation by Shim et al. predicted that for 750℃ aging the volume faction significantly increases after 1 h and reaches a plateau, approximately 3.2 %, after 2 hours [59]. The maximum of the volume fraction of $M_{23}C_6$ in this study was 0.253 %; its carbon content was calculated as 0.013 wt%. Considering the nominal carbon content in Alloy 709 of 0.067 wt%, the $M_{23}C_6$ volume fraction was not likely to reach to saturation. The much lower carbon composition of Alloy 709 (0.063 wt% in Alloy 709 and 0.15 wt% in NF 709) was estimated to cause the slower growth of $M_{23}C_6$. It may need more samples with longer aging conditions for better statistics.

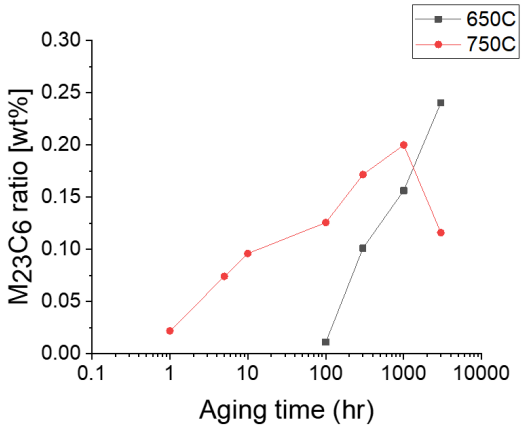

Figure 3.11: $M_{23}C_6$ volume fraction curves of as a function of aging time for Alloy 709 aged at 650 and 750°C.

The width of the $M_{23}C_6$ peaks varied little among different aging conditions, suggesting there was no correlation to the aging time. The simulated behavior also showed that the size of $M_{23}C_6$ saturated right after the precipitation time threshold of $M_{23}C_6$ [59].

In Fig. 3.9 and 3.10, it could be noticed that each $M_{23}C_6$ peak shifted left

with longer aging time, indicating the lattice planes of $M_{23}C_6$ were under stress. Because the recorded diffraction rings were in a reciprocal space, the diameter of diffraction rings was inversely related to the d-spacing value. The 2θ value of $M_{23}C_6$ became smaller while the d-spacing grew and vice versa. Fig. 3.12 shows that at 650℃ the d-spacing of the $M_{23}C_6$ remained steady until 300 h, and increased with aging. At 750℃ , it increased gradually from 10 h to 1000h. The d-spacing of the austenite matrix followed a trend of gradually decreasing with increasing aging time. Assuming that the as-received sample is free of stress, Eq.2.13 gives the lattice strains of the austenite matrix are -1.2×10^{-3} and -1.4×10^{-3} for the 650°C-3000h specimen and the 750°C-3000h specimen. In case of $M_{23}C_6$, the minimum d-spacing value of 750℃ was used for the strain calculation. General Hooke's law can be used to calculate the residual stress from the measured lattice strain:

$$\sigma_{\mathrm{ii}} = \frac{E^{hkl}}{1+\nu^{hkl}}(\epsilon_{\mathrm{ii}}{}^{hkl} + \frac{\nu^{hkl}}{1-2\nu^{hkl}}(\epsilon_{11}{}^{hkl} + \epsilon_{22}{}^{hkl} + \epsilon_{33}{}^{hkl})) \tag{3.1}$$

Here {h k l} specific Young's modulus and Poison's ratio were obtained from the in-situ experiments (discussed in Chapter 5) and ϵ_{33} was assumed to be same as ϵ_{22}. Fig. 3.13 shows the absolute value of the stress on the austenite matrix and the $M_{23}C_6$ precipitates became larger as the aging time increased. Considering the direct relationship between the volume fraction of the $M_{23}C_6$ and the aging time, the increase of the residual stress on the austenite matrix and the $M_{23}C_6$ precipitates was thought to result from the volumetric expansion of the $M_{23}C_6$ precipitates on the GBs. Therefore, it could conclude that the austenite matrix is subjected to a compressive stress because of the presence of intergranular $M_{23}C_6$, and that the stress grows as more precipitates are formed on the GBs.

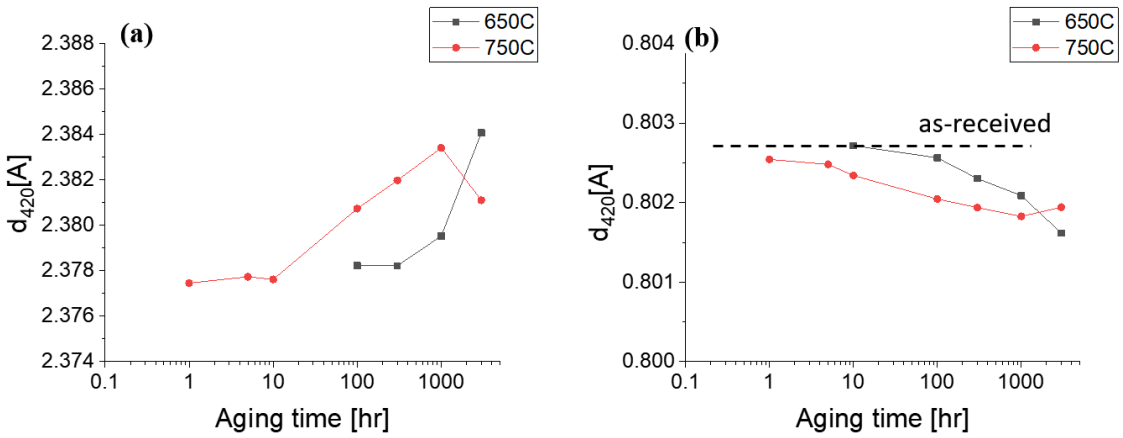

Figure 3.12: d-spacing curves of (a) $M_{23}C_6$ precipitates and (b) the austenite matrix of as a function of aging time for Alloy 709 aged at 650 and 750°C.

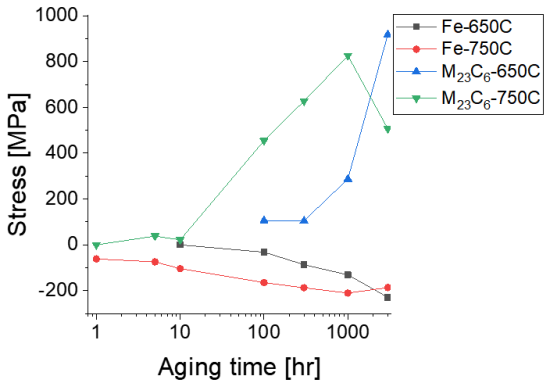

Figure 3.13: Stress curves of the austenite matrix and $M_{23}C_6$ precipitates as a function of aging time for Alloy 709 aged at 650 and 750°C.

3.3.3 Time-Temperature-Precipitation Diagram of $M_{23}C_6$

Fig. 3.14 conclusively depicts that the Time-Temperature-Precipitation (TTP) diagram of the $M_{23}C_6$ precipitate phases in Alloy 709. The TTP diagram of Alloy 709 for the temperature range of 650 - 750°C has different features in comparison with the known behaviors of the Fe-20Cr-25Ni austenitic steel class [57]. No $M_{23}C_6$ was formed until 3000 h for 550℃ aging condition, although the intergranular $M_{23}C_6$ was observed after 300 hours in the other Fe-20Cr-25Ni austenitic steel. At 650 and 750℃, the precipitation time thresholds were approximately 100 and 1 h, while those were 30 and 10 h in the other Fe-20Cr-25Ni austenitic steel.

The aging time required for the formation of the intergranular $M_{23}C_6$ on HAGBs and the lamella-shaped $M_{23}C_6$ on twin boundaries were different. The intergranular $M_{23}C_6$ precipitated out first and then the lamella-shaped $M_{23}C_6$ on the twin boundaries followed. In particular, the $M_{23}C_6$ precipitates started to form on HAGBs at 650℃ -100h and 750℃ -1h aging conditions, whereas the lamella-shaped $M_{23}C_6$ precipitates on twin boundaries did not for these conditions. In contrast to the previous works that failed to show the discriminated behaviors of the lamella-shaped $M_{23}C_6$, this finding would contribute to a better understanding of the precipitation behaviors of the intergranular $M_{23}C_6$.

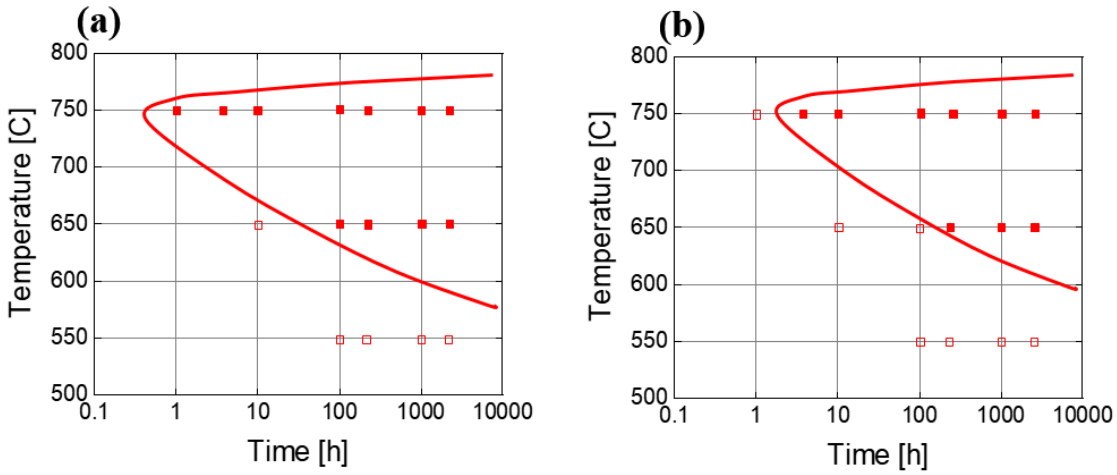

Figure 3.14: Time-Temperature-Precipitation (TTP) diagram of Alloy 709 for the temperature range 550 - 750°C: (a) $M_{23}C_6$ precipitates on HAGBs and (b) lamella-shaped $M_{23}C_6$ on twin boundaries.

CHAPTER 4

MICROSTRUCTURE OF INTERGRANULAR $M_{23}C_6$ PRECIPITATES IN AGED ALLOY 709

The second objective is to figure out the crystallographic correlation of intergranular $M_{23}C_6$ precipitates with the neighboring matrix for a better understanding of their microstructures. The results in Chapter 3 found that the morphologies of intergranular $M_{23}C_6$ precipitates were distinct between the GB types. Accordingly, the microstructures of the intergranular $M_{23}C_6$, which were distributed on the HAGBs and the twin boundaries, were investigated. This study further investigated the crystallographic characteristics of the lamella-shaped $M_{23}C_6$ on twin boundaries that has not been clearly revealed yet, although many studies found that the $M_{23}C_6$ precipitates grow with a cube - cube relationship with the austenite matrix. TEM was utilized to categorize the GB type and obtain DPs of the austenite matrix and the $M_{23}C_6$ precipitates. The analysis of the DPs was subsequently performed to uncover the crystal orientations of the $M_{23}C_6$ precipitates in comparison with those of the neighboring austenite matrix. The DF and HAADF images showed the distributions of the $M_{23}C_6$ precipitates on the HAGBs and the twin boundaries. Based on the crystallographic relations of the intergranular $M_{23}C_6$ precipitates with the neighboring austenite matrix, the schematic of the microstructures of the intergranular $M_{23}C_6$ precipitates on the HAGBs and the twin boundaries are presented.

4.1 Experimental Methods

4.1.1 Indexing of crystal poles

The zone axis is a lattice vector that is parallel to the intersecting line of a set of lattices planes, as shown in Fig. 4.1. When the lattice vector $[U\ V\ W]$ lies in the plane $(h_1\ k_1\ l_1)$ and $(h_2\ k_2\ l_2)$, $Uh_1 + Vk_1 + Wk_1 = 0$ and $Uh_2 + Vk_2 + Wk_2 = 0$. This relationship is known as Weiss Zone Law. The zone axis can be used to represent the crystal pole of a TEM specimen that lies in the reference frame of the TEM. The diffracting planes should be parallel to the incident electron beam, so the zone axis of diffraction patterns can be easily calculated using Weiss Zone Law. The observed diffraction patterns were indexed using the software tool CrysTBox to find the zone axis [61]. Since the cubic lattices have 24 rotational symmetries, the indexed zone axis of observed DPs is represented not as a particular $[U\ V\ W]$ direction but as a family of directions $<U\ V\ W>$. To calculate the rotation angle and the axis between the grains, it is critical to obtain the particular relationship between the zone axes of the specimen. This can be determined using the following equation:

$$\cos\rho = \frac{U_1U_2 + V_1V_2 + W_1W_2}{\sqrt{({U_1}^2 + {V_1}^2 + {W_1}^2)({U_2}^2 + {V_2}^2 + {W_2}^2)}} \tag{4.1}$$

Here ρ is the tilting angle between the two zone axes and can be measured from the TEM experiments. Finally, a set of three corresponding particular zone axes satisfying the equation are used to find the angles from the reference axis.

4.1.2 Calculation of rotation matrix

TEM can only obtain images of a small part of the Kikuchi map, which is not enough to directly measure the angle between the crystal poles because of its high

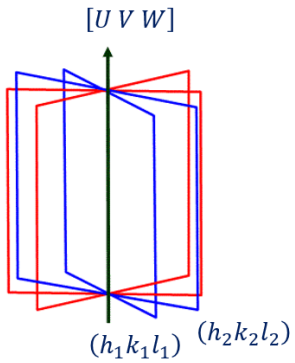

Figure 4.1: Zone axis $[U\ V\ W]$ and diffracting planes $(h_1\ k_1\ l_1)$ and $(h_2\ k_2\ l_2)$.

magnification. Therefore, the triangulation method in Jeong's work [62] was used to analyze the GB types in TEM images. After aligning the representative crystal pole in the Kikuchi map along the reference e-beam axis, symmetric DPs were indexed to find the zone axis (The zone axis of DPs is now the same as the crystal pole). These steps are repeated to measure three different zone axes and the corresponding tilting angles, which are later analyzed to find the misorientation matrix between the two neighboring grains. The detailed explanation on indexing of DPs can be found in Chapter 18.4 of Ref. [52]. Fig. 4.2 shows the schematic diagram of the reference coordinate in the Ewald sphere for calculation of the rotation matrix. Three crystal poles H1, H2, and H3 of Grain I are selected; $[U_1\ V_1\ W_1]$, $[U_2\ V_2\ W_2]$, and $[U_3\ V_3\ W_3]$. Their corresponding tilting angles are $(\alpha_1,\ \beta_1)$, $(\alpha_2,\ \beta_2)$, and $(\alpha_3,\ \beta_3)$. Indexing of Grain II also follows the same process and the parameters are listed in Table 4.1.

The triangulation method determines the relationship between the beam direction $[U_\mathrm{b}\ V_\mathrm{b}\ W_\mathrm{b}]$ and the measured crystal poles. In this method, indexed zone axes are divided by the magnitude of the vector and then inserted into the equations:

$$[U'\,V'\,W'] = [\frac{U}{\sqrt{U^2+V^2+W^2}}\frac{V}{\sqrt{U^2+V^2+W^2}}\frac{W}{\sqrt{U^2+V^2+W^2}}] \qquad (4.2)$$

The beam direction is obtained using the following equation:

$$\begin{pmatrix} U'_1 & V'_1 & W'_1 \\ U'_2 & V'_2 & W'_2 \\ U'_3 & V'_3 & W'_3 \end{pmatrix} \begin{pmatrix} U_\mathrm{b} \\ V_\mathrm{b} \\ W_\mathrm{b} \end{pmatrix} = \begin{pmatrix} \cos\gamma_1 \\ \cos\gamma_2 \\ \cos\gamma_3 \end{pmatrix} \tag{4.3}$$

where γ_1, γ_2 and γ_3 are the interpolar angles between crystal poles and the reference beam direction. The interpolar angle can be calculated in terms of tilting angles along the X-tilt and Y-tilt axes, α and β, within the Ewald sphere as a following

$$\begin{pmatrix} \cos\gamma_1 \\ \cos\gamma_2 \\ \cos\gamma_3 \end{pmatrix} = \begin{pmatrix} \cos(\alpha_1 - \alpha) + \cos(\beta_1 - \beta) - 1 \\ \cos(\alpha_2 - \alpha) + \cos(\beta_2 - \beta) - 1 \\ \cos(\alpha_3 - \alpha) + \cos(\beta_3 - \beta) - 1 \end{pmatrix} \tag{4.4}$$

Eq.4.3 and 4.4 give the beam direction;

$$\begin{pmatrix} U_\mathrm{b} \\ V_\mathrm{b} \\ W_\mathrm{b} \end{pmatrix} = \begin{pmatrix} U_1 & V_1 & W_1 \\ U_2 & V_2 & W_2 \\ U_3 & V_3 & W_3 \end{pmatrix}^{-1} \begin{pmatrix} \cos(\alpha_1 - \alpha) + \cos(\beta_1 - \beta) - 1 \\ \cos(\alpha_2 - \alpha) + \cos(\beta_2 - \beta) - 1 \\ \cos(\alpha_3 - \alpha) + \cos(\beta_3 - \beta) - 1 \end{pmatrix} \tag{4.5}$$

α and β are 0 $^\circ$ for the beam direction. Thus the beam direction is calculated as

$$\begin{pmatrix} U_\mathrm{b} \\ V_\mathrm{b} \\ W_\mathrm{b} \end{pmatrix} = \begin{pmatrix} U_1 & V_1 & W_1 \\ U_2 & V_2 & W_2 \\ U_3 & V_3 & W_3 \end{pmatrix}^{-1} \begin{pmatrix} \cos(\alpha_1) + \cos(\beta_1) - 1 \\ \cos(\alpha_2) + \cos(\beta_2) - 1 \\ \cos(\alpha_3) + \cos(\beta_3) - 1 \end{pmatrix} \tag{4.6}$$

For the X-tilt axis and the Y-tilt axis, (α, β) in Eq. 4.5 can be substituted with (0°, 90°) and (90°, 0°). These give a misorientation matrix from the reference frame of

Grain I. A rotation matrix of Grain I from the reference frame, M_I, is expressed as

$$M = \begin{pmatrix} U_{\text{X-axis}} & U_{\text{Y-axis}} & U_{\text{b}} \\ V_{\text{X-axis}} & V_{\text{Y-axis}} & V_{\text{b}} \\ W_{\text{X-axis}} & W_{\text{Y-axis}} & W_{\text{b}} \end{pmatrix} \tag{4.7}$$

Finally, a misorientation operator $\Delta M_{\text{I-II}}$ going from Grain I to Grain II can be calculated:

$$\Delta M_{\text{I-II}} = M_{\text{II}} M_{\text{I}}^{-1} \tag{4.8}$$

where M_I and M_{II} are the misorientation matrices of Grain I and Grain II in the sample reference frame.

Table 4.1: Tilting angles and indexed crystal poles of two adjacent grains

Grain	Crystal pole	Tilting angle		Grain	Crystal pole	Tilting angle	
		α	β			α	β
Grain I	$[U_1\ V_1\ W_1]$	α_1	β_1	Grain II	$[U_4\ V_4\ W_4]$	α_4	β_4
	$[U_2\ V_2\ W_2]$	α_2	β_2		$[U_5\ V_5\ W_5]$	α_5	β_5
	$[U_3\ V_3\ W_3]$	α_3	β_3		$[U_6\ V_6\ W_6]$	α_6	β_6

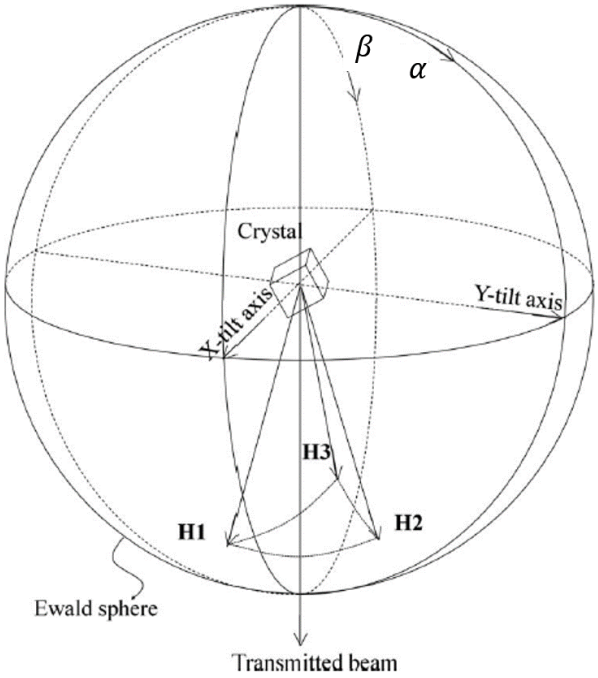

Figure 4.2: Schematic of the reference coordinate in the Ewald sphere; α and β are the tilt angle (adapted from ref. [62]).

4.2 Microstructure of As-received Alloy 709

Fig. 4.3 shows the BF images of the as-received Alloy 709 specimen (A709-AsR). Similar to the SEM results in Chapter 3, no intergranular precipitate was observed along the GBs. Several precipitates were found in the 10×10 μm specimen, indicating that the frequency of the intragranular precipitates was quite low. The intrinsic dislocations were known to provide the nucleation sites for the intragranular precipitates. The precipitate at the center in Fig. 4.3 (a) was formed on dislocations. Fig. 4.3 (c) and (d) shows a periodic network of dislocations along the GB. The dislocations on GBs were likely to provide nucleation sites for the $M_{23}C_6$ precipitates when the specimen undergoes aging [63]. The dislocation arrays were present both on the HAGBs and the twin boundaries; their width was approximately 100 nm.

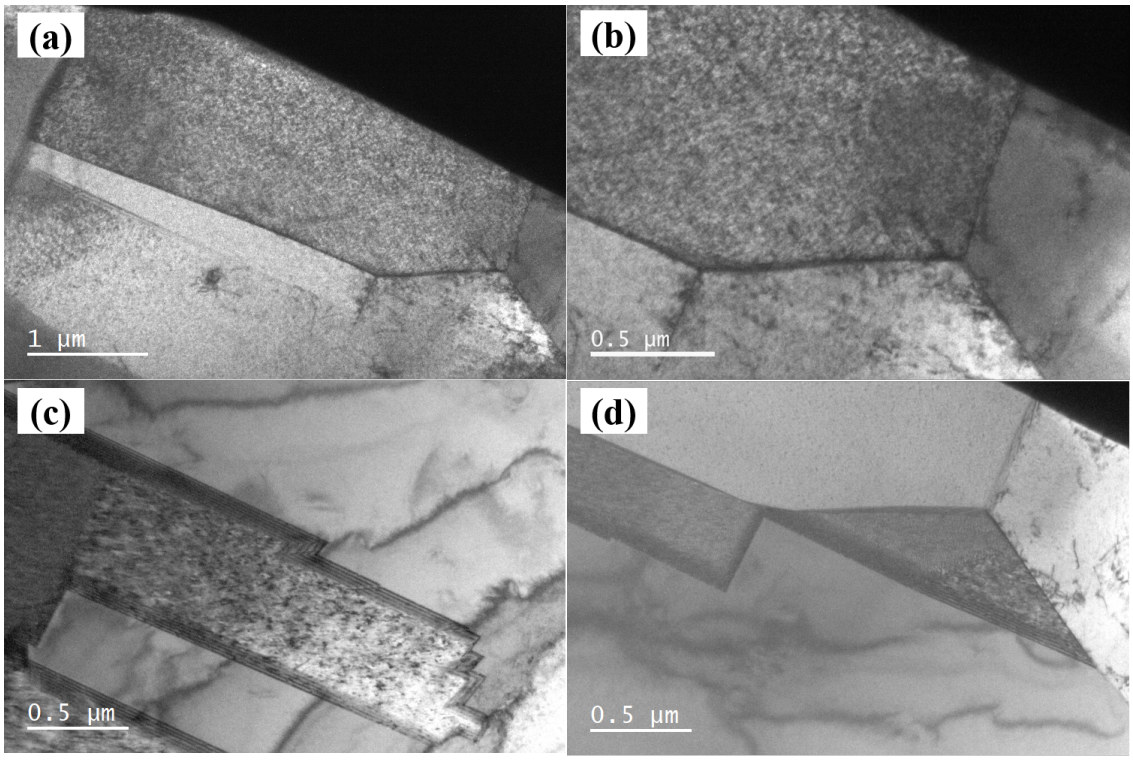

Figure 4.3: BF images of as-received Alloy 709. No intergranular precipitate was observed through the specimen. The dislocation arrays were found on the HAGBs and the twin boundaries.

4.3 Intragranular $M_{23}C_6$ Precipitates of Aged Alloy 709

The DF image in Fig. 4.4 shows distributions of the intragranular $M_{23}C_6$ in the 750°C-300h aged Alloy 709 (A709-750C300h). The image was obtained when only the electrons diffracted by the {1 1 1} plane of the intragranular $M_{23}C_6$ were allowed to pass through the objective aperture (The objective lens was located on the {1 1 1} reflection). The brightness in the image arose only from the intragranular $M_{23}C_6$ precipitates. The intragranular $M_{23}C_6$ with a diameter of approximately 50 - 150 nm were uniformly distributed throughout the specimen.

Fig. 4.5 shows the chemical and crystallographic properties of the austenite matrix and the intragranular $M_{23}C_6$ precipitates in the 750°C-300h aged Alloy 709. The iron-to-chrome (Fe-to-Cr) ratio and the nickel-to-chrome (Ni-to-Cr) ratio of the austenite matrix were identical to the value in the as-received specimen, 2.55 and 1.3, respectively (Since the carbon composition rate could not be obtained from the EDS analysis, $wt\%$ of each element was not calculated here). The EDS results of the $M_{23}C_6$ precipitate in Fig. 4.5(b) exhibit peaks of Ni and Fe next to the strongest Cr peak, indicating that Ni and Fe were present in Cr sites. The Fe-to-Cr ratio of 0.25 and the Ni-to-Cr ratio of 0.08 was similar to those under a lower aging temperature and shorter aging times, 700°C - 100 h [33, 64]. Hence, it was estimated that the partial substitution of Cr by Ni and Fe was saturated once the $M_{23}C_6$ precipitates were formed. Considering the similar composition in the austenite in previous reports, the elemental ratio in $M_{23}C_6$ after saturation seemed to depend on the nominal composition ratio of the material.

The crystallographic correlation of the intragranular $M_{23}C_6$ precipitates and the austenite matrix in Alloy 709 are shown in Figs. 4.6 (a) and (b), respectively. As explained in Chapter 2.2.1, the orientation of the DPs of the intragranular $M_{23}C_6$ was the same as that of the austenitic matrix; the spacing between the DPs was one-third that of the austenite. Considering the result in Chapter 3.3 that the $a_{\gamma\text{-Fe}}/a_{M_{23}C_6}$

was not an integer in the Alloy 709 specimens, it was likely that localized strains were formed near $M_{23}C_6$ due to lattice mismatch and that the intragranular $M_{23}C_6$ precipitates shared a semicoherent interface with the neighboring austenite grain.

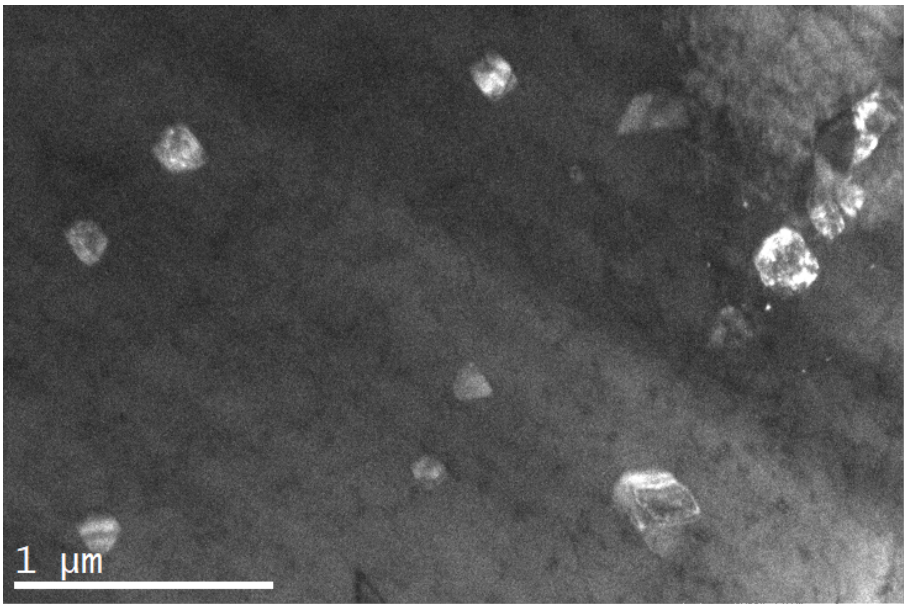

Figure 4.4: Dark field image of intragranular $M_{23}C_6$ embedded in the austenite matrix in Alloy 709 aged at 750°C for 300 h. The objective aperture was located on the (1 1 1) reflection of the intragranular $M_{23}C_6$ so that the brightness arose from that the (1 1 1) plane.

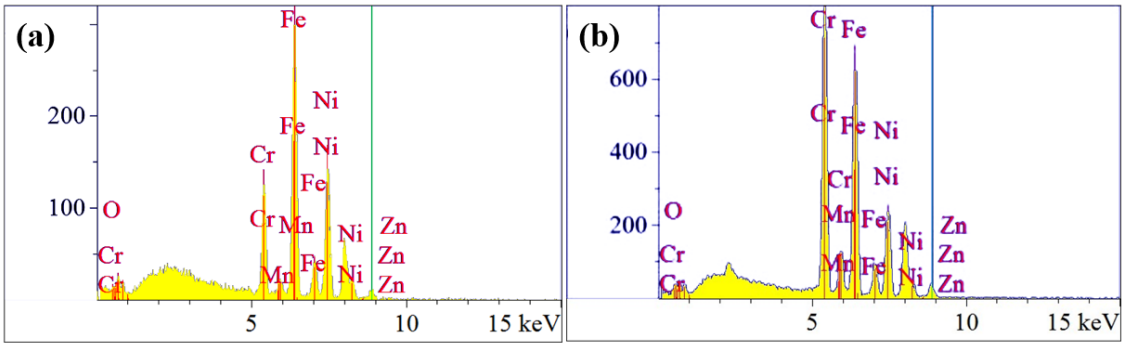

Figure 4.5: EDS spectrum of (a) austenite and (b) intragranular $M_{23}C_6$ in Alloy 709 aged at 750°C for 300 h. Peaks of Ni and Fe were observed next to the strongest Cr peak in (b), exhibiting the partial substitution of Cr by Ni and Fe in $M_{23}C_6$ precipitates.

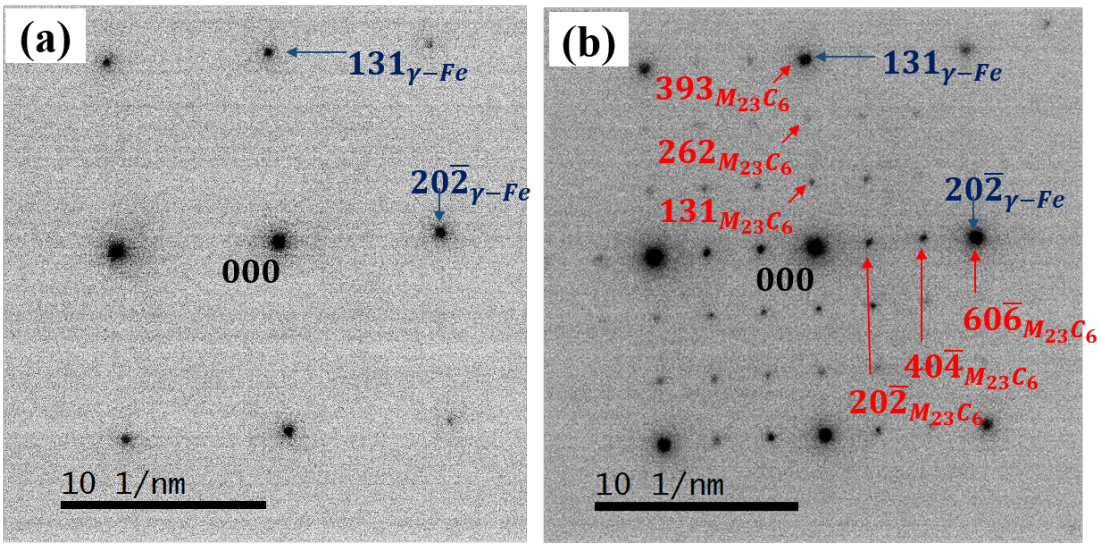

Figure 4.6: DPs of (a) austenite and (b) intragranular $M_{23}C_6$ in Alloy 709 aged at 750°C for 300 h. The DPs of intragranular $M_{23}C_6$ mixed in the DPs of the austenite matrix, indicating that $M_{23}C_6$ has an identical crystal structure to that of austenite and $3 \cdot a_{M_{23}C_6} = a_{\gamma\text{-Fe}}$. The contrast of DPs was inverted for clarity.

4.4 $M_{23}C_6$ Precipitates on HAGBs in Alloy 709

Fig. 4.7 shows the stitched BF images of the 750°C-3000 h aged Alloy 709 specimen (A709-750C3000h). The GB between Grain I (lower) and Grain II (upper) was located in the center of the image. $M_{23}C_6$ precipitates were distributed along the GB, which was determined as a HAGB. The elongated shape of intragranular $M_{23}C_6$ along the GB suggested that the growing speed alongside GBs was higher than that towards the austenite matrix. Intragranular $M_{23}C_6$ was scattered inside the grains and observed on dislocations.

4.4.1 Determination of grain boundary type

After aligning three crystal poles of Grain I and Grain II in Fig. 4.7, the DPs of each grain were indexed as shown in Fig. 4.8. For Grain I, the measured tilting angle of H_1-H_2, H_2-H_3 and H_3-H_1 were 26.2°, 17.3° and 30.9°; <1 0 1>, <2 1 1> and <3 2 3> were indexed as zone axes for each crystal pole. Possible particular crystal poles of each family were inserted into Eq.4.1 to check if the angles between them match to the measured tilting angle. A set of [1 0 1], [3 $\overline{2}$ 3], and [2 $\overline{1}$ 1] gave 25.2°([1 0 1]-[3 $\overline{2}$ 3]), 16.8°([3 $\overline{2}$ 3]-[2 $\overline{1}$ 1]), and 30.0° ([2 $\overline{1}$ 2]-[1 0 1]) with the minimum errors. Therefore, H_1, H_2, and H_3 was determined to be [1 0 1], [3 $\overline{2}$ 3], and [2 $\overline{1}$ 1], respectively. The analysis of Grain II also followed the identical steps.

The indexed crystal orientations and the corresponding tilting angles of Grain I and Grain II are listed in Table 4.2; they were used to calculate a misorientation matrix between Grains I and II. Eq. 4.6 gave the beam directions for each reference axis:

$$\begin{pmatrix} U_{\text{X-axis}} \\ V_{\text{X-axis}} \\ W_{\text{X-axis}} \end{pmatrix} = \begin{pmatrix} \frac{1}{\sqrt{2}} & 0 & \frac{1}{\sqrt{2}} \\ \frac{3}{\sqrt{22}} & \frac{-2}{\sqrt{22}} & \frac{3}{\sqrt{22}} \\ \frac{2}{\sqrt{6}} & \frac{-1}{\sqrt{6}} & \frac{1}{\sqrt{6}} \end{pmatrix}^{-1} \begin{pmatrix} \cos(-5.4) + \cos(-0.1 - 90) - 1 \\ \cos(14.6) + \cos(-17.3 - 90) - 1 \\ \cos(25.3) + \cos(-3.7 - 90) - 1 \end{pmatrix} \quad (4.9)$$

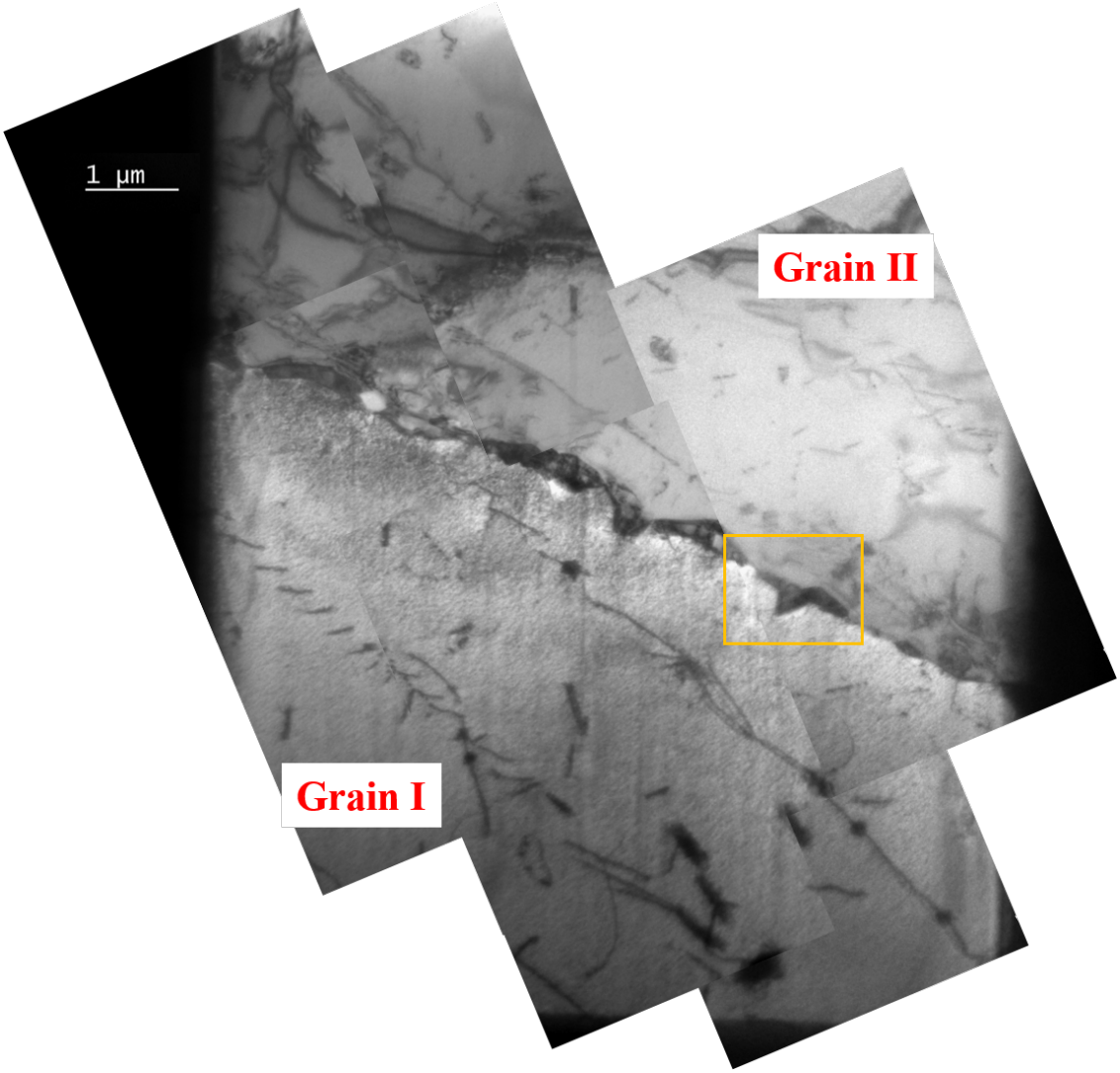

Figure 4.7: Stitched BF images of the Alloy 709 aged at 750℃ for 3000 h. A HAGB between two austenite grains was observed in the center of the image and a series of $M_{23}C_6$ was formed on the HAGB. The region marked with a yellow box was enlarged in Fig. 4.9 for a further analysis.

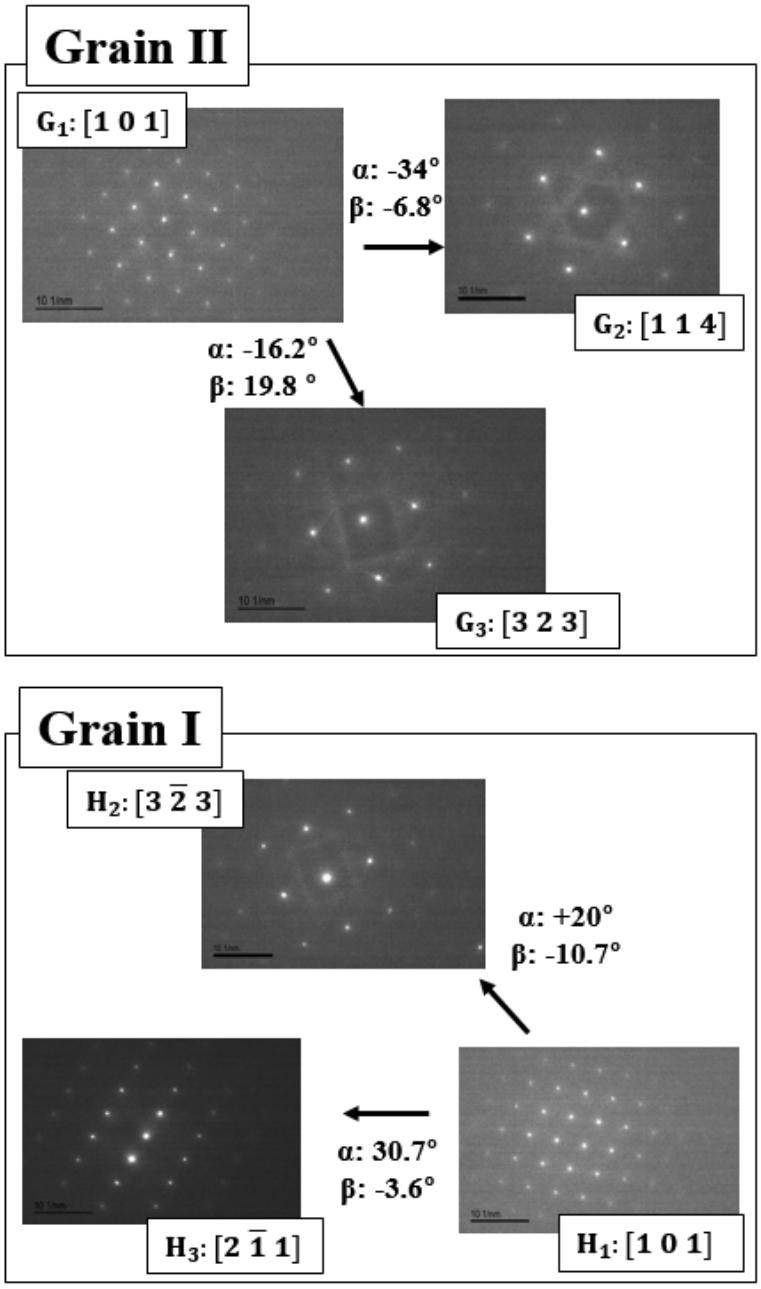

Figure 4.8: Indexed crystal planes of Grain I and Grain II in Fig. 4.7. Crystal poles of [1 0 1], [3 $\overline{2}$ 3], and [2 $\overline{1}$ 1] were indexed for Grain I. [1 0 1], [1 1 4], and [3 2 3] were for in Grain II. Tilting angles between crystal poles was consistent with theoretical values of 25.2°, 16.8° and 30.0°.

$$\begin{pmatrix} U_{\text{Y-axis}} \\ V_{\text{Y-axis}} \\ W_{\text{Y-axis}} \end{pmatrix} = \begin{pmatrix} \frac{1}{\sqrt{2}} & 0 & \frac{1}{\sqrt{2}} \\ \frac{3}{\sqrt{22}} & \frac{-2}{\sqrt{22}} & \frac{3}{\sqrt{22}} \\ \frac{2}{\sqrt{6}} & \frac{-1}{\sqrt{6}} & \frac{1}{\sqrt{6}} \end{pmatrix}^{-1} \begin{pmatrix} \cos(-5.4-90)+\cos(-0.1)-1 \\ \cos(14.6-90)+\cos(-17.3)-1 \\ \cos(25.3-90)+\cos(-3.7)-1 \end{pmatrix} \tag{4.10}$$

$$\begin{pmatrix} U_{\text{b}} \\ V_{\text{b}} \\ W_{\text{b}} \end{pmatrix} = \begin{pmatrix} \frac{1}{\sqrt{2}} & 0 & \frac{1}{\sqrt{2}} \\ \frac{3}{\sqrt{22}} & \frac{-2}{\sqrt{22}} & \frac{3}{\sqrt{22}} \\ \frac{2}{\sqrt{6}} & \frac{-1}{\sqrt{6}} & \frac{1}{\sqrt{6}} \end{pmatrix}^{-1} \begin{pmatrix} \cos(-5.4)+\cos(-0.1)-1 \\ \cos(14.6)+\cos(-17.3)-1 \\ \cos(25.3)+\cos(-3.7)-1 \end{pmatrix} \tag{4.11}$$

A misorientation matrix of grain I from the reference frame, M_I, was given by Eq.4.7:

$$M_{\text{I}} = \begin{pmatrix} -0.006 & -0.094 & 0.996 \\ -0.330 & 0.207 & 0.922 \\ -0.160 & 0.425 & 0.902 \end{pmatrix} \tag{4.12}$$

M_{II} was also calculated using Eq.4.6; finally, Eq.4.8 gave $\Delta M_{I\text{-}II}$ as followings,

$$M_{\text{II}} = \begin{pmatrix} -0.190 & 0.267 & 0.949 \\ -0.315 & -0.342 & 0.915 \\ 0.193 & -0.019 & 0.981 \end{pmatrix} \tag{4.13}$$

$$\Delta M_{\text{I-II}} = \begin{pmatrix} 0.856 & 0.292 & 0.485 \\ -0.326 & 0.958 & 0.092 \\ -0.09 & 0.183 & 0.605 \end{pmatrix} \tag{4.14}$$

The particular rotation axis was [-0.09, 0.577, -0.618] $\sim$ [0 1 -1] with the rotation angle of 44.81°. Since there was no matching rotation axis and angle to any CSLB conditions [26], the boundary between them was categorized as the HAGB.

Table 4.2: Measured tilting angle and indexed crystal pole of Grain I and Grain II in Fig. 4.9.

Crystal	Crystal pole	Tilting angle		Crystal	Crystal pole	Tilting angle	
		α	β			α	β
Grain I	[1 0 1]	-5.4	-0.1	Grain II	[1 0 1]	16.2	-8.7
	[3 $\overline{2}$ 3]	14.6	-17.3		[1 1 4]	-17.8	-15.5
	[2 $\overline{1}$ 1]	25.3	-3.7		[3 2 3]	0	11.1

4.4.2 Microstructure of $M_{23}C_6$ Precipitates on HAGBs in Alloy 709

Fig. 4.9 (a) and (b) shows the detailed morphology of $M_{23}C_6$ precipitates on the HAGB in the 750°C-3000 h aged sample. The image was taken from the region marked with a yellow box in Fig. 4.8. The $M_{23}C_6$ precipitates were semi-continuously distributed along the HAGB. The pointed region of the intergranular $M_{23}C_6$ precipitate (marked in dashed circles) grew approximately 200 nm from the GB towards Grain I. Besides this region, this precipitate, with a width of approximately 100 nm, grew up to 500 nm in length alongside the GB.

The specimen was tilted so that the (1 0 1) zone axis of Grain II was parallel to the beam direction in order to reveal coherency between the grains. Fig. 4.10 (a)-(d) shows the DPs of Grain I, intergranular $M_{23}C_6$, the interface of intergranular $M_{23}C_6$ with Grain II, and Grain II, respectively. The DPs from Grain I in Fig. 4.10 (a) showed no crystal correlation in comparison to the DPs arising from the intergranular $M_{23}C_6$ in Fig. 4.10 (b). When the selected area diffraction (SAD) aperture was moved to the interface of intergranular $M_{23}C_6$ and Grain II, the (0 $\overline{6}$ 0) and ($\overline{3}$ 3 3) reflections of $M_{23}C_6$ were excited due to the strong beam arising from the (0 $\overline{2}$ 0) and ($\overline{1}$ 1 1) planes of the austenite matrix, as seen in Fig. 4.10 (c). The presence of a weak reflection from the precipitate disappeared when the aperture moved to the austenite matrix of Grain II, as shown in Fig. 4.10(d). This confirmed that the intergranular $M_{23}C_6$ was nucleated in a lattice correspondence with Grain II and then grew into the incoherent matrix, i.e. Grain I. The growing preference

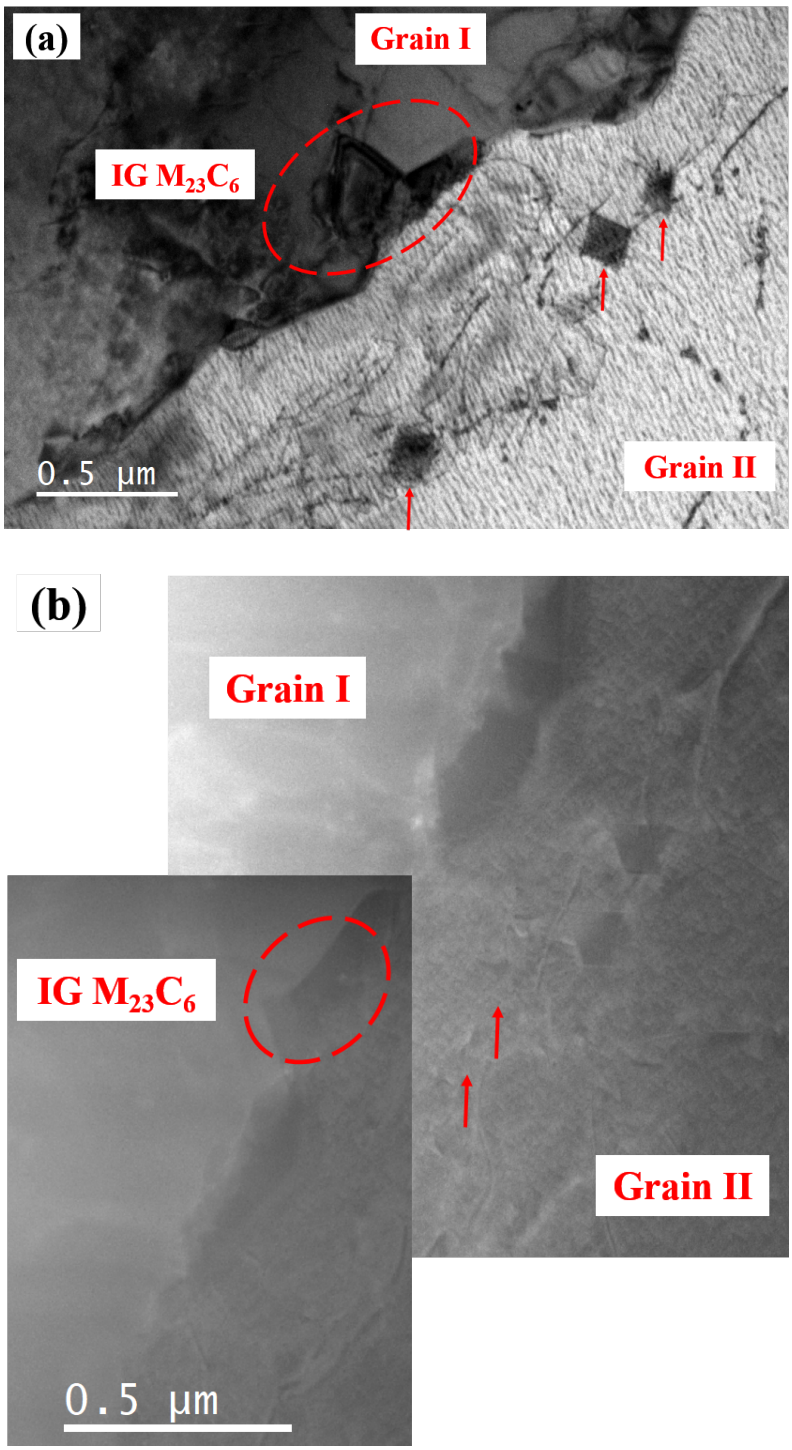

Figure 4.9: (a) BF image and (b) HAADF image of $M_{23}C_6$ precipitates on the HAGB in Alloy 709 aged at 750℃-3000h (A709-750C3000h). The images were taken from the yellow box in Fig. 4.7.

of the intergranular $M_{23}C_6$ in Alloy 709 was identical to the known behaviors of intergranular $M_{23}C_6$ in other austenitic steels or Ni-based alloys [42,43,65]. Kaneko et al. explained that the preferential migration of intergranular $M_{23}C_6$ towards incoherent matrices is caused by the high interfacial energy of the incoherent interface of the intergranular $M_{23}C_6$ precipitate with the austenite [42].

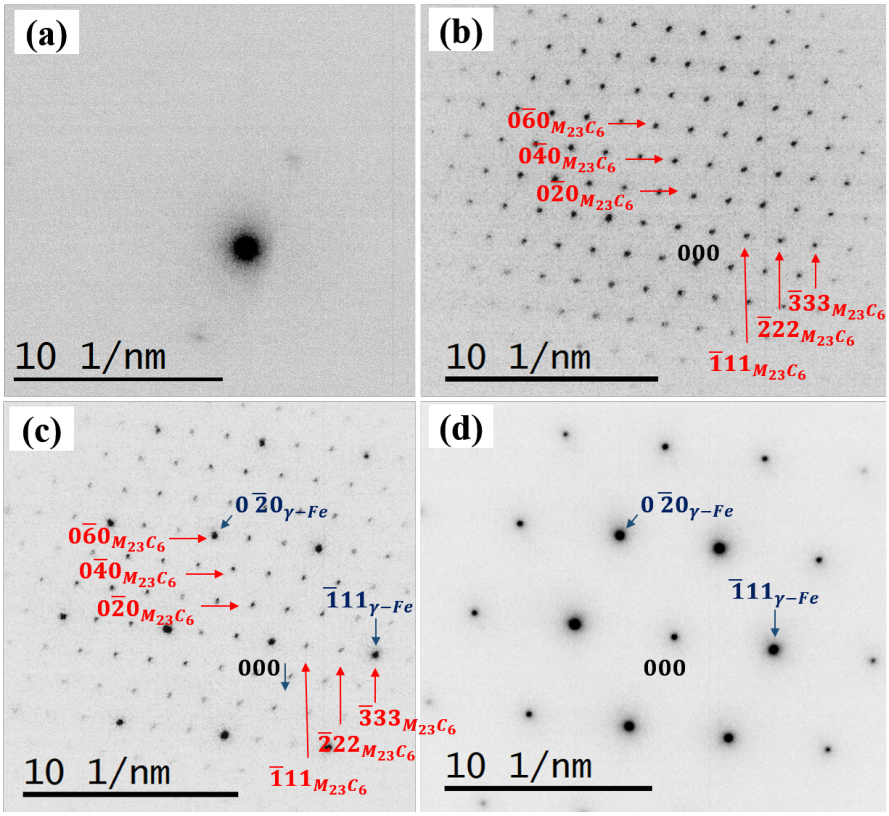

Figure 4.10: DPs of (a) Grain I, (b) intergranular $M_{23}C_6$, (c) the interface of intergranular $M_{23}C_6$ and Grain II, and (d) Grain II in Fig. 4.9. All DPs were taken when the (1 0 1) zone axis of Grain II was parallel to the beam direction. The contrast was inverted for clarity.

4.4.3 Distributions of $M_{23}C_6$ on HAGBs in Alloy 709

Fig. 4.11 shows the DF image when the electrons from the (1 1 0) reflection of the $M_{23}C_6$ precipitates were allowed to pass the objective aperture. Only electrons diffracted from the (1 1 0) plane of the $M_{23}C_6$ precipitates in Grain I contributed to the brightness in the image because the sample was tilted along the <1 0 1> zone axis of Grain I. The intragranular $M_{23}C_6$ precipitates in Grain I (marked with yellow arrows) and the intergranular $M_{23}C_6$ precipitates (marked with blue arrows) were in white color, indicating that their crystal orientation and lattice parameters were identical. Considering that the intragranular $M_{23}C_6$ precipitates are coherent, it was confirmed that the intergranular $M_{23}C_6$ precipitates shared coherent interfaces with Grain I and grew from Grain I toward Grain II. Based on the observation of the flat interface in the as-received specimen in Fig. 4.3, the estimated original GB before aging was likely to be flat, which was drawn in a green dashed line in the image. It could be concluded that the intergranular $M_{23}C_6$ precipitates within Grain II was nucleated on the HAGBs in a coherency with Grain I that is a parent grain.

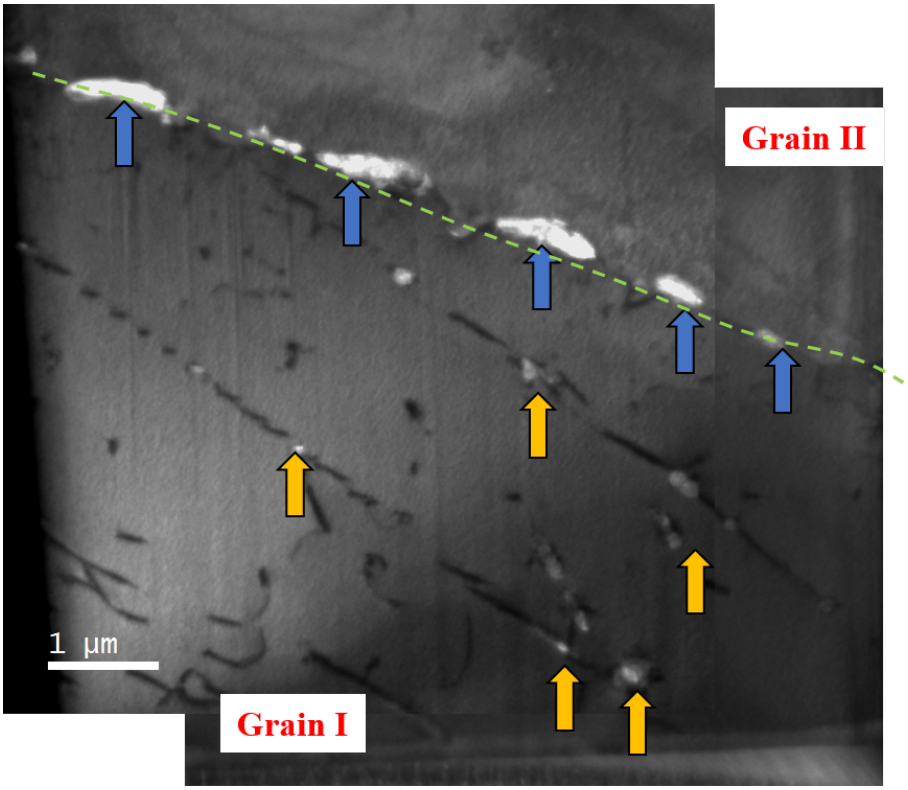

Figure 4.11: DF image of aged Alloy 709 at 750℃ for 3000 h. The image was taken when reflections form planes other than (1 1 0) reflection of $M_{23}C_6$ precipitates was blocked. The brightness is arising only from (1 1 0) plane of $M_{23}C_6$. Note that the brightness in Fig. 4.7(BF images) came from phase and thickness.

4.4.4 Intragranular $M_{23}C_6$ near HAGBs of Alloy 709

The precipitate free zone was observed near the HAGB in Fig. 4.9 (a). The GBs acted as solute sinks so that the regions adjacent to the boundary was unable to nucleate the precipitates. The width of the precipitate free zone, the distance from the GB to the intragranular $M_{23}C_6$ precipitates, was approximately 500 nm. Next to the precipitate free zone, the intragranular $M_{23}C_6$ with a size of approximately 100 nm were distributed on the dislocations. The g·b analysis was performed using four TEM images with various zones axes to reveal the characteristics of the dislocations where the precipitate was formed (marked with a blue arrow), as shown in Fig. 4.12. The dislocations were not shown when the g-vector was $< 1\ 1\ \overline{1} >$ and $< \overline{2}\ 0\ 0 >$. These conditions gave the following equations because dislocations could not be seen when g·b = 0.

$$g_1 \cdot b =< 1\ 1\ \overline{1} > \cdot < b_1\ b_2\ b_3 >= 0 \tag{4.15}$$

$$g_1 \cdot b =< \overline{2}\ 0\ 0 > \cdot < b_1\ b_2\ b_3 >= 0 \tag{4.16}$$

Eq.4.15 and 4.16 were reduced to $b_1+b_2-b_3=0$ and $b_1=0$. Then,

$$b =< 0\ b_2\ b_2 > \| < 0\ 1\ 1 > \tag{4.17}$$

<1 1 1> is one of equivalents of [1 1 0]; therefore, the result confirmed that the dislocation in Fig. 4.12 had a Burgers vector of $\frac{a}{2}$[1 1 0], which provides typical nucleation sites of the intergranular $M_{23}C_6$ in austenitic steels.

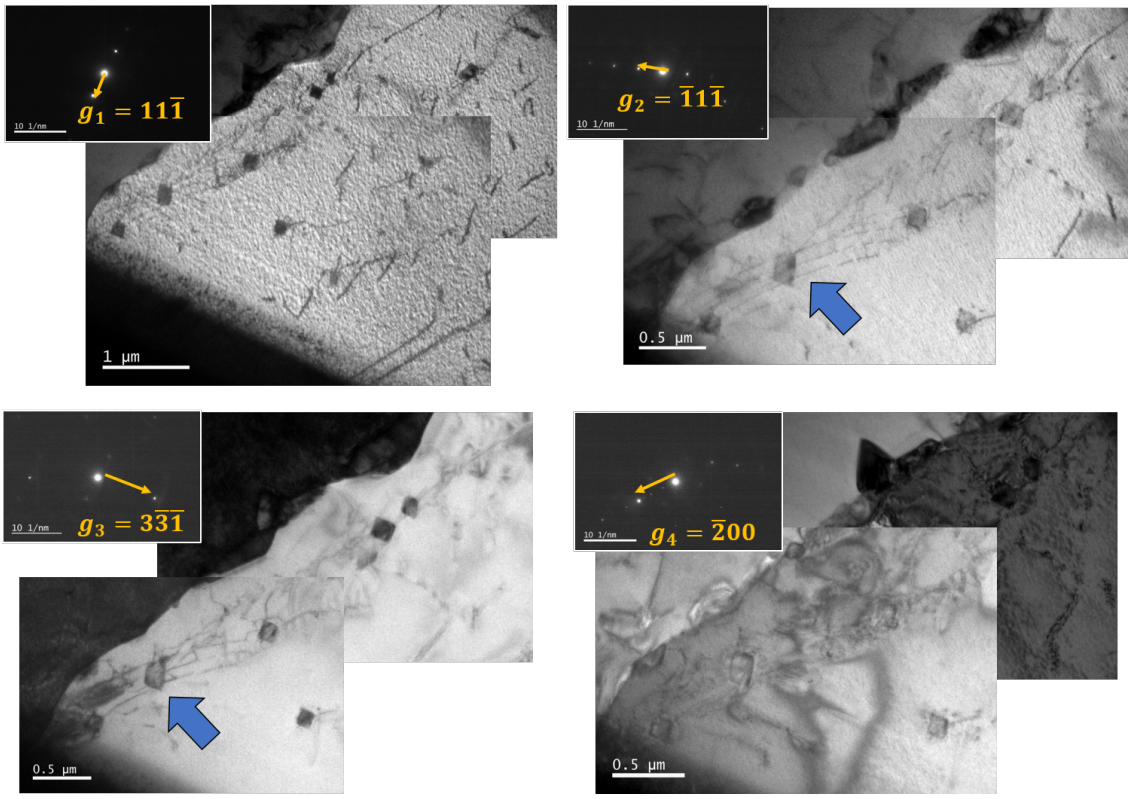

Figure 4.12: BF images of dislocations near the HAGB in Fig. 4.7. The specimen was aged at the 750°C for 300 h (A709-750C300h).

4.5 $M_{23}C_6$ Precipitates on Twin Boundary in Alloy 709

Fig. 4.13 shows the morphology of $M_{23}C_6$ precipitates distributed near the twin boundary in the Alloy 709 specimen aged at 750°C for 300 h (A709-750C300h). Lamella-shaped $M_{23}C_6$ were distributed near the twin boundaries. These precipitates, with a width of 50 - 150 nm, grew to approximately 500 nm in length and were confined within a distance 5 μm from the twin boundary. The growing direction was parallel to the coherent twin boundary. The DPs (shown in Fig. 4.15 and discussed below) of the lamella-shaped precipitates confirmed that they also had a lattice correspondence of $3 \cdot a_{M_{23}C_6} \approx a_{\gamma\text{-Fe}}$ with the neighboring austenite matrix.

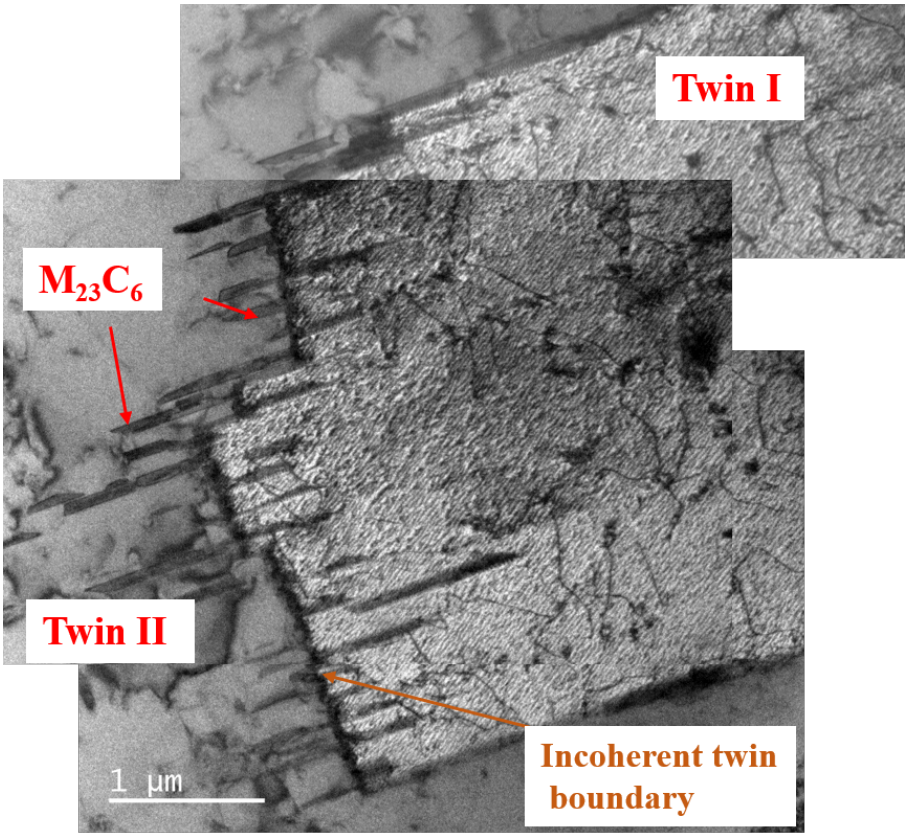

Figure 4.13: BF image of twin boundaries in Alloy 709 aged at 750°C for 3000h (A709-750C3000h).

4.5.1 Determination of Grain Boundary Type

The misorientation matrix between the neighboring grains in Fig. 4.13 was calculated using the values in Table 4.3, which were calculated in the same way in Chapter4.4.1

Table 4.3: Measured tilting angle and indexed crystal pole of grains in Fig. 4.14.

Crystal	Crystal pole	Tilting angle		Crystal	Crystal pole	Tilting angle	
		α	β			α	β
Twin I	[0 1 1]	11.4	-2	Twin II	[0 1 1]	-20.7	-4.9
	[1 4 5]	4.7	-10.5		[$\bar{2}$ 10 5]	0.8	9.5
	[1 2 2]	-16.1	12.5		[$\bar{1}$ 3 2]	19.9	-4.6

Equation 4.6 gave the beam directions for each reference axis:

$$\begin{pmatrix} U_{\text{X-axis}} \\ V_{\text{X-axis}} \\ W_{\text{X-axis}} \end{pmatrix} = \begin{pmatrix} \frac{1}{\sqrt{2}} & 0 & \frac{1}{\sqrt{2}} \\ \frac{3}{\sqrt{22}} & \frac{-2}{\sqrt{22}} & \frac{3}{\sqrt{22}} \\ \frac{2}{\sqrt{6}} & \frac{-1}{\sqrt{6}} & \frac{1}{\sqrt{6}} \end{pmatrix}^{-1} \begin{pmatrix} \cos(-5.4) + \cos(-0.1 - 90) - 1 \\ \cos(14.6) + \cos(-17.3 - 90) - 1 \\ \cos(25.3) + \cos(-3.7 - 90) - 1 \end{pmatrix} \quad (4.18)$$

,

$$\begin{pmatrix} U_{\text{Y-axis}} \\ V_{\text{Y-axis}} \\ W_{\text{Y-axis}} \end{pmatrix} = \begin{pmatrix} \frac{1}{\sqrt{2}} & 0 & \frac{1}{\sqrt{2}} \\ \frac{3}{\sqrt{22}} & \frac{-2}{\sqrt{22}} & \frac{3}{\sqrt{22}} \\ \frac{2}{\sqrt{6}} & \frac{-1}{\sqrt{6}} & \frac{1}{\sqrt{6}} \end{pmatrix}^{-1} \begin{pmatrix} \cos(-5.4 - 90) + \cos(-0.1) - 1 \\ \cos(14.6 - 90) + \cos(-17.3) - 1 \\ \cos(25.3 - 90) + \cos(-3.7) - 1 \end{pmatrix} \quad (4.19)$$

,

$$\begin{pmatrix} U_{\text{b}} \\ V_{\text{b}} \\ W_{\text{b}} \end{pmatrix} = \begin{pmatrix} \frac{1}{\sqrt{2}} & 0 & \frac{1}{\sqrt{2}} \\ \frac{3}{\sqrt{22}} & \frac{-2}{\sqrt{22}} & \frac{3}{\sqrt{22}} \\ \frac{2}{\sqrt{6}} & \frac{-1}{\sqrt{6}} & \frac{1}{\sqrt{6}} \end{pmatrix}^{-1} \begin{pmatrix} \cos(-5.4) + \cos(-0.1) - 1 \\ \cos(14.6) + \cos(-17.3) - 1 \\ \cos(25.3) + \cos(-3.7) - 1 \end{pmatrix} \quad (4.20)$$

A misorientation matrix of grain I from the reference frame, M_I, was given by

Eq.4.7

$$M_{\mathrm{I}} = \begin{pmatrix} -0.215 & 0.217 & 0.954 \\ -0.204 & 0.475 & 0.875 \\ -0.014 & 0.167 & 0.986 \end{pmatrix} \tag{4.21}$$

Finally, M_{II} and $\Delta M_{I\text{-}II}$ were calculated using Eq.4.6-4.8:

$$M_{\mathrm{II}} = \begin{pmatrix} -0.069 & 0.479 & 0.876 \\ -0.262 & 0.323 & 0.919 \\ 0.095 & 0.320 & 0.932 \end{pmatrix} \tag{4.22}$$

$$\Delta M_{\mathrm{I\text{-}II}} = \begin{pmatrix} 0.694 & 0.384 & -0.564 \\ -0.606 & 0.677 & -0.356 \\ 0.283 & 0.643 & 0.627 \end{pmatrix} \tag{4.23}$$

The rotation axis was [0.999, -0.847, -0.989], which was (approximately) a particular vector of the twin boundary rotation axis, [1 1 1]. The rotation angle was calculated to be 60.1°. The difference from the exact twin rotation angle of 60°, θ_{m} (60 - 60.1 = -0.1°), was less than the maximum allowed deviation angle for the twin boundaries in the CSL model ($\frac{15}{3^{1/2}} = 8.66$ °); therefore, the twinning relationship between the two grains was verified.

4.5.2 Microstructure of $M_{23}C_6$ precipitates near twin boundary

The specimen was tilted along the (1 1 2) zone axis of Twin I to check coherency. The DPs from Twin I were indexed in Fig. 4.15(a). Fig. 4.15(b) shows the DPs from the lamella-shaped $M_{23}C_6$ within Twin I, $(M_{23}C_6)_I$. The DPs of all the lamella-shaped $M_{23}C_6$ precipitate within Twin I were identical to each other so that their crystal orientations were parallel to each other. If $(M_{23}C_6)_I$ had coherency with Twin I, the orientation of the DPs from $(M_{23}C_6)_I$ should have been in the (1 1 $\overline{1}$) and ($\overline{2}$ 2 0) directions; however, the DPs in Fig. 4.15(b) were present along the diagonal direction, which was the orientation of reflections of Twin II in Fig. 4.15(c). The excited reflections in Fig. 4.15(c) was identified as one from the {1 1 3} plane family using the d-spacing value. Fig. 4.15(d) shows that the DPs from the lamella-shaped $M_{23}C_6$ within Twin II, $(M_{23}C_6)_{II}$, appeared in the (1 1 $\overline{1}$) and ($\overline{2}$ 2 0) directions, which were the orientation of the DPs from Twin I in Fig. 4.15(a). The observation of the coherency of Twin I with $(M_{23}C_6)_{II}$ and Twin II with $(M_{23}C_6)_I$ indicated that the lamella-shaped $M_{23}C_6$ precipitates near the twin boundaries had a different crystal orientation from the neighboring matrix. In the early stage of precipitation, fine equiaxed $M_{23}C_6$ precipitates were formed on the incoherent twin boundary [46]. Taking this into account, the observed coherency correlation would lead to the conclusion that the fine $M_{23}C_6$ precipitates on the twin boundaries have the cube-cube relation with one of twinning matrices (the parent matrix) and then grow towards the opposite side (the twinning matrix) in the shape of lamella. In particular, $(M_{23}C_6)_{II}$ precipitates grew towards Twin II (the twinning matrix), keeping the continuous lattice planes with Twin I (the parent matrix). Although the energy of the interface of the precipitate with the twinning matrix is extremely low, it is higher than zero interfacial energy of the precipitate-parent matrix interface where no lattice change is present. This would determine the preferential growing toward the twinning matrix, as similar

to the behavior of intergranular $M_{23}C_6$ precipitates on the HAGBs. Some $M_{23}C_6$ looked like it grew towards both matrices; however, the contrast variation inside the precipitate suggested two separate precipitates overlapped. Moiré fringes were observed in the vicinity of the lamella-shaped $M_{23}C_6$ precipitates due to misfit dislocations around the precipitates. The width of the Moiré fringes indicated that strain fields around the precipitates extended to several tens of nanometers. As discussed above, $a_{\gamma\text{-Fe}}/a_{M_{23}C_6}$ was not exactly 3 so that the lattice mismatch probably caused the strains in the region near the interface between the lamella-shaped $M_{23}C_6$ and the austenite matrix.

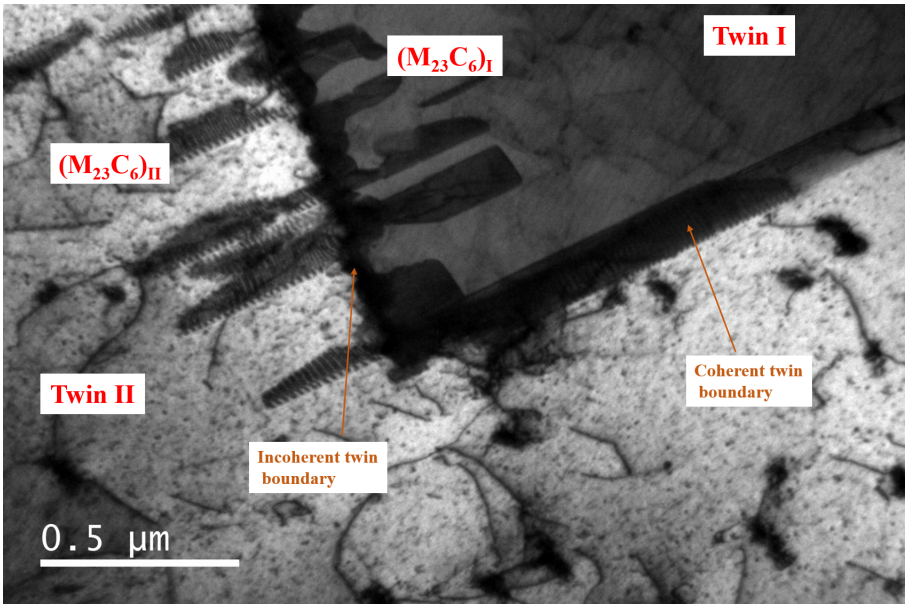

Figure 4.14: BF image of lamella-shaped $M_{23}C_6$ precipitates on the twin boundaries in Alloy 709 aged at 750°C for 3000h (A709-750C3000h).

4.5.3 Distributions of precipitates near twin boundaries

After tilting the specimen along the [1 1 2] zone axis of the twinning matrix, the DF image in Fig. 4.16 was taken. The identical methodologies in the previous chapter were used here. The white contrast in the image arose from $(M_{23}C_6)_{II}$

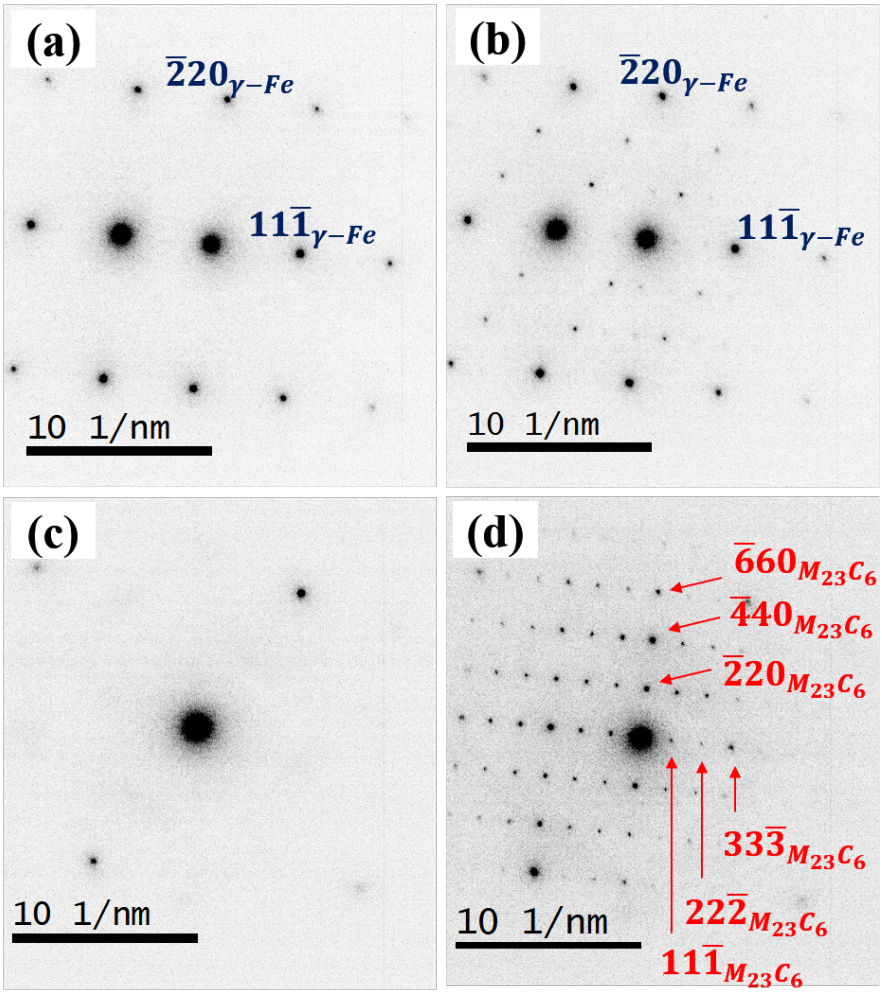

Figure 4.15: DPs of (a) Twin I, (b) $M_{23}C_6)_I$, (c) Twin II, and $M_{23}C_6)_{II}$. The contrast was inverted for clarity.

because only the (1 1 $\bar{1}$) reflection of $(M_{23}C_6)_{II}$ was allowed to pass through the objective aperture. It was apparent that the lamella-shaped $M_{23}C_6$ precipitates had an identical crystal orientation. All of them also shared a coherent interface with Twin I.

Fine intergranular $M_{23}C_6$ precipitates, with a size range of 30 - 60 nm, were observed on the incoherent twin boundary. Their DPs, exclusive of other regions, could not be obtained since the precipitates were so small. The crystal orientation should be identical to either $(M_{23}C_6)_I$ or $(M_{23}C_6)_{II}$ because there were no additional DPs other than the DPs of $(M_{23}C_6)_I$ and $(M_{23}C_6)_{II}$ when the SAD aperture was located on the incoherent twin boundary. The explanation of why only some of these precipitates grew in the shape of a lamella is not yet clear.

The EDS mapping performed in Fig. 4.17 showed the Cr, Fe and Ni distribution across the twin boundary. The Cr distribution exhibited the development of the lamella-shaped $M_{23}C_6$ precipitates on the coherent twin boundary, contradicting previous studies showing the absence of carbides on the coherent twin boundaries [56, 66]. Lewis et al. also found that the $M_{23}C_6$ precipitates developed along the coherent twin boundary in the early stage of precipitation [41]. The observations in this study provided additional pieces of evidence for the precipitation on the coherent twin boundaries. The precipitates grew up to 800 nm in length, with approximately 100 nm in width. The DPs of the $M_{23}C_6$ precipitates on the coherent twin boundary (not shown here) were identical to those of the lamella-shaped $M_{23}C_6$, implying the crystal orientation and the lattice constant of these precipitates were identical to each other. Considering the shape and the growing direction of the $M_{23}C_6$ precipitates on the coherent twin boundary, their precipitation behavior was thought to be identical to that of the lamella-shaped $M_{23}C_6$ on the incoherent twin boundaries.

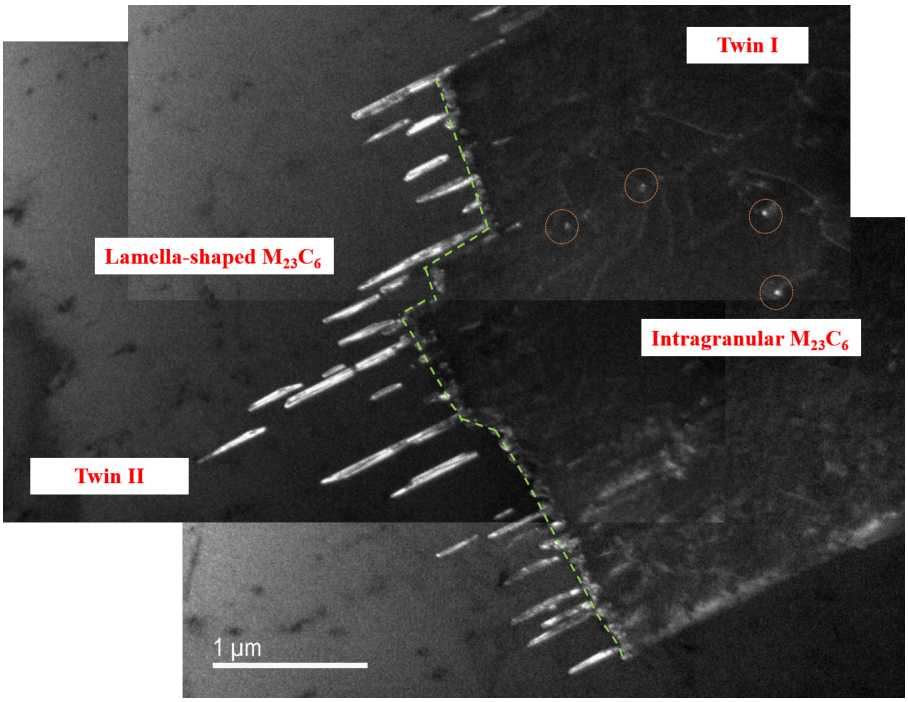

Figure 4.16: Stitched DF images of Alloy 709 aged at 750°C for 3000h (A709-750C3000h). The images were taken when reflections other than the (1 1 $\overline{1}$) reflection of $M_{23}C_6$ precipitates was blocked. The brightness arose only from (1 1 $\overline{1}$) plane of $M_{23}C_6$.

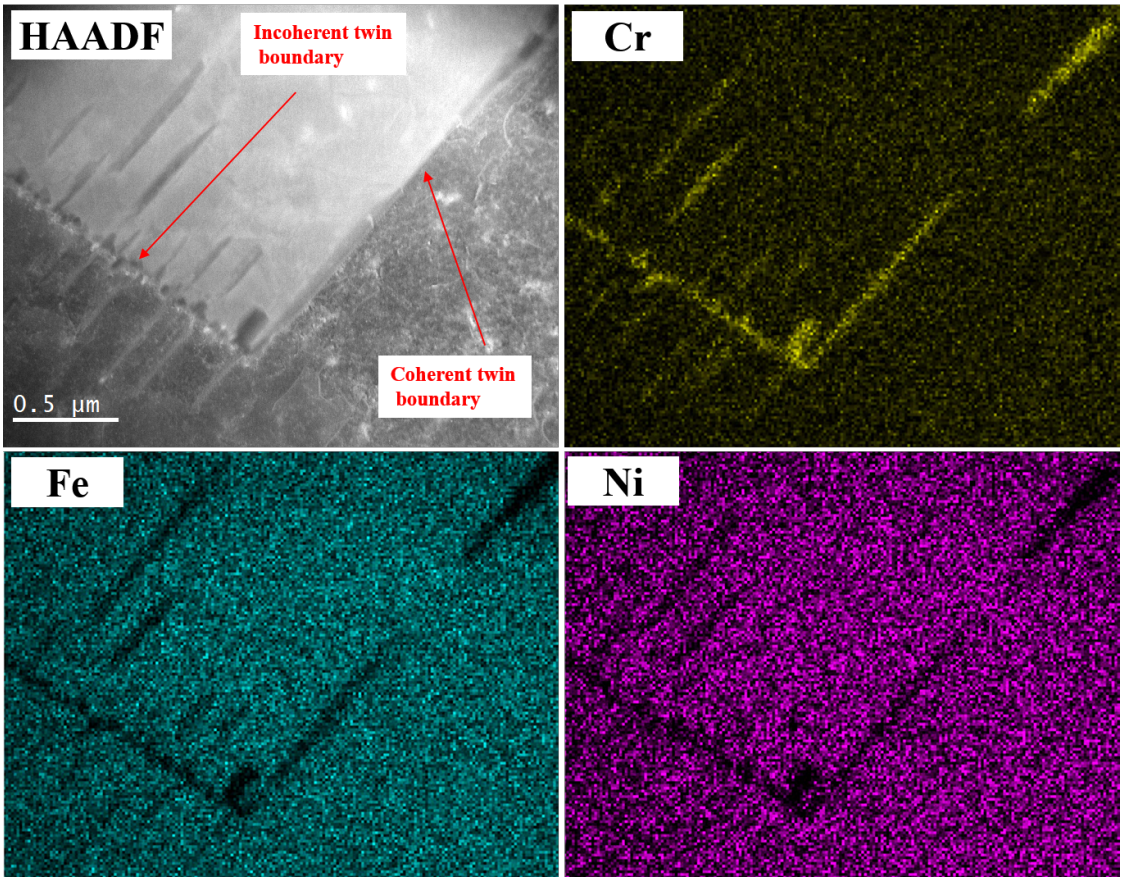

Figure 4.17: EDS element mapping results of the twin boundary in Alloy 709 aged at 750°C for 300h (A709-750C300h). Cr was segregated on the incoherent twin boundary and the coherent twin boundary. Carbon mapping was not shown because of poor sensitivity.

4.5.4 3-D Image of Precipitates near Twin Boundaries

The plan-view and cross-sectional-view images of the twin boundaries in Figs. 4.18 clearly showed the lamella-like structure of the $M_{23}C_6$ precipitates. These precipitates on the twin boundaries have been wrongly described as the needle-like or the bar-like structures in many researches [67–70]. Contrary to this, the observation confirmed that the growth is limited not along the specific direction but on the specific habit plane. Given that the lamella-shaped $M_{23}C_6$ precipitates were located parallel to the twin boundary, the habit plane was thought to be one of twinning planes.

To figure out the morphologies of the lamella-shaped $M_{23}C_6$ on the habit plane, equally spaced cross-sectional images were obtained using the Helios 600i FIB instrument as shown in Figs. 4.19. The specimen was tilted so that the twinning plane was perpendicular to the SEM viewing direction (The twinning plane was approximately parallel to the screen). These images obviously provided direct information on the structure of the lamella-shaped $M_{23}C_6$ on the twin boundaries. The spacing between the images was 10 nm; therefore, it could be estimated that the depth of lamella-shaped $M_{23}C_6$ was about 40 - 50 nm in consistency with the width in the 2-D TEM images. Figs. 4.19(a) showed the lamella-shaped $M_{23}C_6$ was rooted in the twin boundary; the length of the precipitate was approximately 300 nm as shown in Figs. 4.19(d). The shape of precipitate looked like an elongated circle and the length was about 300 nm, which was much longer than $M_{23}C_6$ precipitates in the HAGBs.

In Fig. 4.19 (d), the lamella-shaped $M_{23}C_6$ was disconnected to the twin boundary though it was connected from the twin boundary in Fig. 4.19 (a). The discontinuity of the lamella-shaped $M_{23}C_6$ have been frequently noted in other researches because the cross-section of the specimen was not perfectly parallel to the habit plane. These morphologies misled the interpretation of the microstructure of the lamella-

shaped $M_{23}C_6$ in previous studies [46, 71, 72]. They thought the lamella-shaped $M_{23}C_6$ precipitates were formed on the dislocations at a distance from the twin boundary. Beckitt and Clark explained that the stress due to volume changes of $M_{23}C_6$ guide the growth of $M_{23}C_6$ out from the twin boundary [71]. According to Singhal and Martin, the precipitate was likely to induce the repulsion of the Shockley partial dislocation and then this would lead the incomplete precipitation inside the precipitates that was observed as a break [72]. Sasmal suggested that the higher elastic modulus along <1 1 1> might drive the growth parallel to the coherent twin boundary after the precipitates are formed on the dislocations [46]. The SEM results here showed the discontinuity between the precipitate and the twin boundary was because the precipitate was located at a small angle off the surface. Therefore, the FIB removed the twin boundary and the upper part of the precipitate after taking Fig. 4.19 (b). Therefore, the discontinuity in SEM and TEM results was due that the sectioning of the specimen was not perfectly parallel to the habit plane.

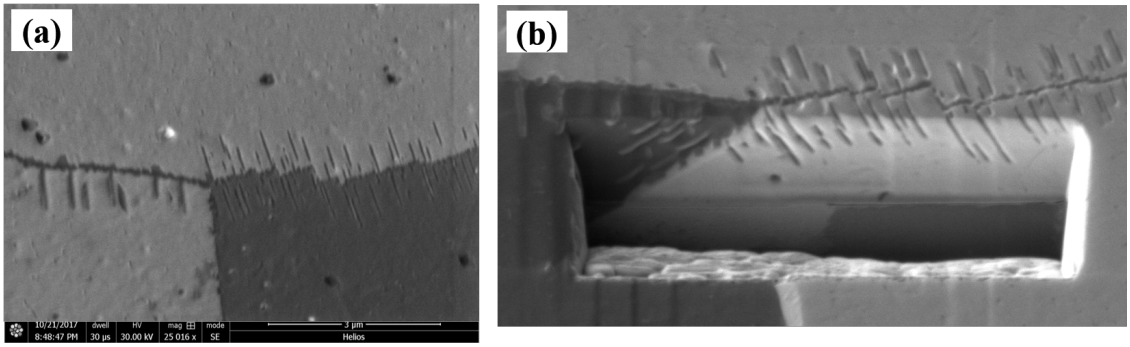

Figure 4.18: (a) Plan-view image of lamella-shaped $M_{23}C_6$ precipitates near the twin boundary. (b) 45° view cross-sectional image of (a). $8 \times 3 \times 8$um trench was cut to show the cross-section.

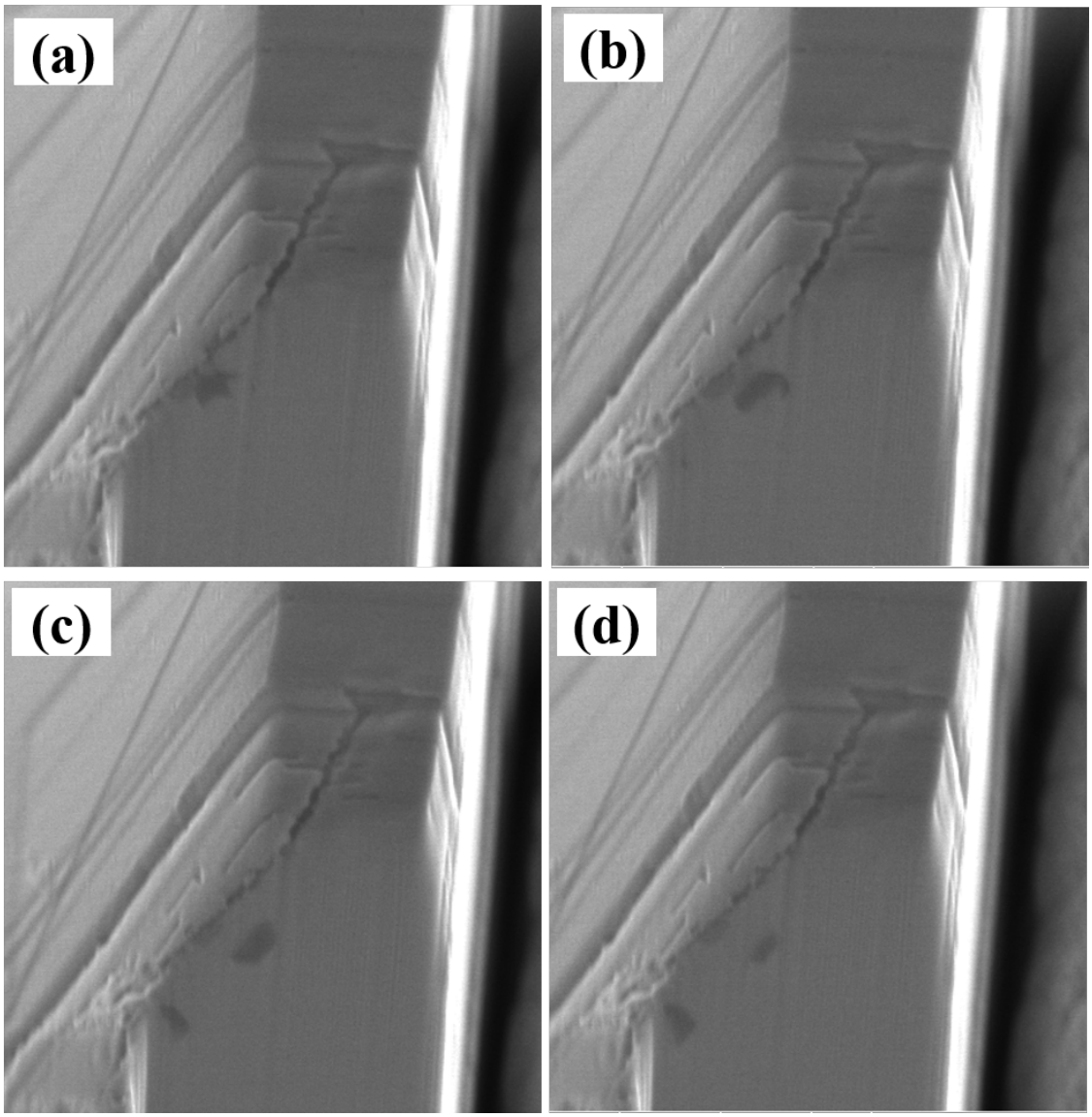

Figure 4.19: Equally spaced cross-sectional images of lamella-shaped $M_{23}C_6$ in the twin boundary. The spacing between images was approximately 10nm.

4.6 Microstructure of Intergranular $M_{23}C_6$ Precipitates

Figs. 4.20 and 4.21 shows the schematic of the microstructure of the intergranular $M_{23}C_6$ precipitates on HAGBs and the lamella-shaped $M_{23}C_6$ on twin boundaries, respectively. Both of them grow in a cube-cube relationship with the neighboring austenite grain, $[001]_\gamma \| [001]_{M_{23}C_6}$ and $[110]_\gamma \| [110]_{M_{23}C_6}$, in a lattice correspondence of $3 \cdot a_{M_{23}C_6} \sim a_{\gamma\text{-Fe}}$. The intergranular $M_{23}C_6$ precipitates share relatively flat coherent interfaces either of neighboring grains, the parent grain. The other interface is rounded outward and incoherent. The intergranular $M_{23}C_6$ precipitates are rooted in the parent grain and grow toward the incoherent grain. The growth is much faster alongside the GBs so the intergranular precipitates exhibit the elongated shape alongside the GB.

In case of the lamella-shaped $M_{23}C_6$ on the twin boundaries, their crystal correlation with the neighboring matrix was analogous to that of intergranular $M_{23}C_6$ precipitates on the HAGBs. The lamella-shaped $M_{23}C_6$ precipitates are rooted in one of the twinning matrices, sharing the coherent interface with it. They have a habit plane and grow towards the opposite side that is the twinning matrix of the parent matrix. The growing direction of the lamella-shaped $M_{23}C_6$ rooted in the other matrix is opposite. Considering the shape of the precipitate, it was estimated that the growth of the lamella-shaped $M_{23}C_6$ results from the diffusion from the matrix as in other intergranular $M_{23}C_6$ precipitates on the HAGBs. The fine equiaxed $M_{23}C_6$ are also formed on the twin boundaries.

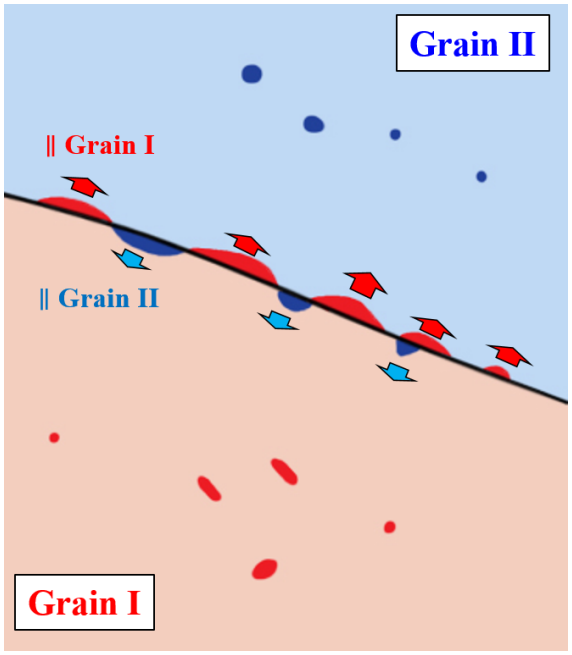

Figure 4.20: Schematic of the microstructure of $M_{23}C_6$ precipitates on HAGBs. Grains in same color represent the identical crystallographic orientation.

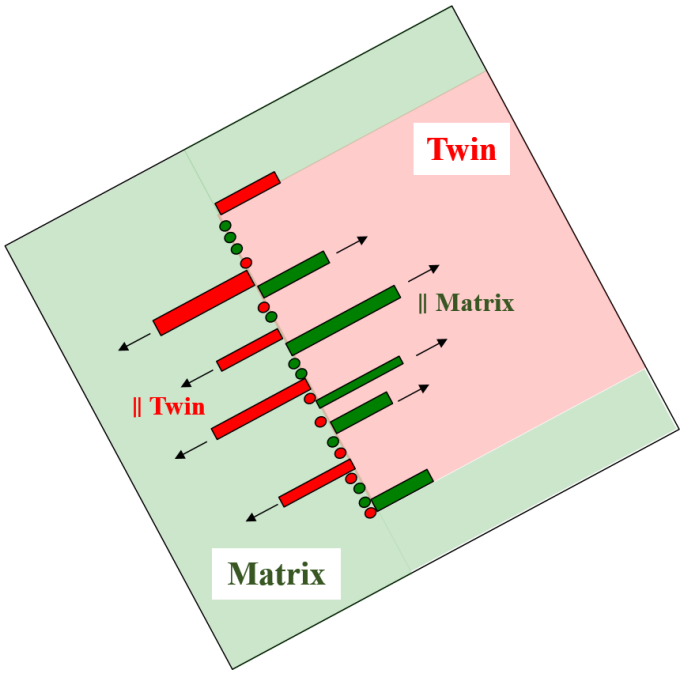

Figure 4.21: Schematic of the microstructure of lamella-shaped $M_{23}C_6$ precipitates on twin boundaries. Grains in same color represent the identical crystallographic orientation.

CHAPTER 5

EFFECT OF INTERGRANULAR $M_{23}C_6$ PRECIPITATES ON MECHANICAL PROPERTIES OF ALLOY 709

The third objective of this study is to investigate the impact of the $M_{23}C_6$ precipitation on the mechanical response of Alloy 709 under deformation. As discussed in Chapter 3 and 4, the intergranular $M_{23}C_6$ precipitates were the dominant precipitate phase in the aged Alloy 709 specimens. There will be significant precipitation on the GBs during high temperature operation in the advanced reactors even if the pristine Alloy 709 is used. Therefore, in-situ XRD experiments would provide valuable information on how the intergranular $M_{23}C_6$ precipitates correlate with the microstructural evolution of the material. Dogbone specimens cut from the as-received and the aged Alloy 709 sample were uniaxially strained while synchrotron diffractions were recorded. One as-received, two aged specimens were chosen to figure out the roles of the $M_{23}C_6$ precipitates for strengthening the material. The 2D ring diffraction patterns were analyzed to calculate lattice strains, applied stress, Young's modulus, and Poisson's ratio. The mechanical behaviors under deformation are discussed in terms of the correlation of the intergranular $M_{23}C_6$ precipitates and the austenite matrix. The morphological changes near the intergranular $M_{23}C_6$ precipitates in tensile-deformed specimens are also compared to those of un-deformed specimens using microscopes.

5.1 Experimental Methods

5.1.1 Sample Preparation

After aging of the Alloy 709 samples, an electrical discharge machining (EDM) was used to machine dogbone specimens at the MechSE Machine Shop in the University of Illinois at Urbana and Champaign. Fig. 5.1 shows a drawing of the dogbone specimens; the thickness and the width of the narrow section were 12mm and 0.75 mm, respectively. Three aging conditions were chosen to test Alloy 709 with different $M_{23}C_6$ volume fractions: as-received (A709-AsR), 750°C-10h (A709-750C10h), and 750°C-3000h (A709-750C300h). As shown in Fig. 3.11, the volume fractions of A709-AsR, A709-750C10h, and A709-750C300h were 0, 0.09, 0.15 wt%, respectively.

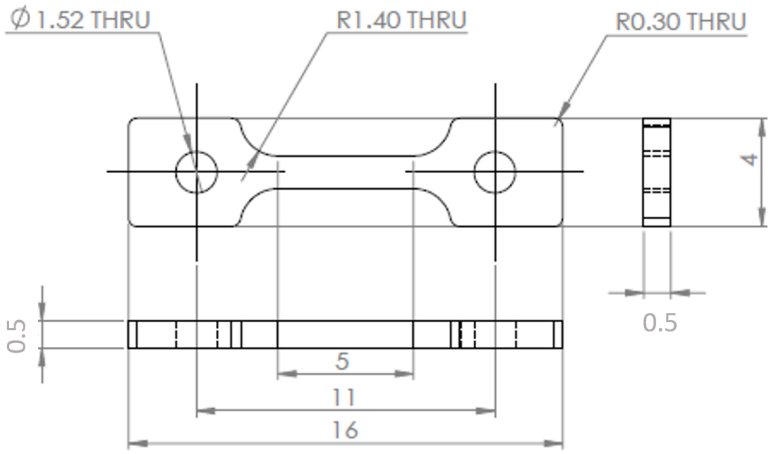

Figure 5.1: Dimensions of the dogbone tensile specimens.

5.1.2 In-situ Synchrotron XRD Measurement during Tensile Test

The in-situ synchrotron diffraction profiles measurements during tensile-straining were carried out at room temperature and atmospheric in the APS synchrotron 1-ID

beam line in Argonne national lab. The experimental setup and beam conditions were identical to that of the ex-situ measurements in Chapter 3. The picture of the tensile specimen holder and the detectors are shown in Fig. 5.2. A MTS closed-loop servo-hydraulic tensile load frame (Model 858) was attached to the beam line and the tensile holder was mounted on the load frame to secure the dogbone tensile specimens. A pre-loading with a small load of approximately 20N was applied to the specimens to remove slack. The specimens were strained vertically at a constant holder grip movement speed of 5×10^{-5}mm/s (corresponding strain rate of 10^{-5}/s) in the elastic regime. An incident beam with a size of 100×100 μm horizontally scanned the specimens with a step size of 10 μm. 50 scans were averaged to obtain a diffraction profile at each data point. It took about 1 - 2 h to pass the elastic regime and then the grip movement speed increased to 5×10^{-4}mm/s (corresponding strain rate of 10^{-4}/s) to reduce test time (3-5 h depending on the total strain). The length of an exposed region (between the holder grips) of the specimen was set as the initial length of the specimen, 5mm. The increasing distance between the holder grips during the test was measured to calculate the engineering strain.

2-D diffraction rings at each data point were analyzed to measure the lattice strain change for the austenite and the precipitate. The diffraction rings recorded on the detectors were circular without uniaxial load. When the specimen was strained along the loading direction, the strain of the specimen was positive in the axial direction and negative in the transverse direction of the loading direction. Because 2θ and d-spacing were in inverse relation, the diffraction rings became ellipsoidal rings that the long axis was oriented in the transverse direction. Fig 5.3 shows an array of each detector: GE 1 (η=270°) and GE 3 (η=90°) detectors in the axial direction; GE 2(η=180°) and GE 4 (η=360°) detectors in the transverse direction. The diffraction rings were integrated over a 20° on each direction. In particular, the rings with an azimuthal angle of 80-100° and 260-280° were integrated to obtain a 1-D diffraction spectrum in the axial direction; 170-190° and 350-10° in the

transverse direction. Each 1-D diffraction spectrum was fitted with a pseudo-Voigt function using the GSAS 2 software to find the peak center(θ_0), intensity, and width. Changes in d-spacing represents lattice strain development of grains orientated with {h k l} lattice plane perpendicular to the loading direction. The initial d-spacing of {h k l} reflection, d_0^{hkl}, and the d-spacing of the {h k l} reflection, d^{hkl}, were calculated from Bragg's law (Eq.2.11):

$$d_0^{hkl} = \frac{\lambda}{\theta_0^{hkl}} \; and \; d^{hkl} = \frac{\lambda}{\theta^{hkl}} \tag{5.1}$$

where θ_0 is the center of the fitted {h k l} reflection in the 1-D diffraction spectrum of the specimen without external load. The strain for each {h k l} reflection could be calculated using the following equation:

$$\epsilon_{hkl} = \frac{d^{hkl} - d_0^{hkl}}{d_0^{hkl}} \tag{5.2}$$

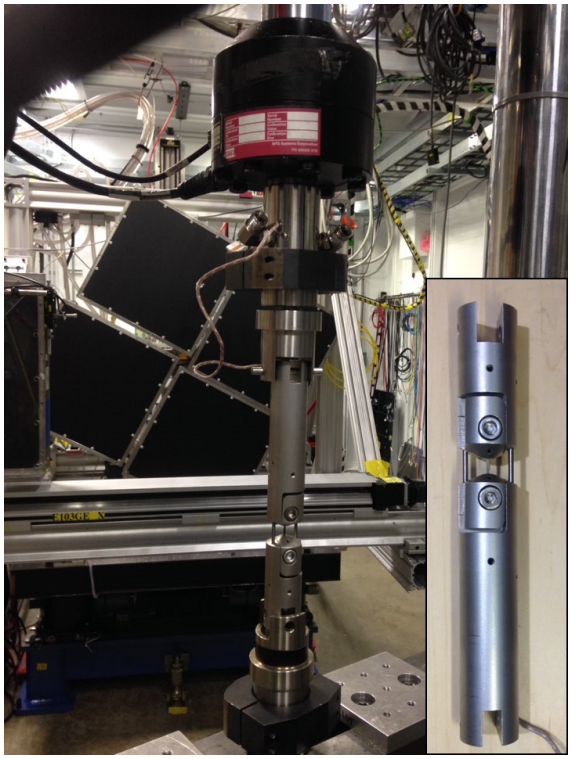

Figure 5.2: The MTS tensile tester and the grip holder at the APS synchrotron 1-ID beam line. The 4 GE detectors were seen behind the holder. An inset showed an enlarged image of the grip holder and a loaded Alloy 709 specimen.

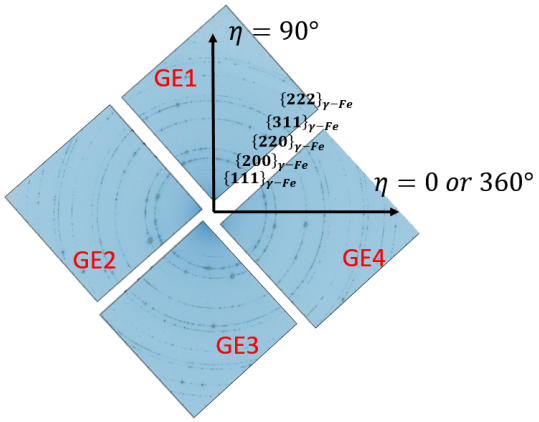

Figure 5.3: Diffraction rings recorded on the 4 GE detectors. 2D-diffraction rings associated with the austenite are labelled.

5.2 Mechanical Properties of Alloy 709

Fig. 5.4 shows the engineering stress as a function of engineering strain curves for the as-received Alloy 709 (A709-AsR), the Alloy 709 aged at 750°C for 300h (A709-750C300h), the Alloy 709 aged at 750°C for 3000h (A709-750C3000h. The mechanical properties of each specimen are listed in Table 5.1. The serrations in the early stage of the as-received tensile curve were caused by the force release. The synchrotron X-ray beam line suddenly stopped for 1 h during the test, so the straining was paused and then continued after the beam was back to normal. The data during was removed; the curve excluding the break was analogous to the curves of the as-received Alloy 709 that was measured at the other hydraulic tensile test machine [73]. The aged Alloy 709 exhibited shorter elongation and higher ultimate tensile strength (UTS) than the as-received one in accordance with the typical behaviors of the aged alloys due to precipitation hardening. The elongation of the as-received, the 750°C-300h, and the 750°C-3000h Alloy 709 specimens were 0.57, 0.68, and 0.72, respectively. This was in relation to the volume fraction increase, which was discussed in Chapter 4, indicating the ductility of aged Alloy 709 was strongly correlated with the $M_{23}C_6$ precipitates. The Yield strength and the UTS increased with increasing volume fraction of the $M_{23}C_6$ precipitates; however, there was no noticeable change between the 10 h and 300 h specimens. The Young's modulus increased by 30 % and the UTS doubled in the aged specimens, confirming $M_{23}C_6$ contributed to strengthening of the aged Alloy 709.

Table 5.1: Mechanical properties of as-received Alloy 709 (A709-AsR), Alloy 709 aged at 750°C for 300h (A709-750C300h), Alloy 709 aged at 750°C for 3000h (A709-750C3000h).

Samples	Young's modulus [GPa]	Yield strength [MPa]	UTS [MPa]	Elongation
as-received	101	178	514	0.57
750°C-10h	128	305	688	0.68
750°C-300h	137	345	671	0.72

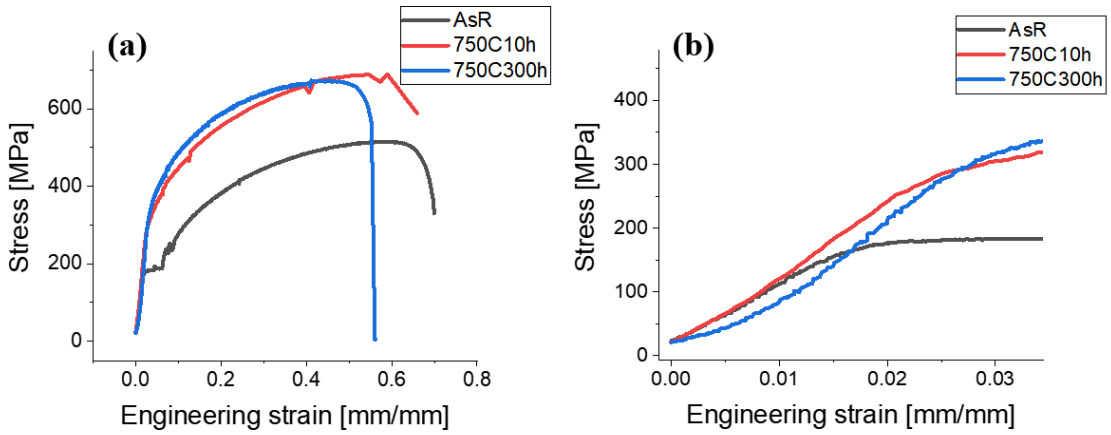

Figure 5.4: (a) Engineering stress curves as a function of engineering strain and (b) zoomed-in curves in the elastic regime for as-received Alloy 709 (A709-AsR), Alloy 709 aged at 750°C for 300h (A709-750C300h), Alloy 709 aged at 750°C for 3000h (A709-750C3000h). The force release during the unexpected stoppage of the beam line caused serrations in the early plastic deformation region of the tensile curve for the as-received one. Mechanical properties were not affected by the serration in comparison with the tensile tests of identical sample set that was performed in the other hydraulic tensile load frame.

5.3 Lattice Strain Evolution of Austenite Matrix in Alloy 709

Fig. 5.5 shows the lattice strain curves *versus* engineering stress of the austenite for the as-received (A709-AsR), the 750°C-300h (A709-750C10h), and the 750°C-300h (A709-750C300h) Alloy 709 specimens. Like the engineering stress - engineering strain curves in Fig. 5.4, the engineering stress - the lattice strain curve was linear over the strain range of 0-2 $\times$ 10^{-3}. As stress increased, the curves deviated from the linearity in all specimens; the starting points of non-linearity were roughly 180, 300, and 350 [MPa] in the as-received, the 750°C-10h, and the 750°C-300h specimen, respectively. The points were consistent with the transition point from

the elastic regime to the plastic regime, confirming that the non-linearity of the lattice strain evolution also started from the onset of the plastic regime.

The lattice evolution was distinct among planes (A detailed discussion about this can be found in the next chapter). Grains orientated with $\{2\ 0\ 0\}_{\gamma\text{-Fe}}$ were the most strained for all aging conditions. The anisotropic behavior was attributed to the slip system in fcc materials. When the tensile axis is aligned to a $\langle 2\ 0\ 0\rangle$ direction, four slip directions in the cubic system are distributed symmetrically around $\langle 2\ 0\ 0\rangle$ so that the slips are much favorable along the $\langle 2\ 0\ 0\rangle$ direction [74]. At the given engineering stress of 400 MPa, the strain in the as-received, the 750°C-10h, the 750°C-300h specimen was 4.5×10^{-3}, 3.8×10^{-3}, and 3.8×10^{-3}, respectively. Considering that the strain is proportional to the applied load, the lower strain of the austenite indicated that some portion of the load on the austenite was taken over to the precipitates, confirming the strengthening effect of the $M_{23}C_6$ precipitates. The other noticeable point was that the maximum strain for $\{2\ 0\ 0\}_{\gamma\text{-Fe}}$ did not vary with the aging conditions. $\{2\ 0\ 0\}_{\gamma\text{-Fe}}$ was strained up to approximately 8.4×10^{-3} until fracture, suggesting the austenite matrix of Alloy 709 could not withstand the lattice strain more than 8.4×10^{-3}.

5.4 Anisotropy of Austenite Matrix in Alloy 709

As reviewed in Chapter 2.3.3, the austenite matrix exhibits an elastically anisotropy under uniaxial loading and its Young's modulus of each {h k l} plane could be predicted using Reuss's model. S_{11}, S_{12}, S_{44} of the austenite stainless steel are 0.757,-0.18,and 0.86, respectively; Eq.2.7 gave the calculated elastic modulus for each plane. $\{h\ k\ l\}_{\gamma\text{-Fe}}$ specific elastic modulus are E_{111} = 220 GPa, E_{200} = 132 GPa, E_{220} = 188 GPa, and E_{311} = 163 GPa.

Fig. 5.6 shows E_{hkl} as a function of anisotropy factor, A_{hkl}(calculated from Eq.2.10). The predicted value by Reuss's model and the measured value from Fig. 5.4 are

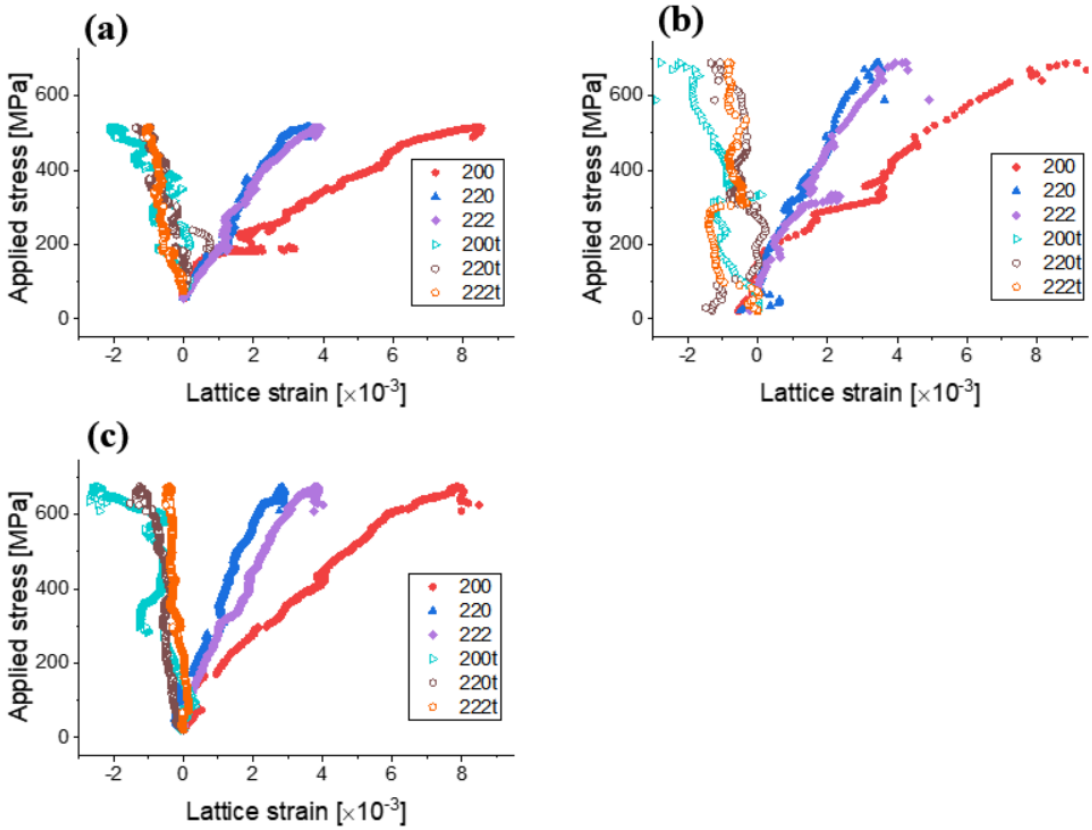

Figure 5.5: Lattice evolution of the austenite matrix along the loading direction and the transverse direction for (a) as-received Alloy 709 (A709-AsR), (b) Alloy 709 aged at 750°C for 10h (A709-750C10h), and (c) Alloy 709 aged at 750°C for 300h (A709-750C300h). The open symbols represent the transverse direction.

plotted. The data points in the elastic regime were fitted using the linear least squares fitting to calculate the slope (stiffness), E_{hkl}. E_{hkl} was in proportional relation to A_{hkl} for all aging conditions as predicted by Reuss' model. There was no obvious trend change between the as-received one and the aged ones, leading to an estimate that the presence of $M_{23}C_6$ precipitates did not impact the anisotropy of the austenite in the elastic regime.

The linear relation between the macrostress and the lattice strain started to vary from the onset of the plastic regime as shown in Fig. 5.7. There was no obvious non-linearity for $\{1\ 1\ 1\}_{\gamma\text{-Fe}}$. The linearity for $\{1\ 1\ 1\}_{\gamma\text{-Fe}}$ over the full range of strain was reported in previous studies on other stainless steels and nickel-base alloys with a fcc structure [75–78]. Grains orientated with brittle $\{1\ 1\ 1\}_{\gamma\text{-Fe}}$, which elastic modulus was the highest, did not yield over the entire strain range. The non-linearity of the lattice strain evolution was observed in all reflections except for $\{1\ 1\ 1\}_{\gamma\text{-Fe}}$. The slope of $\{2\ 0\ 0\}_{\gamma\text{-Fe}}$ in the plastic regime was the lowest among the planes as well as in the elastic regime, indicating grains orientated with $\{2\ 0\ 0\}_{\gamma\text{-Fe}}$ are the softest both in the elastic and plastic regime. The lattice strain for $\{2\ 0\ 0\}_{\gamma\text{-Fe}}$ was further strained than the extrapolated linearity from the onset of the plastic regime for all conditions, while in the curve of $\{2\ 2\ 0\}_{\gamma\text{-Fe}}$ a negative deviation from the extrapolated linearity was observed for 750°C-300h aging condition. The contrast behavior of $\{2\ 0\ 0\}_{\gamma\text{-Fe}}$ and $\{2\ 2\ 0\}_{\gamma\text{-Fe}}$ was due to the microstress on the austenite grains [49]. As the macrostress increased, the $\{2\ 0\ 0\}_{\gamma\text{-Fe}}$ orientated grains yielded first and the further lattice microstrain was induced along the $\{2\ 0\ 0\}_{\gamma\text{-Fe}}$ orientated grains in the plastic regime. The tensile intergranular microstrain of $\{2\ 0\ 0\}_{\gamma\text{-Fe}}$ orientated grains resulted in the compressive microstress on $\{2\ 0\ 0\}_{\gamma\text{-Fe}}$ orientated grains. The negative microstrain due to compressive microstress was observed as the negative deviation from the extrapolated linearity, although the net increase in lattice strain was positive over the entire strain.

The presence of $M_{23}C_6$ appeared to influence the anisotropy of the austenite.

The slope of $\{2\ 0\ 0\}_{\gamma\text{-Fe}}$ was approximately 60% higher in the as-received specimen than in the aged ones, while the discrepancy was relatively small in other planes. The precipitates inside the matrix were known to induce multiple slips instead of a single slip and then decrease the anisotropy [79, 80]. Therefore, the preferential strain for $\{2\ 0\ 0\}_{\gamma\text{-Fe}}$ was very likely limited by the $M_{23}C_6$ precipitates. Considering that $\{2\ 0\ 0\}_{\gamma\text{-Fe}}$ orientated grains determine the yield of the austenite matrix during lattice strain development under uniaxial loading, it could be concluded that the strengthening in aged Alloy 709 resulted from the preferential hardening of $\{2\ 0\ 0\}_{\gamma\text{-Fe}}$ orientated grains by the intergranular $M_{23}C_6$ precipitates.

The anisotropy was also observed along the transverse direction in all specimens as shown in Fig. 5.5. $\{2\ 0\ 0\}_{\gamma\text{-Fe}}$ compressed most. The Poisson's ratio of $\{2\ 0\ 0\}_{\gamma\text{-Fe}}$ was calculated using the ratio of the lattice strain in the transverse direction to that in the axial direction represents: 0.293, 0.281, and 0.291 for the as-received, the 750°C-10h, and the 750°C-300h specimens, respectively. The trend did not show any obvious correlation with the aging condition.

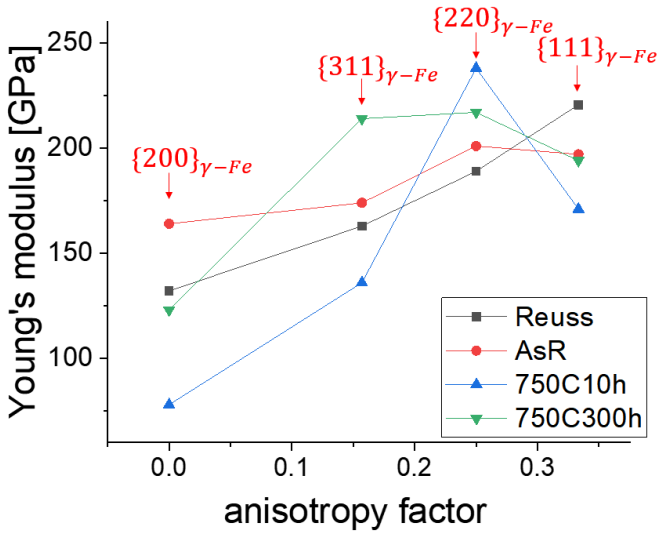

Figure 5.6: Young's modulus curves as a function of anisotropic factor, A_{hkl}, for as-received and aged Alloy 709. Predicted Young's moduli by Reuss' model were plotted together with the experimental results.

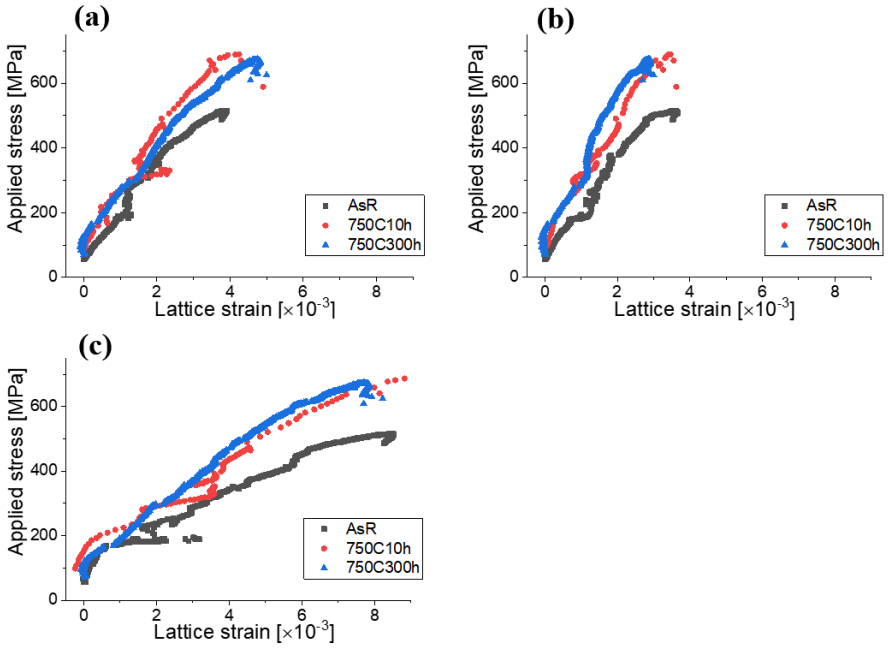

Figure 5.7: Lattice evolution of (a) $\{2\ 2\ 2\}_{\gamma\text{-Fe}}$, (b) $\{2\ 2\ 0\}_{\gamma\text{-Fe}}$, and (c) $\{2\ 0\ 0\}_{\gamma\text{-Fe}}$ for as-received and aged Alloy 709.

5.5 Behavior of Precipitates in Alloy 709 under Stress

Fig. 5.8 exhibits the lattice strain evolution of the NbN and the $M_{23}C_6$ precipitates. The lattice strain of the NbN precipitates increased up to 7.9×10^{-3} with increasing strain in the as-received specimen. The maximum lattice strain was considerably reduced in the aged samples, increasing to 5.2×10^{-3} and 4.8×10^{-3} in the 750°C-10h specimen and the 750°C-300h specimen, respectively. The maximum load on the NbN phase were calculated using Eq.3.1: 2.8 GPa, 1.84 GPa, and 1.7 GPa for the as-received, the 750°C-10h, and the 750°C-300h specimen, respectively. The lower load for the aging samples confirmed the load partitioning of the $M_{23}C_6$ precipitates as also evidenced by the lower lattice strain of the austenite for the aged specimen. For the $M_{23}C_6$ precipitates, the trend in lattice strain increase was similar, reaching 8.6×10^{-3} and 8×10^{-3} for the 750°C-10h specimen and the 750°C-300h specimen, respectively. The maximum load of $M_{23}C_6$ was 20% higher

for the 750°C-10h specimen compared to the 750°C-300h specimen, 2.5 GPa and 2.9 GPa, respectively. When the volume fraction of each phase was taken into account, the loading partitioning fraction of $M_{23}C_6$ could be obtained:

$$f_{M_{23}C_6} = \frac{V_{M_{23}C_6} \cdot \sigma_{M_{23}C_6}}{V_{M_{23}C_6} \cdot \sigma_{M_{23}C_6} + V_{NbN} \cdot \sigma_{NbN}} \tag{5.3}$$

where V is the volume fraction for each phase. $f_{M_{23}C_6}$ was 0, 0.23, and 0.63 for as-received (0.15 wt% of NbN), 750°C-10h (0.14 wt% of NbN and 0.03 wt% of $M_{23}C_6$), and 750°C-300h (0.15 wt% of NbN and 0.18 wt% of $M_{23}C_6$), respectively. Therefore, it could be confirmed that both the $M_{23}C_6$ and the NbN contributed to strengthening the material. $f_{M_{23}C_6}$ appeared to similar to the volume fraction ratio of $M_{23}C_6$ to NbN, indicating the load partitioning of each precipitate phase was in strong relation to its volume fraction.

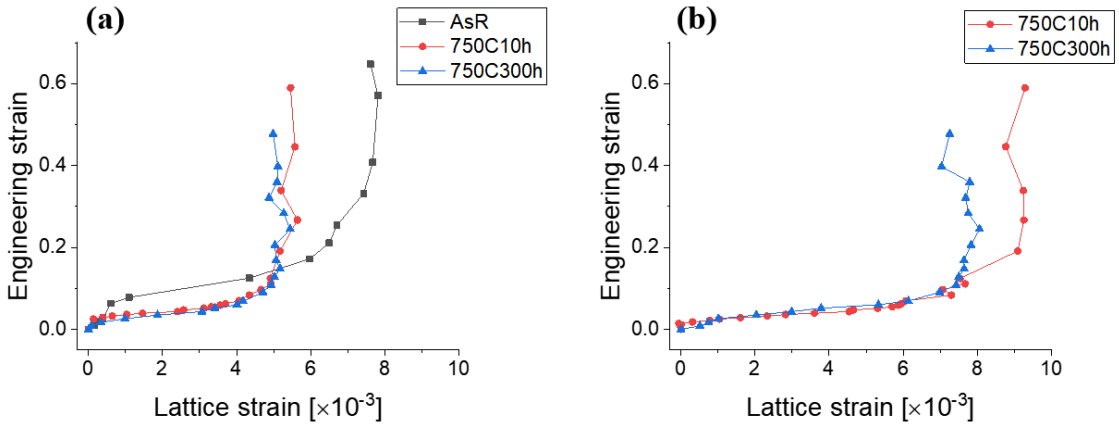

Figure 5.8: Lattice strain evolution of (a) NbN and (b) $M_{23}C_6$ in as-received, 750°C-10h, and 750°C-300h Alloy 709. $\{4\ 2\ 0\}_{M_{23}C_6}$ and $\{2\ 0\ 0\}_{NbN}$ was chosen because it was the strongest peak. Other weak peaks were hard to be differentiated from background noise since the intensity was too low.

In contrast to the behavior of the austenite, it was noted that the increase of the lattice strain for both precipitate phases was saturated in the plastic regime. This indicated that the NbN and the $M_{23}C_6$ precipitates could not withstand significant

stress and subsequently started to fail. The failure of precipitate was observed in the SEM results as well. Fig. 5.9 exhibit the morphologies near HAGBs and twin boundaries of the as-received and 750°C-300h Alloy 709 after fracture. The images were taken from the representative region without severe deformation, which was at 5 mm distance from a necking point. The images clearly showed how the austenite matrix reacts to the failure of the precipitates during deformation. In the as-received Alloy 709, a few microcracks were observed next to intragranular precipitates and no microcrack was found on the GBs. In contrast to this, the GBs decorated with the intergranular $M_{23}C_6$ precipitates in aged Alloy 709 showed different behaviors. A large number of microcracks were observed along the HAGBs, indicating that the formation of the microcracks was mostly due to the delamination of the interphase interface or the fracture inside the intergranular precipitates on the HAGBs. Therefore, the results led to the conclusion that the microstructural failure near the precipitates limit the load partitioning effect of the precipitates in the aged material.

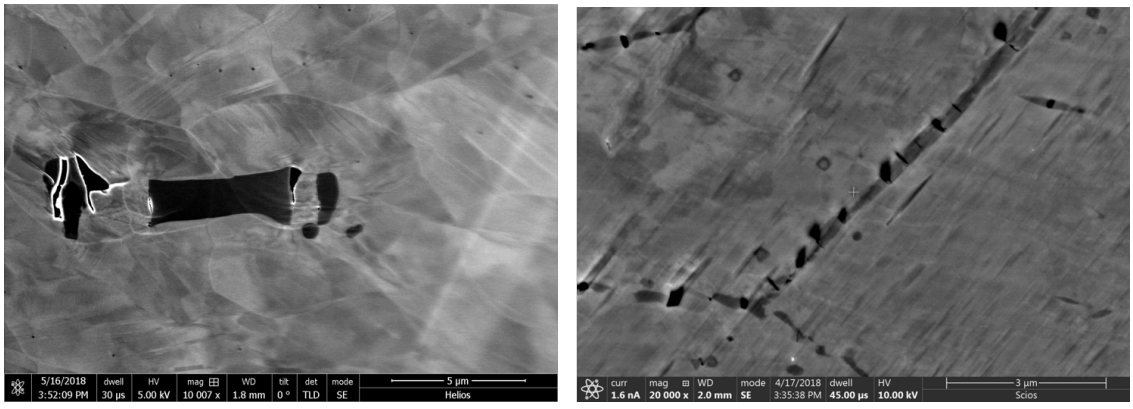

Figure 5.9: Microcracks in the Alloy 709 specimen after failure: (a) as-received Alloy 709 and (b) Alloy 709 aged at 750°C for 3000h. Black features represented cracks.

CHAPTER 6

CONCLUSIONS

Alloy 709 specimens aged at 550, 650 and 750℃ for 1 to 3000 h were investigated using various analytical tools such as SEM, EBSD, EDS, TEM, STEM, and synchrotron diffraction analysis. The morphological, microstructural, and mechanical properties of the $M_{23}C_6$ precipitates in the aged Alloy 709 were successfully studied.

First, the morphologies of precipitates were varied by the characteristics of the GBs and the precipitation time threshold in Alloy 709 were different from other Fe-20Cr-25Ni austenitic alloys. The findings are summarized as follows:

(i) $M_{23}C_6$ was the predominant precipitate phase of the aged Alloy 709.

(ii) No $M_{23}C_6$ was formed under aging at 550°C; intense precipitation of $M_{23}C_6$ precipitates was found on grain boundaries after aging at 650 and 750°C.

(iii) Elongated $M_{23}C_6$ precipitates and lamella-shaped $M_{23}C_6$ precipitates were formed on HAGBs and twin boundaries, respectively.

(iv) The precipitation time threshold of the intergranular $M_{23}C_6$ on the HAGBs was shorter than that of the lamella-shaped $M_{23}C_6$ precipitates.

(v) The frequency and the volume fraction of the $M_{23}C_6$ increased after the precipitation threshold and did not reach saturation for aging conditions in this study.

These results confirmed the Time-Temperature-Precipitation diagram of the $M_{23}C_6$ precipitate phase, which was different from the known Time-Temperature-Precipitation diagram of other Fe-20Cr-25Ni austenitic steels. The formation of intergranular $M_{23}C_6$ precipitates caused compressive stress on the austenite matrix and tensile stress on the $M_{23}C_6$ precipitates, which became higher with increasing aging time

because of the volumetric expansion of the intergranular $M_{23}C_6$ precipitates.

Second, the intergranular $M_{23}C_6$ precipitates on the HAGBs and the lamella-shaped $M_{23}C_6$ precipitates on the twin boundaries crystallographically correlated with the neighboring austenite matrix. The $M_{23}C_6$ precipitates formed as an fcc structure (Fm-3m) in a cube - cube relationship with the austenite matrix, $[001]_{\gamma\text{-Fe}} \| [001]_{M_{23}C_6}$ and $[110]_{\gamma\text{-Fe}} \| [110]_{M_{23}C_6}$. The observation of an identical crystal orientation between the intergranular $M_{23}C_6$ and the neighboring austenite grain indicated that the intergranular $M_{23}C_6$ on the HAGBs were rooted in either of the neighboring grains, sharing a coherent interface with the austenite matrix. The intergranular $M_{23}C_6$ grew toward the opposite side of the parent grain while maintaining a lattice correspondence with the parent matrix, $3 \cdot a_{M_{23}C_6} \approx a_{\gamma\text{-Fe}}$. The equally spaced cross-sectional images confirmed that the lamella-shaped $M_{23}C_6$ precipitates on the twin boundaries were also rooted in either of the neighboring grains, contradicting the controversial explanation of the discontinuity of the lamella-shaped $M_{23}C_6$ from the twin boundaries. Compared to the intergranular $M_{23}C_6$ on the HAGBs, the growth was confined on the habit plane, one of the twinning planes. The intergranular $M_{23}C_6$ precipitates that was rooted in the same grain had an identical crystal orientation.

Third, the presence of the $M_{23}C_6$ strengthened the material and also resulted in morphological changes near the grain boundaries. The austenite anisotropically responded to applied stress both in the elastic regime and the plastic regime. An obvious correlation between the precipitate and the anisotropic behavior of the austenite was not observed. Grains orientated with $\{2\ 0\ 0\}_{\gamma\text{-Fe}}$ that yielded first was strained most, governing the yield and the failure of the austenite matrix. The stiffness of $\{2\ 0\ 0\}_{\gamma\text{-Fe}}$ in the aged Alloy 709 substantially increased, confirming that $M_{23}C_6$ hardened the material by reducing the microstrain of $\{2\ 0\ 0\}_{\gamma\text{-Fe}}$ orientated grains. The tensile microstrain of $\{2\ 0\ 0\}_{\gamma\text{-Fe}}$ orientated grains induced compressive stress on $\{2\ 2\ 0\}_{\gamma\text{-Fe}}$ orientated grains, while grains orientated with $\{1\ 1\ 1\}_{\gamma\text{-Fe}}$,

which has the highest elastic modulus, did not yield over the entire strain range. The presence of $M_{23}C_6$ precipitates substantially increased the strength of the Alloy 709 while taking over the load. The small volume fraction of $M_{23}C_6$ was effective in strengthening and $M_{23}C_6$ became the main strengthening phase with the increase in volume fraction. The mechanical failure of the precipitates, which were confirmed by the formation of microcracks near the precipitates, limited further increase of the load partitioning by the precipitates.

CHAPTER 7

FUTURE WORK

This section will describe the proposed direction of future works based on the limits of this study. Although this study revealed many of the microstructural properties of the intergranular $M_{23}C_6$ in the aged Alloy 709 and their impact on the mechanical properties of the material. More experimental tasks could be suggested to provide a comprehensive understanding of the growth behavior and the strengthening mechanism of the $M_{23}C_6$ precipitates in austenitic steels.

7.1 Morphologies of $M_{23}C_6$ in Early Stage of Precipitation

The study of the microstructural evolution of the intergranular $M_{23}C_6$ in the early stage of precipitation in Alloy 709 will provide a complement to this study. In particular, the study will focus on how the $M_{23}C_6$ precipitates nucleate on the dislocations and grow toward the neighboring austenite matrix. The study needs to include the behaviors of intergranular $M_{23}C_6$ on other GB types, such as LAGBs or triple junctions, which were not studied in this research, as well as on HAGBs and twin boundaries.

The proposed work scope involves two elements, specimen preparation and experimental characterization. Alloy 709 samples right before the precipitation threshold will yield information in regard to the nucleation behavior of the intergranular $M_{23}C_6$ precipitates in the early stage of precipitation. The aging conditions can be chosen based on the Time-Temperature-Precipitation diagram of Alloy 709 that

was obtained in this study. The morphologies will be similar to those in Fig. 2.5. Tiny faceted precipitates are expected to be distributed along the GBs. In the specimens subjected under a longer aging process, the intergranular $M_{23}C_6$ precipitates will coarsen and then segregate in a semi-continuous thin layer, revealing the microstructural evolution of intergranular $M_{23}C_6$.

Various techniques are needed to study the crystallographic properties of the intergranular $M_{23}C_6$ precipitates. Considering the lower limit of the area selection of the selected area diffraction aperture (approximately 200nm in most TEMs), electron DPs of each nano-sized crystal in the specimens in the early stage of precipitation could be obtained using the nano aperture election diffraction (NAED) technique. When a small condenser aperture is inserted, a beam-aligning lens can limit the probe size to less than several tens of nanometers and focus a parallel transmitted beam on the front focal plane of the objective lens. The diffracted beam from this nano-sized probe, which is smaller than the grain size, will reveal the crystal information of the nano-sized crystals. The DPs will exhibit coherency with either of the neighboring grains as well. In addition, the dark field imaging technique, which was utilized in this study, will be applicable to the observation of tiny intergranular precipitates in the early stage of precipitation.

7.2 Chemical Analysis of Intergranular $M_{23}C_6$

Chemical information is of considerable interest as well because it will explain the formation mechanism of the intergranular precipitates. Cr diffusion from the austenite matrix is the driving force behind the precipitation and, therefore, the observations of the Cr distribution near the interface of the intergranular $M_{23}C_6$ precipitates will provide a fundamental understanding of the formation of intergranular $M_{23}C_6$. Atom probe tomography (ATP) makes it possible to see if the Cr-depleted zones are located near the intergranular $M_{23}C_6$ precipitates. More-

over, the comparison of the elemental concentrations of the intergranular $M_{23}C_6$ precipitates on the different types of GBs would be informative.

7.3 Dislocation Movement near Intergranular $M_{23}C_6$

More TEM analysis will provide better insight into the strengthening mechanism of the intergranular precipitates. Because the precipitates strengthen the material via impeding the movement of dislocations, the intergranular precipitates act as barriers to the transmission of dislocations from one grain to the next during deformation, causing the dislocation pile-up on intergranular precipitates. The best investigative tool for the movement of dislocations near the GBs is in-situ TEM. The results will be compared to the GBs without precipitates where the tangled dislocation structures are expected to form.

CHAPTER 8

REFERENCES

[1] "World energy outlook 2014," tech. rep., International Energy Agency, Paris, France, 2014.

[2] "IAEA annual report 2016," tech. rep., International Atomic Energy Agency, Vienna, Austria, 2016.

[3] G. Nerac and A. GIF, "A technology roadmap for generation iv nuclear energy systems," in *The US DOE Nuclear Energy Research Advisory Committee and the Generation IV International Forum*, 2002.

[4] K. Murty and I. Charit, "Structural materials for Gen-IV nuclear reactors: Challenges and opportunities," *Journal of Nuclear Materials*, vol. 383, no. 1-2, pp. 189–195, 2008.

[5] S. J. Zinkle and G. Was, "Materials challenges in nuclear energy," *Acta Materialia*, vol. 61, no. 3, pp. 735–758, 2013.

[6] R. W. Moir and E. Teller, "Thorium-fueled underground power plant based on molten salt technology," *Nuclear technology*, vol. 151, no. 3, pp. 334–340, 2005.

[7] R. Accosta, "Studies of metal fire," *Study of Sodium Spray Fires for Sandia National Laboratories*, 2008.

[8] R. Hill, "US status of fast reactor research and technology," *Argonne National Laboratory, Nuclear Engineering Division*, 2012.

[9] K. Natesan and M. Li, "Materials performance in sodium-cooled fast reactors: past, present, and future," in *International conference on fast reactors and related fuel cycles: safe technologies and sustainable scenario. Paris*, 2013.

[10] T.-L. Sham, M. A. Sokolov, and L. Tan, "Creep resistance and fracture toughness of recently-developed optimized Grade 92 and its weldments for advanced fast reactors," tech. rep., Oak Ridge National Lab.(ORNL), Oak Ridge, TN (United States), 2017.

[11] S. Kihara, A. Ohtomo, I. Kajigaya, and F. Kishimoto, "Recent plant experience and research into fireside corrosion in Japan," *Materials and Corrosion*, vol. 39, no. 2, pp. 69–83, 1988.

[12] H. Naoi, H. Mimura, M. Ohgami, M. Sakakibara, S. Araki, Y. Sogoh, T. Ogawa, H. Sakurai, and T. Fujita, "Development of tubes and pipes for ultra-supercritical thermal power plant boilers," *Nippon Steel Technical Report*, pp. 22–22, 1993.

[13] M. P. Brady, Y. Yamamoto, G. Muralidharan, H. Rogers, and B. A. Pint, "Deployment of alumina forming austenitic (AFA) stainless steel," tech. rep., Oak Ridge National Laboratory (ORNL), 2013.

[14] A. S. Alomari, N. Kumar, and K. L. Murty, "Investigation on creep mechanisms of Alloy 709," in *ASME 2017 Nuclear Forum collocated with the ASME 2017 Power Conference Joint With ICOPE-17, the ASME 2017 11th International Conference on Energy Sustainability, and the ASME 2017 15th International Conference on Fuel Cell Science, Engineering and Technology*, pp. V009T02A003–V009T02A003, American Society of Mechanical Engineers, 2017.

[15] M. McMurtrey, L. Carroll, and J. Wright, "Microstructural effects on creep-fatigue life of Alloy 709," tech. rep., Idaho National Lab.(INL), Idaho Falls, United States, 2017.

[16] S. Upadhayay, "Tensile properties of advanced austenitic stainless steel, Alloy 709, using in-situ sem heating and loading," Master's thesis, North Carolina State University, 2017.

[17] M. P. Brady, Y. Yamamoto, M. L. Santella, P. J. Maziasz, B. A. Pint, C. Liu, Z. Lu, and H. Bei, "The development of alumina-forming austenitic stainless steels for high-temperature structural use," *The Journal of the Minerals*, vol. 60, no. 7, p. 12, 2008.

[18] K. Natesan, X. Zhang, T.-L. Sham, H. Wang, and H. Wang, "Report on the completion of the procurement of the first heat of Alloy 709," tech. rep., Argonne National Laboratory (ANL), 2017.

[19] E. Lara-Curzio, J. L. Moser, H. Wang, and C. S. Hawkins, "Shakedown tests for refurbished and upgraded frames and initiation of Alloy 709 creep rupture tests," tech. rep., Oak Ridge National Lab.(ORNL), Oak Ridge, TN (United States), 2017.

[20] M. Li, K. Natesan, and W.-Y. Chen, "FY 2017–thermal aging effects on advanced structural materials," tech. rep., Argonne National Lab.(ANL), Argonne, IL (United States), 2017.

[21] D. Smith, N. Lybeck, J. Wright, and R. Wright, "Thermophysical properties of Alloy 709," *Nuclear Engineering and Design*, vol. 322, pp. 331–335, 2017.

[22] S. Sham, "ARC materials development - accomplishments and plans." DOE-NE Materials Crosscut Coordination Meeting, 2013.

[23] B. Kim, L. Tan, C. Xu, Y. Yang, X. Zhang, and M. Li, "Microstructural evolution of NF709 (20Cr-25Ni-1.5 MoNbTiN) under neutron irradiation," *Journal of Nuclear Materials*, vol. 470, pp. 229–235, 2016.

[24] J. M. Howe, *Interfaces in materials: atomic structure, thermodynamics and kinetics of solid-vapor, solid-liquid and solid-solid interfaces*. Wiley-Interscience, 1997.

[25] W. Soffa, "Structures resulting from precipitation from solid solution," *ASM International*, vol. 9, pp. 646–650, 1985.

[26] C. T. Forwood and L. M. Clarebrough, *Electron microscopy of interfaces in metals and alloys*. CRC Press, 1991.

[27] M. Kronberg and u. F. Wilson, "Secondary recrystallization in copper," *Metals Transactions*, vol. 1, no. 8, pp. 501–514, 1949.

[28] D. Brandon, "The structure of high-angle grain boundaries," *Acta Metallurgica*, vol. 14, no. 11, pp. 1479–1484, 1966.

[29] Oxford Instruments Nanoanalysis, "Generating orientation maps to present EBSD data." Retrieved from https://www.azom.com/article.aspx?ArticleID =11775, 2015.

[30] L. Priester, *Grain boundaries: from theory to engineering*, vol. 172. Springer Science & Business Media, 2012.

[31] W. Shockley and W. Read, "Quantitative predictions from dislocation models of crystal grain boundaries," *Physical Review*, vol. 75, no. 4, p. 692, 1949.

[32] G. Hasson and C. Goux, "Interfacial energies of tilt boundaries in aluminium. Experimental and theoretical determination," *Scripta metallurgica*, vol. 5, no. 10, pp. 889–894, 1971.

[33] T. Sourmail, "Precipitation in creep resistant austenitic stainless steels," *Materials Science and Technology*, vol. 17, no. 1, pp. 1–14, 2001.

[34] Y. Zhou, Y. Liu, X. Zhou, C. Liu, J. Yu, Y. Huang, H. Li, and W. Li, "Precipitation and hot deformation behavior of austenitic heat-resistant steels: A review," *Journal of Materials Science & Technology*, vol. 33, no. 12, pp. 1448–1456, 2017.

[35] T. Sourmail and H. Bhadeshia, "Microstructural evolution in two variants of NF709 at 1023 and 1073 K," *Metallurgical and Materials Transactions A*, vol. 36, no. 1, pp. 23–34, 2005.

[36] R. Ecob, R. Lobb, and V. Kohler, "The formation of G-phase in 20/25 Nb stainless steel AGR fuel cladding alloy and its effect on creep properties," *Journal of materials science*, vol. 22, no. 8, pp. 2867–2880, 1987.

[37] R. Stickler and A. Vinckier, "Morphology of grain-boundary carbides and its influence on intergranular corrosion of 304 stainless steel," *Transactions of the American Society of Metals*, vol. 54, no. 362, p. 80, 1961.

[38] C. Tedmon, D. Vermilyea, and J. Rosolowski, "Intergranular corrosion of austenitic stainless steel," *Journal of the Electrochemical Society*, vol. 118, no. 2, pp. 192–202, 1971.

[39] P. Lin, K. Aust, G. Palumbo, and U. Erb, "Influence of grain boundary character distribution on sensitization and intergranular corrosion of Alloy 600," *Scripta Metallurgica et materialia*, vol. 33, no. 9, 1995.

[40] A. Joshi and D. F. Stein, "Chemistry of grain boundaries and its relation to intergranular corrosion of austenitic stainless steel," *Corrosion*, vol. 28, no. 9, pp. 321–330, 1972.

[41] M. H. Lewis and B. Hattersley, "Precipitation of $M_{23}C_6$ in austenitic steels," *Acta Metallurgica*, vol. 13, no. 11, pp. 1159–1168, 1965.

[42] K. Kaneko, T. Fukunaga, K. Yamada, N. Nakada, M. Kikuchi, Z. Saghi, J. S. Barnard, and P. A. Midgley, "Formation of $M_{23}C_6$-type precipitates and chromium-depleted zones in austenite stainless steel," *Scripta Materialia*, vol. 65, no. 6, pp. 509–512, 2011.

[43] Y. S. Lim, D. J. Kim, S. S. Hwang, H. P. Kim, and S. W. Kim, "$M_{23}C_6$ precipitation behavior and grain boundary serration in Ni-based Alloy 690," *Materials Characterization*, vol. 96, pp. 28–39, 2014.

[44] M. Gao and R. Wei, "Precipitation of intragranular $M_{23}C_6$ carbides in a nickel alloy: Morphology and crystallographic feature," *Scripta Metallurgica et Materialia*, vol. 30, no. 8, 1994.

[45] H. Liu, M. Gao, D. G. Harlow, and R. P. Wei, "Grain boundary character, and carbide size and spatial distribution in a ternary nickel alloy," *Scripta Metallurgica et Materialia*, vol. 32, no. 11, pp. 1807–1812, 1995.

[46] B. Sasmal, "Mechanism of the formation of lamellar $M_{23}C_6$ at and near twin boundaries in austenitic stainless steels," *Metallurgical and Materials Transactions A*, vol. 30, no. 11, pp. 2791–2801, 1999.

[47] J. Hu, B. Chen, D. J. Smith, P. E. Flewitt, and A. C. Cocks, "On the evaluation of the bauschinger effect in an austenitic stainless steel—the role of multi-scale residual stresses," *International Journal of Plasticity*, vol. 84, pp. 203–223, 2016.

[48] J. Don and S. Majumdar, "Creep cavitation and grain boundary structure in type 304 stainless steel," *Acta metallurgica*, vol. 34, no. 5, pp. 961–967, 1986.

[49] D. Dye, H. Stone, and R. Reed, "Intergranular and interphase microstresses," *Current opinion in solid state and materials Science*, vol. 5, no. 1, pp. 31–37, 2001.

[50] H. Möller, J. Barbers, and G. Martin, "Mitt. kaiser-wilhelm-inst. eisenforschg," *Düsseldorf*, vol. 21, p. 261, 1939.

[51] E. Kröner, "Berechnung der elastischen konstanten des vielkristalls aus den konstanten des einkristalls," *Zeitschrift für Physik*, vol. 151, no. 4, pp. 504–518, 1958.

[52] D. B. Williams and C. B. Carter, "Transmission electron microscope," in *Transmission electron microscopy*, Springer, 2009.

[53] B. D. Cullity and S. R. Stock, *Elements of X-ray Diffraction*. Pearson Education, 2014.

[54] G. Williamson and W. Hall, "X-ray line broadening from filed aluminium and wolfram," *Acta metallurgica*, vol. 1, no. 1, pp. 22–31, 1953.

[55] B. H. Toby and R. B. Von Dreele, "GSAS-II: the genesis of a modern open-source all purpose crystallography software package," *Journal of Applied Crystallography*, vol. 46, no. 2, pp. 544–549, 2013.

[56] E. Trillo and L. Murr, "A TEM investigation of $M_{23}C_6$ carbide precipitation behaviour on varying grain boundary misorientations in 304 stainless steels," *Journal of Materials Science*, vol. 33, no. 5, pp. 1263–1271, 1998.

[57] D. Powell, R. Pilkington, and D. Miller, "The precipitation characteristics of 20% Cr/25% Ni-Nb stabilised stainless steel," *Acta Metallurgica*, vol. 36, no. 3, pp. 713–724, 1988.

[58] A. Carter, T.Porter, K. Findley, and M. Kaufman, "Time temperature precipitation diagram and qualitative validation for Alloy 709," in *Transactions of the American Nuclear Society*, pp. 638–641, American Nuclear Society, 2017.

[59] J.-H. Shim, E. Kozeschnik, W.-S. Jung, S.-C. Lee, D.-I. Kim, J.-Y. Suh, Y.-S. Lee, and Y. W. Cho, "Numerical simulation of long-term precipitate evolution in austenitic heat-resistant steels," *Calphad*, vol. 34, no. 1, pp. 105–112, 2010.

[60] H. Yan, "Microstructure evolution in Alloy 709 at 550 and 650°C," Master's thesis, University of Illinois at Urbana-Champaign, 2018.

[61] M. Klinger and A. Jäger, "Crystallographic tool box (CrysTBox): automated tools for transmission electron microscopists and crystallographers," *Journal of applied crystallography*, vol. 48, no. 6, pp. 2012–2018, 2015.

[62] H. Jeong, S. Seo, H. Hong, and Y. Yoo, "Characterization of the parameters relating adjacent grains using transmission electron microscopy," *Journal of Applied Crystallography*, vol. 43, no. 6, pp. 1495–1501, 2010.

[63] S. Lartigue and L. Priester, "Stability of extrinsic grain boundary dislocations in relation with intergranular segregation and precipitation," *Acta Metallurgica*, vol. 31, no. 11, pp. 1809–1819, 1983.

[64] R. Jargelius-Pettersson, "Precipitation in a nitrogen-alloyed stainless steel at 850°C," *Scripta Metallurgica et Materialia*, vol. 28, no. 11, pp. 1399–1403, 1993.

[65] R. Hu, G. Bai, J. Li, J. Zhang, T. Zhang, and H. Fu, "Precipitation behavior of grain boundary $M_{23}C_6$ and its effect on tensile properties of Ni-Cr-W based superalloy," *Materials Science and Engineering: A*, vol. 548, pp. 83–88, 2012.

[66] A. Advani, R. Romero, L. Murr, D. Matlock, W. Fisher, P. Tarin, C. Cedillo, J. Maldonado, R. Miller, and E. Trillo, "Deformation effects on interfacial carbide precipitation and chromium-depletion in type 304 stainless steel," *Scripta Metallurgica et Materialia*, vol. 27, no. 12, pp. 1759–1764, 1992.

[67] H. Li, S. Xia, B. Zhou, W. Chen, and C. Hu, "The dependence of carbide morphology on grain boundary character in the highly twinned Alloy 690," *Journal of Nuclear Materials*, vol. 399, no. 1, pp. 108–113, 2010.

[68] Y. S. Lim, J. S. Kim, H. P. Kim, and H. D. Cho, "The effect of grain boundary misorientation on the intergranular $M_{23}C_6$ carbide precipitation in thermally treated Alloy 690," *Journal of Nuclear Materials*, vol. 335, no. 1, pp. 108–114, 2004.

[69] F. Wilson, "The morphology of grain-and twin-boundary carbides in austenitic steels," *The Journal of the Iron and Steel Institute*, vol. 209, pp. 126–130, 1971.

[70] B. Weiss and R. Stickler, "Phase instabilities during high temperature exposure of 316 austenitic stainless steel," *Metallurgical transactions*, vol. 3, no. 4, pp. 851–866, 1972.

[71] F. Beckitt and B. Clark, "The shape and mechanism of formation of $M_{23}C_6$ carbide in austenite," *Acta Metallurgica*, vol. 15, no. 1, pp. 113–129, 1967.

[72] L. Singhal and J. Martin, "The growth of $M_{23}C_6$ carbide on incoherent twin boundaries in austenite," *Acta Metallurgica*, vol. 15, no. 10, pp. 1603–1610, 1967.

[73] V. M. Riso, "Mechanical characterization of Alloy 709 stainless steel after high temperature aging for application in advanced reactor," Master's thesis, University of Illinois at Urbana-Champaign, 2018.

[74] E. Oliver, M. Daymond, and P. Withers, "Interphase and intergranular stress generation in carbon steels," *Acta Materialia*, vol. 52, no. 7, pp. 1937–1951, 2004.

[75] B. Clausen, T. Lorentzen, and T. Leffers, "Self-consistent modelling of the plastic deformation of fcc polycrystals and its implications for diffraction measurements of internal stresses," *Acta Materialia*, vol. 46, no. 9, pp. 3087–3098, 1998.

[76] B. Clausen, T. Lorentzen, M. A. Bourke, and M. R. Daymond, "Lattice strain evolution during uniaxial tensile loading of stainless steel," *Materials Science and Engineering: A*, vol. 259, no. 1, pp. 17–24, 1999.

[77] J. Pang, T. Holden, J. Wright, and T. Mason, "The generation of intergranular strains in 309H stainless steel under uniaxial loading," *Acta materialia*, vol. 48, no. 5, pp. 1131–1140, 2000.

[78] T. Holden, A. Clarke, and R. Holt, "Neutron diffraction measurements of intergranular strains in MONEL-400," *Metallurgical and Materials Transactions A*, vol. 28, no. 12, pp. 2565–2576, 1997.

[79] H. Sehitoglu, T. Foglesong, and H. Maier, "Precipitate effects on the mechanical behavior of aluminum copper alloys: Part I. Experiments," *Metallurgical and Materials Transactions A*, vol. 36, no. 3, pp. 749–761, 2005.

[80] H. Sehitoglu, T. Foglesong, and H. Maier, "Precipitate effects on the mechanical behavior of aluminum copper alloys: Part II. Modeling," *Metallurgical and materials Transactions A*, vol. 36, no. 13, pp. 763–770, 2005.